Discovery and characterization of a specific inhibitor of serine-threonine kinase cyclin dependent kinase-like 5 (CDKL5) demonstrates role in hippocampal CA1 physiology

Anna Castano*
Department of Pharmacology, University of Colorado School of Medicine, Aurora, CO
Anna.Castano@cuanschutz.edu

Margaux Silvestre*
Kinases and Brain Development Laboratory, The Francis Crick Institute, 1 Midland Road, London, NW1 1AT UK
Margaux.silvestre@crick.ac.uk

Carrow I. Wells
Structural Genomics Consortium, UNC Eshelman School of Pharmacy, University of North Carolina at Chapel Hill, Chapel Hill, North Carolina, 27599, United States of America
carrow.i.wells@gsk.com

Jennifer L. Sanderson
Department of Pharmacology, University of Colorado School of Medicine, Aurora, CO
JENNIFER.SANDERSON@CUANSCHUTZ.EDU

Carla A. Ferrer
Structural Genomics Consortium, UNC Eshelman School of Pharmacy, University of North Carolina at Chapel Hill, Chapel Hill, North Carolina, 27599, United States of America
Calafe2@hotmail.com

Han Wee Ong
Structural Genomics Consortium, UNC Eshelman School of Pharmacy, University of North Carolina at Chapel Hill, Chapel Hill, North Carolina, 27599, United States of America
onghw@live.unc.edu

Yi Liang
Structural Genomics Consortium, UNC Eshelman School of Pharmacy, University of North Carolina at Chapel Hill, Chapel Hill, North Carolina, 27599, United States of America
liang_yi@wuxiapptec.com

William Richardson
Centre for Medicines Discovery, Nuffield Department of Medicine, University of Oxford, Oxford, OX3 7FZ, United Kingdom
william.richardson95@outlook.com

Josie A. Silvaroli
Division of Pharmaceutics and Pharmacology, College of Pharmacy and Comprehensive Cancer Center, The Ohio State University, Columbus, Ohio, 43210, United States of America
silvaroli.1@osu.edu

Frances M. Bashore
Structural Genomics Consortium, UNC Eshelman School of Pharmacy, University of North Carolina at Chapel Hill, Chapel Hill, North Carolina, 27599, United States of America
Frances.Bashore@unc.edu

Jeffery L. Smith
Structural Genomics Consortium, UNC Eshelman School of Pharmacy, University of North Carolina at Chapel Hill, Chapel Hill, North Carolina, 27599, United States of America

jeffs@email.unc.edu

Isabelle M. Genereux
Structural Genomics Consortium, UNC Eshelman School of Pharmacy, University of North Carolina at Chapel Hill, Chapel Hill, North Carolina, 27599, United States of America
genereux@live.unc.edu

Kelvin Dempster
Kinases and Brain Development Laboratory, The Francis Crick Institute, 1 Midland Road, London, NW1 1AT UK
Kelvin.dempster@crick.ac.uk

David H. Drewry
Structural Genomics Consortium, UNC Eshelman School of Pharmacy, University of North Carolina at Chapel Hill, Chapel Hill, North Carolina, 27599, United States of America; UNC Lineberger Comprehensive Cancer Center, School of Medicine, University of North Carolina at Chapel Hill, Chapel Hill, North Carolina, 27599, United States of America
david.drewry@unc.edu

Navjot S. Pabla
Division of Pharmaceutics and Pharmacology, College of Pharmacy and Comprehensive Cancer Center, The Ohio State University, Columbus, Ohio, 43210, United States of America
pabla.2@osu.edu

Alex N. Bullock
Centre for Medicines Discovery, Nuffield Department of Medicine, University of Oxford, Oxford, OX3 7FZ, United Kingdom
alex.bullock@cmd.ox.ac.uk

Tim A. Benke#
Departments of Pediatrics, Pharmacology, Neurology and Otolaryngology, University of Colorado School of Medicine, Aurora, CO
Tim.Benke@cuanschutz.edu

Sila K. Ultanir#
Kinases and Brain Development Laboratory, The Francis Crick Institute, 1 Midland Road, London, NW1 1AT UK
Sila.ultanir@crick.ac.uk

Alison D. Axtman#
Structural Genomics Consortium, UNC Eshelman School of Pharmacy, University of North Carolina at Chapel Hill, Chapel Hill, North Carolina, 27599, United States of America;
orcid.org/0000-0003-4779-9932
Alison.Axtman@unc.edu

*Co-first authors, #Co-senior authors

Corresponding author: Tim A. Benke, University of Colorado Denver, School of Medicine, 12800 E 19th, MS8102, Denver, CO 80045, tim.benke@cuanschutz.edu

Number of words
Abstract: 210
Introduction: 811
Methods: 2976
Results: 2194
Discussion: 810
Number of Figures: 10
Number of Tables: 1
Number of References: 81
Supplementary information: 10 Figures, 2 schema, 2 tables, text

Funding: NIH-NINDS NS112770 (all), Ponzio Family Chair in Neurology Research (AC, TAB), The Structural Genomics Consortium (SGC) is a registered charity (number 1097737) that receives funds from Bayer AG, Boehringer Ingelheim, the Canada Foundation for Innovation, Eshelman Institute for Innovation, Genentech, Genome Canada through Ontario Genomics Institute [OGI-196], EU/EFPIA/OICR/McGill/KTH/Diamond, Innovative Medicines Initiative 2 Joint Undertaking [EUbOPEN grant 875510], Janssen, Merck KGaA (aka EMD in Canada and USA), Pfizer, the São Paulo Research Foundation-FAPESP, and Takeda (CIW, CAF, HWO, YL, FMB, JLS, IMG, DHD, ADA). Research reported in this publication was supported in part by the NC Biotechnology Center Institutional Support Grant 2018-IDG-1030 (DHD, ADA), NIH U24DK116204 (DHD, ADA), and NIH 1R44TR001916 (DHD, ADA). This work was supported by the Francis Crick Institute which receives its core funding from Cancer Research UK (CC2037), the UK Medical Research Council (CC2037), and the Wellcome Trust (CC2037); Loulou Foundation Project Grant (11015). Margaux Silvestre is a recipient of the Loulou foundation junior fellowship award (2021). For the purpose of Open Access, the author has applied a CC BY public copyright license to any Author Accepted Manuscript version arising from this submission.

Acknowledgments: NanoBRET constructs for CDKL5, GSK3α, and GSK3β were kindly provided to the SGC-UNC team by Promega. TREE*spot* kinase interaction mapping software (http://treespot.discoverx.com) was used to prepare the kinome trees in Figure 3. The authors thank the Diamond Light Source for beamtime (proposal mx28172) as well as the staff of beamline i04 for their guidance.

Disclosures:
Benke – Consultancy for AveXis, Ovid, GW Pharmaceuticals, International Rett Syndrome Foundation, Takeda, Taysha, CureGRIN, GRIN Therapeutics, Alcyone, Neurogene, and

Marinus; Clinical Trials with Acadia, Ovid, GW Pharmaceuticals, Marinus and RSRT; all remuneration has been made to his department

Axtman – Advisor for Proteic Bioscience Inc.

Abstract

Pathological loss-of-function mutations in cyclin-dependent kinase-like 5 (*CDKL5*) cause CDKL5 deficiency disorder (CDD), a rare and severe neurodevelopmental disorder associated with severe and medically refractory early-life epilepsy, motor, cognitive, visual and autonomic disturbances in the absence of any structural brain pathology. Analysis of genetic variants in CDD have indicated that CDKL5 kinase function is central to disease pathology. *CDKL5* encodes a serine-threonine kinase with significant homology to GSK3β, which has also been linked to synaptic function. Further, *Cdkl5* knock-out rodents have increased GSK3β activity and often increased long-term potentiation (LTP). Thus, development of a specific CDKL5 inhibitor must be careful to exclude cross-talk with GSK3β activity. We synthesized and characterized specific, high-affinity inhibitors of CDKL5 that do not have detectable activity for GSK3β. These compounds are very soluble in water but blood-brain barrier penetration is low. In rat hippocampal brain slices, acute inhibition of CDKL5 selectively reduces post-synaptic function of AMPA-type glutamate receptors in a dose-dependent manner. Acute inhibition of CDKL5 reduces hippocampal LTP. These studies provide new tools and insights into the role of CDKL5 as a newly appreciated, key kinase necessary for synaptic plasticity. Comparisons to rodent knock-out studies suggest that compensatory changes have limited the understanding of the roles of CDKL5 in synaptic physiology, plasticity and human neuropathology.

165 **Introduction**

166 Pathological loss-of-function mutations in cyclin-dependent kinase-like 5 (*CDKL5*)[1, 2]
167 cause CDKL5 deficiency disorder (CDD, OMIM 300203, 300672), a rare (incidence 1:40,000–
168 60,000[3-5]), severe neurodevelopmental disorder associated with severe early-life epilepsy,
169 motor, cognitive, visual and autonomic disturbances[2, 6-9, 10]. Epilepsy in CDD does not
170 respond to *any* antiseizure medications[11]; a newly approved therapy provides modest
171 improvements[12]. Hemizygous males and heterozygous females can be equally and severely
172 affected[13, 14]. These severe symptoms are in absence of any structural brain pathology[15].
173 CDKL5 is a key mediator of synaptic and network development and physiology. Recent analysis
174 of genetic variants in CDD have indicated that CDKL5 kinase function is central to disease
175 pathology[13, 16]. In other words, loss of kinase function seems functionally equivalent to loss
176 of the protein.

177 In rodent models, CDKL5 is expressed throughout the CNS primarily in neurons, increases
178 post-natally and is stabilized at peak levels in adults[17-19], indicating roles during development
179 and into adulthood. These features make it impossible to tease apart the precise role of altered
180 CDKL5 function in mediating these symptoms in CDD. It remains unclear whether symptomatic
181 abnormalities are due to chronic CDKL5 dysfunction, acute CDKL5 dysfunction during an earlier
182 critical developmental time point, worsened by epilepsy or any combination. Adult rodent
183 models of CDD are associated with abnormal behaviors, visual disturbances[20] and multiple
184 abnormal signaling cascades[21-25]. CDKL5 is localized to the dendritic spines of excitatory
185 synapses as well as the nucleus of neurons[17, 26, 27]. CDKL5 functions in the formation of
186 excitatory synapses with partners that include PSD-95[28], NGL-1[29], Shootin1[30], and
187 actin[17]. Previous work had suggested CDKL5 specific substrates including MeCP2, DNMT1,
188 AMPH1, NGL-1 and HDAC4 but reliable antibodies have not been available[20]. Recent work
189 has identified MAP1S and microtubule end binding protein 2 (EB2) as physiological CDKL5

190 substrates in brain [19]. A phosphospecific antibody for EB2-S222 has been used to report
191 CDKL5 activity in mouse models and human iPSCs [19, 31, 32]. CDKL5 is a binding partner of
192 both PSD-95 and gephyrin[33]; binding with PSD-95 is critical for spine development[21].
193 Studies have typically found that loss of CDKL5 leads to a global reduction in excitatory
194 synapse numbers[29, 34], reduced PSD-95[35, 36] and synapsin[35] with loss of AMPA-type
195 glutamate receptors (GluA2[37]) and increased NMDA-type glutamate receptors (GluN2B[38]).
196 Inhibitory synapses appear to be unaffected[29], although inhibitory synaptic currents are
197 affected in some CDKL5 mouse models[39]. Embryonic knock-out of *Cdkl5* rodents either
198 enhanced long-term potentiation (LTP) [38, 40] or did not affect LTP [37, 40] in an age
199 dependent fashion. Reports so far do not fully explain the presumed excitation/inhibition
200 imbalance in epilepsy. Further, immature CDKL5 deficient mice do not have seizures or
201 epilepsy[21, 41] and appear insensitive to pro-convulsants such as kainate [21]. This paradox
202 highlights a big gap in our understanding of CDKL5 function: early developmental onset of
203 medically resistant epilepsy in CDD contrasts with a complete lack in experimental models. The
204 reasons for this mismatch are unclear and include possible developmental or other rodent-
205 specific compensations, which typically involve transcriptional changes. Finally, the role of acute
206 CDKL5 kinase dysfunction at any developmental time point is unknown. To address this, we
207 sought to develop a sensitive and specific inhibitor of CDKL5.

208 *CDKL5* is an X-linked gene encoding a 115 kDa serine-threonine kinase and member of the
209 CMGC family that includes cyclin dependent kinases (CDK), MAP-kinases, glycogen synthase
210 kinases (GSK) and cyclin-dependent kinase-like (CDKL) [42]. It has limited structural homology
211 to CDKL1, 2, 3 and 4 (http://mbv.broadinstitute.org/) but significant homology to GSK3β[43].
212 *CDKL1-4* mRNA are expressed at much lower levels than *CDKL5* in mouse and human brain
213 (http://mouse.brain-map.org). Of these kinases, only GSK3β has been linked to brain synaptic
214 function[44].

215 CDKL5 appears to be linked to GSK3β function. *Cdkl5* knock-out mice have increased
216 GSK3β activity, as evidenced by *hypo*-phosphorylation of GSK3β at S-9 and decreased β-
217 catenin[22]. β-catenin, which is phosphorylated and destabilized by active GSK3β, is often used,
218 with S9-phospho-GSK3β, as a marker of GSK3β activity[45]. Inhibition of GSK3β in CDKL5
219 (young but not old) knock-out mice normalizes expression of β-catenin and S9-phospho-
220 GSK3β[22, 23]. While upstream signaling is also affected (mTOR and AKT)[21], it is completely
221 unclear how CDKL5 and GSK3β activities are linked in CDKL5 knock-out mice.
222 GSK3β mediates a yin-yang interaction of LTP and LTD. Activation of GSK3β is required for the
223 induction of GluN-LTD while inhibition occurs with the induction of LTP[44]. Thus, development
224 of a specific CDKL5 inhibitor must be careful to exclude crosstalk with GSK3β activity.

225 Here, we synthesized and characterized specific, high-affinity inhibitors of CDKL5 that do
226 not have detectable activity for GSK3β. These compounds are very soluble in water, but blood-
227 brain barrier penetration is low. When applied directly to rat hippocampal brain slices, acute
228 inhibition of CDKL5 selectively reduces post-synaptic function of AMPA-type glutamate
229 receptors in a dose-dependent manner and inhibits a key form of synaptic plasticity,
230 hippocampal LTP. These studies provide new insights into the role of CDKL5 in neuronal
231 function and pathology.

232

233 **Methods**

234 *Synthetic Schemes.* Compound **B1** was prepared as a TFA salt with >95% purity (by
235 HPLC) according to Scheme 1 (Supplementary Information) via a reductive coupling reaction in
236 the presence of sodium borohydride and ethanol followed by amide coupling and deprotection.
237 Compounds **B4** and **B12** were prepared as an HCl salt with >95% purity (by NMR) according to
238 Scheme 2 (Supplementary Information). An amide coupling reaction in the presence of

239 propylphosphonic anhydride (T3P) followed by nitro group reduction generated a common
240 intermediate. Subsequent amide coupling reaction followed by deprotection yielded **B4** and
241 **B12**. Full characterization of the intermediates and final products (Figure 2) are included as
242 Supplementary Information.

243 *NanoBRET Assays***.** Human embryonic kidney (HEK293) cells obtained from ATCC
244 (Manassas, VA, USA) were cultured in Dulbecco's Modified Eagle's medium (DMEM, Gibco)
245 supplemented with 10% (v/v) fetal bovine serum (FBS, Corning). These cells were incubated at
246 37°C in 5% CO_2 and passaged every 72 hours with trypsin (Gibco) so that they never reached
247 confluency. Promega (Madison, WI, USA) kindly provided constructs for NanoBRET
248 measurements of CDKL5 (NLuc-CDKL5), GSK3α (NLuc-GSK3α), and GSK3β (NLuc-GSK3β)
249 included in Table S1 as well as Figures 3, S4, and S5. N-terminal NLuc orientations were used
250 for all three kinases. NanoBRET assays were executed in dose–response (12-pt curves) format
251 in HEK293 cells as previously reported [46-48]. Assays were executed as recommended by
252 Promega, using 0.31 μM of tracer K11 for CDKL5, 0.13 μM of tracer K8 for GSK3α, and 0.063
253 μM of tracer K8 for GSK3β.

254 *Analysis of Kinome-Wide Selectivity***.** The broad selectivity of compounds **B1**, **B4**, and
255 **B12** at 1 μM was evaluated via the Eurofins DiscoverX Corporation (Fremont, CA, USA)
256 *scan*MAX assay platform. In total, 403 wild-type (WT) human kinases were included in these
257 analyses. Percent of control (PoC) values were generated, which allowed for the calculation of
258 selectivity scores (S_{10}(1 μM)) noted in Figure 3 [43]. WT human kinases in the *scan*MAX panel
259 with PoC ≤20 (and GSK3β) for **B1**, with PoC <10 for **B4**, and PoC <35 for **B12** are also included
260 in Figure 3. The kinome tree diagrams in Figure 3 were created based on WT kinases with PoC
261 <10 for each compound.

262 *Biochemical Assays***.** A homogenous competition binding assay for CDKL5 was
263 executed at Luceome Biotechnologies, LLC (Tuscon, AZ, USA) using their *KinaseSeeker*

264 technology [49]. Briefly, this is a luminescence-based assay that relies on displacement of an
265 active site dependent probe by an ATP-competitive test compound. Compounds **B1**, **B4**, and
266 **B12** were evaluated in dose–response (12-pt curve) format in duplicate. Curves are included in
267 Figure S4 and IC_{50} values generated are embedded in tables within Figure 3.

268 Radiometric enzymatic assays were executed at Eurofins at the K_m value for ATP to
269 generate dose–response (9-pt) curves for all kinases listed in Figure 3 (except for CDKL5). A
270 detailed protocol for these assays, which includes the protein constructs, substrate, and controls
271 employed, is part of the Eurofins website: https://www.eurofinsdiscoveryservices.com.

272 *Kinetic Solubility*. The kinetic solubility of compound **B1** was evaluated using an aliquot
273 of a 10 mM DMSO stock solution dissolved in phosphate buffered saline solution (PBS) at pH
274 7.4. This analysis was done by Analiza, Inc (Cleveland, OH, USA) as described previously [50].
275 The reported solubility values in Table 1 have been corrected for background nitrogen present
276 in DMSO and the media.

277 *Microsomal Stability*. Mouse liver microsomal stability of compound **B1** was evaluated by
278 Analiza, Inc (Cleveland, OH, USA) as described previously [48]. This data generated by Analiza
279 is included in Table 1.

280 *CDKL Family Thermal Shift Assays.* CDKL1, CDKL2, CDKL3, and CDKL5 proteins were
281 produced using the construct boundaries previously used to generate 4AGU, 4AAA, 3ZDU, and
282 4BGQ, respectively. 4 μM of the kinase domain of CDKL1, CDKL2, CDKL3, or CDLK5 in 10 mM
283 HEPES-NaOH pH 7.4 and 500 mM NaCl was incubated with **B1** (12.5, 25, or 50 μM) in the
284 presence of 5× SyPRO orange dye (Invitrogen). Next, fluorescence was evaluated using a
285 Real-Time PCR Mx3005p machine (Stratagene). A previously reported protocol was followed to
286 run the Tm shift assays and assess melting temperatures[56]. Data is included in Figure S6.

287 *CDKL5 Enzymatic Assays*. These assays were executed as previously described[57,
288 58]. Briefly, FLAG-tagged WT or kinase dead (KD, CDKL5 K42R) constructs of human CDKL5
289 were subcloned into a pT7CFE1-CHis plasmid (Thermo Fisher). A HeLa cell lysate-based Kit (1-
290 Step Human Coupled IVT Kit—DNA, 88881, Life Technologies) enabled *in vitro* translation of
291 these constructs. His Pur cobalt spin columns (Thermo Scientific) were used to purify the *in*
292 *vitro*-translated proteins. To execute the *in vitro* kinase assays, myelin basic protein (Active
293 Motif, 31314) was employed as a substrate for recombinant CDKL5. These two components
294 were incubated in kinase buffer (Cell Signaling, 9802) supplemented with or without ATP (50
295 μM) for 30 minutes at 30 °C, followed by kinase assays run using the ADP-Glo Kinase Assay kit
296 (Promega). After the termination of kinase assay, NuPAGE LDS Sample Buffer (4X) was added
297 to the reaction mixture and the samples were heated at 100°C for 10 minutes. The protein
298 samples were run on Invitrogen Bis-tris gradient midi-gels and transferred to PVDF membrane
299 for western blot analysis. Primary antibody used for western blot analysis was from Cell
300 Signaling: FLAG (#14793) and was used at 1:1,000 dilution. Anti-Rabbit HRP-conjugated
301 secondary antibody was from Jackson Immunoresearch (#111-035-144) and used at 1:5,000
302 dilution. Immunoblot signals were detected using SignalFire ECL Reagent (#6883) and X-ray
303 films (Bioland #A03-02). Canon LiDE400 scanner was used for scanning the films. Precision
304 Plus Protein Dual Color Standard prestained protein marker (Biorad) was used to estimate the
305 molecular weight of sample proteins.

306

307 *Snapshot PK Study*. The pharmacokinetics of compound **B1** was evaluated by
308 Pharmaron (San Diego, CA, USA) following a single intraperitoneal administration to CD1 mice
309 (two males). A dose of 2.29 mg/kg of the TFA salt of compound **B1** in NMP/Solutol/PEG-
310 400/normal saline (v/v/v/v, 10:5:30:55) was prepared just before use. This dose was calibrated
311 due to the compound being a salt form. Plasma was sampled 0.5-, 1-, 2-, and 4-hours post-

312 dose. Bioanalytical assays were run using Prominence HPLC and AB Sciex Triple Quan 5500
313 LC/MS/MS instruments, and a HALO column (90A, C18, 2.7 µm, 2.1x50 mm). Snapshot PK
314 results are included in Figure S10. PK parameters were estimated by non-compartmental model
315 using WinNonlin 8.3 (Certara, Princeton, NJ, USA). The lower limit of quantification for plasma
316 sampling was 1.53 ng/mL.

317 *Analysis of Brain/Plasma Concentration*. The brain/plasma concentration of compound
318 **B1** was evaluated by Pharmaron following a single intraperitoneal administration to CD1 mice
319 (three males per dose). Two doses (2.29 mg/kg and 7.63 mg/kg) of the TFA salt of compound
320 **B1** in NMP/Solutol/PEG-400/normal saline (v/v/v/v, 10:5:30:55) were prepared just before use.
321 These doses were calibrated due to the compound being a salt form. Plasma and brain samples
322 were collected 1-hour post-dose. Brain samples were homogenized at a ratio of 1:3 with PBS
323 (W/V, 1:3) and then final brain concentrations corrected. Bioanalytical assays were run using
324 Prominence HPLC and AB Sciex Triple Quan 5500 LC/MS/MS instruments, and a HALO
325 column (90A, C18, 2.7 µm, 2.1x50 mm). Brain/plasma concentration results are included in
326 Table S2. The lower limit of quantification for plasma sampling was 1.53 ng/mL and 0.763
327 ng/mL for brain.

328 *Animals-The Francis Crick Institute (TFCI).* Rat handling and housing was performed
329 according to the regulations of the Animal (Scientific Procedures) Act 1986. Animal studies were
330 approved by the Francis Crick Institute ethical committee and performed under U.K. Home
331 Office project license (PPL P5E6B5A4B).

332 *Rat Neuron Primary Culture-TFCI.* Primary cortical cultures were prepared from
333 embryonic day (E) E18.5 embryos of Long Evans rats as described [59]. Pregnant females were
334 culled using cervical dislocation, embryos were removed from the uterus and the brains were
335 taken out. Cortices were dissected out, pooled from multiple animals, and washed three times
336 with HBSS. An incubation with 0.25 % trypsin for 15 minutes at 37 °C was followed by four

337 times washing with HBSS. Cells were dissociated and then counted using a hemocytometer.
338 Neurons were plated on 12-well culture plates at a density of 300,000 cells per well. The wells
339 were coated with 0.1 M borate buffer containing 60 µg/mL poly-D-lysine and 2.5 µg/mL laminin
340 and placed in the incubator overnight. Neurons were plated with minimum essential medium
341 (MEM) containing 10% fetal bovine serum (FBS), 0.5% dextrose, 0.11 mg/mL sodium pyruvate,
342 2 mM glutamine and penicillin/streptomycin. After 4 hours, cultures were transferred to
343 neurobasal medium containing 1 mL of B27 (Gibco), 0.5 mM glutamax, 0.5 mM glutamine, 12.5
344 µM glutamate and penicillin/streptomycin. Primary neuronal cultures were kept at 37 °C and 5%
345 CO_2. Every 3-4 days, 20-30% of the maintenance media was refreshed. Between DIV14-16,
346 neurons were treated with 5 nM, 50 nM, 500 nM and 5 µM of the different compounds for 1
347 hour. The compounds were added directly to the media and the plates were place at 37 °C for
348 the time of the treatment. DMSO was added to the well for the control condition.

349 *Western Blotting-TFCI.* After treatment, neuronal cultures were lysed in 300 µL of 1X
350 sample buffer (Invitrogen) containing 0.1 M DTT. Lysates were sonicated briefly twice and
351 denatured at 70 °C for 10 minutes. The samples were centrifuged at 13,300 rpm for 10 minutes
352 and ran on NuPage 4-12% Bis-Tris polyacrylamide gels (Invitrogen). Proteins were transferred
353 onto a Immobilon PVDF membrane (Millipore), which was then blocked in 4% milk in tris-
354 buffered saline containing 0.1% Tween-20 (TBST) for 30 minutes. Primary antibodies were
355 incubated at 4 °C overnight, and HRP-conjugated secondary antibodies at RT for 2 hours. The
356 following primary antibodies were used: rabbit anti-CDKL5 (1:1,000; Atlas HPA002847), rabbit
357 anti-pS222 EB2 (1:2,000; Covalab, from [19]), rat anti-EB2 (1:2,000; Abcam ab45767), mouse
358 anti-tubulin (1:100,000; Sigma T9026), rabbit anti-β-catenin (1:1,000; Cell Signalling 9562) and
359 rabbit anti phospho-β-catenin (Ser33/37 Thr41) (1:250, Cell Signalling 9561).The following
360 secondary antibodies were used at a concentration of 1:10,000: HRP-conjugated anti-rabbit
361 (Jackson 711-035-152), HRP-conjugated anti-mouse (Jackson 715-035-151) and HRP-

362 conjugated anti-rat (Jackson 712-035-153). The membrane was developed using ECL reagent
363 (Cytiva) and was visualized with an Amersham Imager 600 (GE Healthcare). Quantification of
364 Western blots was manually performed using Image Studio Lite Software (version 5.2). EB2
365 phosphorylation was measured relative to total EB2 and catenin phosphorylation to total
366 catenin. The other proteins were normalized to tubulin, if not indicated otherwise.

367 *Animals-University of Colorado School of Medicine (UC-SOM).* All studies conformed to
368 the requirements of the National Institutes of Health *Guide for the Care and Use of Laboratory*
369 *Rats* and were approved by the Institutional Animal Care and Use subcommittee of the
370 University of Colorado Anschutz Medical Campus (protocol 00411). Timed-pregnant Sprague
371 Dawley rats (Charles Rivers Labs, Wilmington, MA, USA) gave birth in-house. All rodents were
372 housed in micro-isolator cages with water and chow available *ad libitum*.

373 *Hippocampal Slice Preparation and Electrophysiology-UC-SOM.* As done previously [60-
374 62], following rapid decapitation and removal of the rat brain at post-natal day (P) 20–30,
375 sagittal hippocampal slices (400 μm) were made using a vibratome (Leica VT 1200, Buffalo
376 Grove, IL) in ice-cold sucrose artificial cerebral spinal fluid (sACSF: 206 mM sucrose, 2.8 mM
377 KCl, 1 mM $CaCl_2$, 3 mM $MgSO_4$, 1.25 mM NaH_2PO_4, 26 mM $NaHCO_3$, 10 mM D-glucose and
378 bubbled with 95%/5% O_2/CO_2). Following removal of CA3, slices were recovered in a
379 submersion type chamber perfused with oxygenated artificial cerebral spinal fluid (ACSF: 124
380 mM NaCl, 3 mM KCl, 1 mM $MgSO_4$, 2 mM $CaCl_2$, 1.2 mM NaH_2PO_4, 26 mM NaHCO3, 10 mM
381 D-glucose and bubbled with 95%/5% O_2/CO_2) at 28°C for at least 90 min and then submerged
382 in a recording chamber perfused with recirculated ACSF. All electrophysiology was performed in
383 the CA1 region at 28°C. Drugs were added to ACSF. Two twisted-tungsten bipolar stimulating
384 electrodes were offset in the CA1 to stimulate one or two independent Schaffer collateral-
385 commissural pathways using a constant current source (WPI, Sarasota, FL) with a fixed
386 duration (20 μs), each at a rate of 0.033 Hz. Field excitatory post-synaptic potentials (fEPSPs)

387 were recorded from the stratum radiatum (or stratum pyramidale region where indicated) region
388 of CA1 using a borosilicate glass (WPI, Sarasota, Fl) microelectrode (pulled (Sutter, Novato,
389 CA) to 6 to 9 MΩ when filled with ACSF), amplified 1000x (WPI, Sarasota, Fl and Warner,
390 Hamden, CT), and digitized (National Instruments, Austin, Texas) at 20 kHz using winLTP-
391 version 2.4[63] to follow fEPSP slope (averaged over 4 EPSPs), measured using 20% to 80%
392 rise times, expressed as percent of baseline, during the course of an experiment. To be sure
393 only "healthy" slices were included in our studies, responses had to meet several criteria: fiber
394 volleys less than 1/3 of response amplitude and peak responses larger than 0.5 mV; responses
395 and fiber volley must be stable (<5% drift). Following baseline stabilization of fEPSP slope at
396 ~50% of maximal slope for at least 30 min, measurements of synaptic physiology were
397 performed. Stimulation was adjusted to make 4-6 measurements from ~10% to -90% maximal
398 slope to measure input-output (I/O) curves; recordings that deviated from linear slope were
399 rejected. Paired-pulse ratios of slopes and peaks were measured at ~50% of maximal slope.
400 For measurements of NMDA-receptor dependent population spikes [64], Mg2+ was omitted
401 from recording ACSF, the recording electrode was placed in stratum pyramidale, stimulation
402 was adjusted to evoke a first population spike > 2 mV, and stabilization of the 2nd NMDA-
403 receptor dependent population spike (measured from the coast-line of the fEPSP) for greater
404 than 30 minutes was allowed prior to measuring the effect of antagonists. Theta burst LTP was
405 induced at test strength of two trains, separated by 20 seconds, of 10 trains of 4 stimuli at
406 100Hz, separated by 200 msec. Potentiation was statistically compared over the last 5 minutes.

407 For whole-cell, voltage-clamp electrophysiological recordings of excitatory post-synaptic
408 currents (EPSCs), 350 µm horizontal hippocampal slices were prepared from rats at post-natal
409 day (P) 20-30 similar to previously[65, 66]. After 15 min recovery at 34°C, slices were
410 maintained at room temperature until recording in modified ACSF containing (in mM): 126 NaCl,
411 5 KCl, 2 $CaCl_2$, 1.25 NaH_2PO_4, 1 $MgSO_4$, 26 $NaHCO_3$, 10 glucose and 2 N-acetyl cysteine.

412 Slices were incubated in either CAF-382 (**B1**) (100 nM) or vehicle (water) in modified ACSF for
413 at least 1h prior to recording. Using infrared–differential interference contrast microscopy for
414 visualization, whole-cell recordings (Axopatch 200B amplifier and pClamp software (Molecular
415 Devices)) from CA1 pyramidal neurons (series resistance between 3 and 6 MΩ) were performed
416 at 29-30°C with an intracellular solution containing (in mM): 130 Cs gluconate, 1 CsCl, 1 $MgS0_4$,
417 10 HEPES, 1 EGTA, 4 MgATP, 0.4 MgGTP, spermine (0.01) and 2 QX-314, pH 7.3. AMPA-type
418 EPSCs, evoked using a bipolar tungsten-stimulating electrode as above, at a holding potential
419 of −65 mV were pharmacologically isolated using picrotoxin (50 μM; Tocris). EPSC peaks were
420 evoked every 20 seconds. After establishing whole-cell access, a 3 min baseline recording at
421 −65 mV was followed by LTP induction using a pairing protocol: cells were depolarized to 0 mV
422 for 90 sec and stimulated every 20 sec then followed by delivery of 1s x 100Hz high frequency
423 stimulation. Evoked EPSC amplitudes were subsequently monitored at -65 mV. Potentiation
424 was statistically compared over the last 5 minutes.

425 *Western Blotting-UC-SOM.* Hippocampal slices were prepared and recovered as for
426 electrophysiology with the addition of cuts to isolate CA1 from the remaining hippocampus; after
427 recovery, the slices from a given rat were incubated in inhibitor or vehicle (water) in ACSF for 2
428 hours. Following this, slices were suspended in STE buffer, sonicated, boiled for 5 minutes and
429 then frozen until further use. To minimize the effects of slice preparation[67] and to control for
430 slice quality, only slices that came from a preparation that met electrophysiological criteria were
431 used. All concentrations were quantified with BCA and then loaded in duplicate on 10%
432 polyacrylamide gel and a five-point dilution series of naive rat hippocampal homogenate was
433 included on each gel as a standard curve for quantification of immunoreactivity/ μg loaded
434 protein[68]. Following transfer to PolyScreen PVDF transfer membrane (Genie, Idea Scientific
435 Company, Minneapolis, MN, USA), blots were blocked in BSA or Carnation nonfat dry milk for 1
436 h and incubated either 1h at room temperature or overnight at 4°C with antibodies. The

437 following primary antibodies were used: sheep anti-CDKL5 (1:2,000; University of Dundee, Anti-
438 CDKL5(350-650)), rabbit anti-pS222 EB2 (1:1,000; Covalab, from [19]), rat anti-EB2 (1:1,000;
439 Abcam ab45767). Blots were then subjected to three 10-min washings in Tris-buffered saline
440 (140 mm NaCl, 20 mm Tris pH 7.6) plus 0.1% Tween 20 (TTBS), before being incubated with
441 anti-sheep, anti-rat or anti-rabbit secondary antibody (1:5000) in 1% BSA or milk for 1 h at room
442 temperature, followed by three additional 10-min washes preformed with TTBS.
443 Immunodetection was accomplished using a chemiluminescent substrate kit (SuperSignal West
444 Femto Maximum Sensitivity Substrate; Pierce) and the Alpha Innotech (Alpha Innotech, San
445 Leandro, CA, USA) imaging system. Quantification was performed using AlphaEase software
446 (Alpha Innotech, San Leandro, CA, USA) and Excel (Microsoft, Redmond, WA, USA).
447 Immunoreactivity was reported as the density of sample bands relative to the standard curve.
448 For phospho-proteins, ratios of immunoreactivity/μg to totals are reported without
449 standardization. Only values falling within the standard curve generated from the dilution series
450 included on each gel were incorporated into the final analysis. Some of the blots were then
451 stripped (Restore PLUS Western Blot Stripping Buffer; Thermo Scientific, Rockford, IL) and
452 reblotted if needed.

453 *Statistical Analysis-OSU.* Data were analyzed via GraphPad Prism 9. Each assay was
454 run in triplicate and mean values are graphed in Figure 4 with error bars showing standard
455 deviation (SD). In Figure 4, statistical analysis was done using one-way ANOVA with Dunnett's
456 multiple comparisons test. Thresholds for significance (p-values) were set at ***$p < 0.0001$ and
457 non-significant statistics were not included.

458 *Statistical Analysis-TFCI.* Data were analyzed using GraphPad Prism 9. Exact values of
459 n and statistical methods are mentioned in the figure legends. Each concentration was
460 compared to the control using a one-way ANOVA test. A p-value higher than 0.05 was not
461 considered as statistically significant. Thresholds for significance were placed at *$p \leq 0.05$, **$p \leq$

462 0.01, ***p ≤ 0.001 and ****p≤ 0.0001. All errors bars in the figures are standard deviation (SD)
463 where indicated. Non-significant statistics were not included.

464 *Statistical Analysis-UCSOM.* Data are expressed as mean ± SEM with n = number of
465 rats for a given treatment, unless otherwise stated. Data are plotted using Sigmaplot 12.5
466 (Systat, Chicago, IL, USA). Mann-Whitney Rank Sum, one-way, two-way and repeated
467 measures (RM) ANOVA (Holm-Sidak post-hoc testing) and Student's t-tests were used, where
468 indicated and appropriate, for statistical comparisons for electrophysiological and biochemical
469 using SigmaPlot 12.5 (Systat, Chicago, IL). Significance is reported at $p < 0.05$ unless otherwise
470 stated. All errors bars in the figures are standard error (SE) where indicated. Non-significant
471 statistics were not included.

472 *Data and materials availability.* Data has been uploaded to Dryad
473 (https://doi.org/10.5061/dryad.sn02v6x88). Newly synthesized compounds are available from
474 the senior authors (Alison.Axtman@unc.edu).

475

476 **Results**

477 *Identification of CDKL5 inhibitors that lack GSK3β activity.* SNS-032 and AT-7519 were
478 initially identified as potent CDK inhibitors [43, 69]. We profiled our extensive library of SNS-032
479 and AT-7519 analogs using the CDKL5 NanoBRET assay. In parallel, the CDKL5 actives (IC_{50}
480 <1 μM) were profiled using the GSK3β NanoBRET assay. Based on the data generated, a plate
481 of 25 compounds was assembled. Criteria for inclusion on this plate included an IC_{50} <400 nM in
482 the CDKL5 NanoBRET assay and >20-fold difference between the CDKL5 NanoBRET and the
483 GSK3β NanoBRET IC_{50} values (Table S1).

484 *A targeted screen of CDKL5 inhibitors in neurons.* A set of 20 CDKL5 inhibitors were
485 selected based on their selectivity properties for CDKL5 versus GSK3α/β for testing their

486 inhibition of CDKL5 in rat primary cortical neuron cultures. We tested if we could detect a dose-
487 dependent reduction of EB2 pSer222 following 1 hour incubation in culture media. We
488 normalized pS222 EB2 with total EB2 levels to assess a specific reduction in phosphorylation as
489 opposed to a loss of total protein levels. Almost all inhibitors showed a pSer222 EB2 reduction
490 at 500 nM; most inhibitors showed a reduction at 50 nM (Figure 1). Three inhibitors caused a
491 significant reduction in pSer222 EB2 at 5 nM without a change in total EB2 levels: CAF-382
492 (**B1**), HW2-013 (**B4**) and LY-213 (**B12**) (Figure 1). These represented different chemical parent
493 backbones, so we decided to study these inhibitors further.

494 *Potency and selectivity analyses of lead compounds.* As shown in Figure 2, **B1** is an
495 SNS-032 analog, while **B4** and **B12** are analogs of AT-7519. SNS-032 and AT-7519 are
496 published inhibitors of several members of the cyclin-dependent kinase (CDK) and cyclin-
497 dependent kinase-like (CDKL) families [43]. Before using these compounds as tools for
498 dissecting CDKL5 biology, we needed to first understand their kinome-wide selectivity. We
499 analyzed **B1**, **B4**, and **B12** at 1 μM using the Eurofins DiscoverX *scan*MAX panel, which
500 assesses binding to 403 wild-type (WT) human as well as several non-human and mutant
501 kinases. Percent of control (PoC) values are generated for each kinase contained within the
502 panel [43].

503 For **B1**, an analog of SNS-032, pan CDK inhibition was maintained (Figure 3A). All
504 kinases with PoC ≤20 in the DiscoverX *scan*MAX panel plus GSK3β were profiled using
505 orthogonal binding or enzymatic assays. While **B1** has a good selectivity score (S_{10}(1 μM) =
506 0.017), several CDKs (CDK9, PCTK1/CDK16, PCTK2/CDK17, PCTK3/CDK18) are potently
507 inhibited (IC_{50} ≤100 nM) (colored green in the nested table in Figure 3A). Weaker inhibition of
508 CDK7 as well as both GSK3α and GSK3β was noted. Curves corresponding to the affinity data
509 for CDKL5 and GSK3 are included in Figures S4 and S5A, respectively. As the binding pockets
510 share a high degree of similarly, the selectivity of **B1** within the CDKL family was further profiled

511 via thermal shift assays (Figure S6). The highest change in melting temperature (ΔTm, >5 ^{o}C)
512 was noted for CDKL5, while a modest ΔTm of 3–4 ^{o}C was observed for CDKL2. As a PoC value
513 of 48 for CDKL2 was observed when **B1** was screened at 1 μM in the DiscoverX *scan*MAX
514 panel, follow-up enzymatic studies were not executed for this kinase. We propose that only at
515 higher concentrations (>10 μM) would inhibition of this kinase become significant.

516 Compounds **B4** and **B12**, which are analogs of AT-7519, also demonstrated good
517 kinome-wide selectivity with S_{10}(1 μM) scores of 0.02 and 0.01, respectively (Figure 3).
518 Orthogonal profiling of **B4** confirmed high affinity binding to CDKL5, GSK3α, and GSK3β (green
519 in nested table in Figure 3B, curves in Figures S4 and S5B), with slightly weaker affinity for
520 GSK3α/β than CDKL5 evaluated via the respective cellular target engagement (NanoBRET)
521 assays (Figures 3, S4, and S5). Kinases with PoC ≤10 in the DiscoverX *scan*MAX panel were
522 profiled using orthogonal binding or enzymatic assays. An additional nine kinases demonstrated
523 PoC <35. Orthogonal profiling of **B12** confirmed high affinity binding to CDKL5, GSK3α, and
524 GSK3β (green in nested table in Figure 3C, curves in Figures S4 and S5C). This compound is a
525 more effective inhibitor of GSK3α when compared to GSK3β. As was the case for **B4**, **B12**
526 bound with greater affinity to CDKL5 than GSK3α/β in the respective NanoBRET assays
527 (Figures 3, S4, and S5C). Aside from GSK3α/β, a large (>100-fold) window exists between
528 CDKL5 and the next most potently inhibited kinase, DYRK2, when considering the enzymatic
529 and/or binding data.

530 Binding and orthogonal assay results in combination with Western blots confirmed that in
531 cells, **B1** is a CDKL5 and multi-CDK inhibitor with much weaker GSK3α/β affinity (>1.8 μM) and
532 inhibitory activity. Compounds **B4** and **B12** exhibited similar inhibition profiles and are potent
533 inhibitors of CDKL5, GSK3α, and GSK3β. Despite its potency, compound **B4** demonstrated
534 sub-optimal selectivity when compared with **B1** and **B12**. This was determined based on the

535 number of WT human kinases with PoC <35 in the DiscoverX *scan*MAX panel when profiled at
536 1 μM: **B1** = 12, **B4** = 17, **B12** = 9.

537 *In vitro kinase activity.* We employed *in vitro* kinase assays to evaluate the impact of **B1**
538 on CDKL5 activity (Figure 4). After preparing human WT and kinase dead (KD, CDKL5 K42R
539 [57, 58]) recombinant proteins, equal amounts were employed in CDKL5 activity assays (Figure
540 4B). We observed that, in the presence of ATP (50 μM, Figure 4A), WT CDKL5 but not KD
541 CDKL5 elicited kinase activity, as measured by turnover of ATP to ADP via a luminescent
542 reagent (ADP-Glo assay). Next, the activity of untreated WT CDKL5 was compared with WT
543 CDKL5 treated with vehicle (DMSO) or kinase inhibitors (10 or 100 nM). **B1**, AST-487, and
544 lapatinib were the inhibitors chosen. AST-487 is a confirmed, but less selective inhibitor of
545 CDKL5 (positive control) [51]. Lapatinib is a relatively selective kinase inhibitor that does not
546 inhibit CDKL5 (negative control). The difference between DMSO, lapatinib, and untreated
547 CDKL5 was not significant at 10 or 100 nM (Figure 4C, D). **B1** and AST-487, however, robustly
548 inhibited CDKL5 in a dose-dependent manner (Figure 4C, D). **B1** was confirmed to be a potent
549 inhibitor of CDKL5 kinase activity using this assay.

550 Kinase domains of GSK3β and CDKL5 have high similarity, to test the crosstalk of these
551 inhibitors with GSK3β, we measured phospho-β-catenin (Ser33/37/Thr41), which is directly
552 phosphorylated by GSK3β [19]. Phospho-β-catenin (Ser33/37/Thr41) is reduced upon exposure
553 to GSK3β inhibitor CHIR 99021 while EB2 pSer222, is not affected by GSK3β inhibition (Figure
554 S7). We measured pSer222 EB2 levels normalized to total EB2 at increasing concentrations of
555 inhibitors in primary neurons and compared this to phospho-β-catenin normalized to total
556 β–catenin (Figure 5). We found that CAF-382 (**B1**) showed a significant reduction in pSer222
557 EB2/total EB2 at 500 nM concentration (Figure 5A). There was a trend of pSer222 EB2/total
558 EB2 reduction from 5 nM, which was not significant (Figure 5A). Phospho-β-catenin/ total β-
559 catenin was not changed over the entire concentration range, indicating that CAF-382 (**B1)** does

560 not inhibit GSK3β (Figure 5A). HW2-013 (**B4)** was effective in reducing EB2 pSer222 at 500 nM
561 but also inhibited GSK3β significantly at 500 nM with a trend of inhibition from 5 nM, indicating
562 that this inhibitor affects GSK3β (Figure 5B). Finally, LY-213 (**B12**) reduced pSer222 EB2 at 500
563 nM but also seemed to decrease β-catenin phosphorylation at this concentration. LY-213 (**B12**)
564 showed comparable trends of inhibition for GSK3β and CDKL5 (Figure 5C). There were no
565 significant differences in total CDKL5, EB2 or β-catenin levels during these treatments (Figure
566 S8). We concluded that CAF-382 (**B1**) can inhibit CDKL5 activity without affecting GSK3 activity
567 in neurons.

568 *Acute CDKL5 inhibition by CAF-382 (**B1**) in rat hippocampal slices.* To determine if CAF-
569 382 (**B1**) could inhibit CDKL5 activity within intact brain tissue, we prepared acute hippocampal
570 slices from P20–30 rats and incubated them with CAF-382 (**B1**) for 2h as described. As for
571 primary cultures, CAF-382 (**B1**) reduced EB2 phosphorylation in a dose dependent fashion
572 (Figure 6). Similarly, SNS-032, the parent compound of CAF-382 (**B1**), also reduced EB2
573 phosphorylation in hippocampal slices (Figure S9).

574 Previous studies found that genetic knock-down of *Cdkl5* in primary rodent brain cultures
575 reduced glutamatergic excitatory synaptic transmission associated with loss of dendritic spines
576 [29]. In this approach, the time-course of loss of CDKL5 function is expected to occur over
577 several days. To clarify the more acute role of CDKL5 in regulating excitatory synaptic
578 transmission, we applied CAF-382 (**B1**) (10–100 nM) to hippocampal slices while measuring
579 fEPSPs in the CA1 hippocampus. While varying the stimulation strength applied to pre-synaptic
580 Schaffer-collateral pathway inputs, we were able to measure the input-output responsiveness
581 through measuring the input (fiber volley size) versus output (fEPSP slope). The slope of this
582 relationship was reduced in a dose-response relationship by CAF-382 (**B1**) within 30 minutes of
583 application (Figure 7A). In other words, for a similar input (fiber volley amplitude), the post-
584 synaptic responsiveness (fEPSP slope) was reduced (Figure 7B). This suggests that the effect

585 of acute CDKL5 inhibition by CAF-382 (**B1**) on glutamatergic synaptic transmission is primarily
586 post-synaptic. Determination that amphiphysin-1, a pre-synaptic protein, is phosphorylated by
587 CDKL5 [70] suggested a role of CDKL5 in presynaptic function. However, *Cdkl5* knock-out
588 studies showed that amphiphysin-1 was not phosphorylated by CDKL5 *in vivo*, suggesting an
589 alternative amphiphysin-1-independent mechanism is responsible for observed presynaptic
590 changes [Kontaxi et al Mike Cousin, biorxiv]. To investigate the presynaptic role of CDKL5
591 kinase function, the paired-pulse ratio across several paired-pulse intervals was measured
592 (Figure 8). CAF-382 (**B1**) (100 nM x 1 hour) had no effect on the paired-pulse ratio, confirming
593 the acute effects of CAF-382 (**B1**) are restricted to the post-synapse. fEPSP slopes are
594 mediated by AMPA-type glutamate receptors with NMDA-type glutamate receptors largely silent
595 under these conditions. In order to visualize the impact of CAF-382 (**B1**) on NMDA-type
596 glutamate receptor mediated responses, extracellular Mg^{2+} was removed from the recording
597 medium [64]. Under these conditions, a NMDA-receptor mediated field potential (population
598 spike 2) becomes apparent; this was not affected by CAF-382 (**B1**) (Figure 9) but was
599 completely blocked by the NMDA-type glutamate receptor antagonist D-APV (50 μM). This
600 result suggests that the acute effect of CAF-382 (**B1**) mediated CDKL5 inhibition is to selectively
601 reduce AMPA-type glutamate receptor-mediated responses post-synaptically.

602 A previous study found that germ-line knock-out of *Cdkl5* in the mouse enhanced long-
603 term potentiation (LTP) at 7–13 week old (wo) hippocampal Schaffer Collateral to CA1
604 synapses without alteration of the input-output relationship [38]. In another study, germ-line
605 knock-out of *Cdkl5* in a mouse at 4–5 wo did not affect stable LTP at this synapse [37]. In a rat
606 *Cdkl5* knock-out, LTP at this synapse was selectively increased at 3–4 wo but not at later ages
607 [40]. To clarify the more acute role of CDKL5 in regulating LTP at this synapse, we incubated 3–
608 4 wo hippocampal slices with CAF-382 (**B1)** (100 nM) for at least 30 minutes and, following
609 stable baseline measurements of fEPSP slope, induced LTP via theta burst to Schaffer

610 Collateral to CA1 synapses in the continuous presence of CAF-382 (**B1)**. Compared to
611 interleaved recordings from control slices, CAF-382 (**B1)** significantly reduced LTP at 60
612 minutes post theta-burst (Figure 10). To investigate this further, LTP at these synapses of
613 isolated AMPA-type glutamate receptors via a pairing protocol was measured using whole-cell
614 patch-clamp. In this case, hippocampal slices were incubated with CAF-382 (**B1)** (100 nM) for
615 only one hour prior to, but not during, recording. Compared to interleaved recordings from
616 control slices, CAF-382 (**B1)** significantly reduced LTP at 30 minutes post pairing (Figure 11).
617 The induction and expression of LTP includes the contributions of pre-synaptic and post-
618 synaptic mechanisms at both excitatory and inhibitory synapses[71, 72]. Since we do not see a
619 presynaptic effect of CAF-382 (**B1)** (Figure 8), and the approach (Fig. 11) removed the
620 contribution of inhibitory synapses, this supports the direct role of CDKL5 in the post-synaptic
621 mediation of LTP at this synapse at this age.

622 *Evaluation of suitability of CDKL5 lead for in vivo studies.* As our studies were all
623 executed *in vitro*, the suitability of **B1** for use *in vivo* was unknown. To gauge whether **B1** could
624 be dosed in animals using a water-based formulation, we first analyzed its aqueous kinetic
625 solubility (Table 1). **B1** demonstrated good solubility (196 μM), supporting that it readily
626 dissolves in aqueous buffer without observed precipitation. Mouse liver microsomal stability data
627 was also collected (Table 1). **B1** proved to be very tolerant to microsomal exposure and
628 demonstrated excellent stability (>85%) after 30 minutes. Since compound **B1** was found to
629 have the required aqueous solubility and mouse liver microsomal stability, it was submitted for
630 *in vivo* characterization. Pharmacokinetic analysis and brain exposure of mice following
631 intraperitoneal administration with **B1** were next examined. Plasma was sampled 0.5-, 1-, 2-,
632 and 4-hours post-dose with 2.29 mg/kg of a salt form of **B1** (Figure S10). No abnormal clinical
633 symptoms were observed in dosed animals. The half-life of **B1** was found to be <1h, with the
634 highest concentration of drug in the plasma found 0.5 h after dosing (Cmax = 508 ng/mL) and

635 total system exposure (AUCinf) of 646 h*ng/mL (Figure S10). The same dose (2.29 mg/kg) as
636 well as a 7.63 mg/kg dose were used to analyze the brain penetration of **B1** in mice 1h after
637 administration. As shown in Table S2, brain and plasma sampling indicated that brain
638 penetration of **B1** was generally low.

639

640 **Discussion**

641 CDD is a rare, devastating, genetically mediated neurological disorder with symptomatic
642 onset in very early infancy. Though there are newly approved therapies that provide some relief
643 for epilepsy [12], the additional features that are impactful to caregivers (Jeff Neul, personal
644 communication) of motor, cognitive, visual and autonomic disturbances [2, 6-9, 10] are not
645 currently addressed. CDKL5 protein [73] and *CDKL5* gene [74] replacement approaches are
646 advancing through pre-clinical studies to potential first-in-human trials
647 (https://www.ultragenyx.com/our-research/pipeline/ux055-for-cdd/). While CDKL5 is a key
648 mediator of synaptic and network development and physiology, the precise role of this kinase as
649 explored through genetic manipulations in rodent models remains unclear. This knowledge gap
650 prevents a full understanding of the role of CDKL5 across development and has implications for
651 determining and interpreting when protein and gene replacement strategies may be most
652 efficacious. As CDKL5 kinase function is central to disease pathology [13, 16], our development
653 of a specific CDKL5 kinase inhibitor aims to address this gap.

654 Following identification of existing inhibitors [69], detailed analysis of the activity of
655 analogs of these inhibitors in a range of assays identified three compounds with significant
656 selectivity over GSK3β, a key requirement due to structural homology [43] and linkage of
657 GSK3β to both synaptic physiology [44] and CDKL5-related signaling [22, 23]. The lead
658 compound, **CAF-382 (B1**), demonstrated potent activity in multiple assays, including target-
659 based *in vitro* biochemical assays and functional assays utilizing both rodent neuronal cultures

660 and brain slices. The results across all assays are consistent, and align with the hypothesis that
661 compound **B1** inhibits CDKL5 and blocks phosphorylation of a known CDKL5 substrate, EB2
662 [19, 31, 32]. Several cyclin dependent kinases (CDKs) that are potently (IC_{50} ≤100 nM) inhibited
663 (CDK9 [75], PCTK1/CDK16 [76], PCTK2/CDK17 [77], and PCTK3/CDK18 [78]) by **B1** are
664 expressed in the brain (http://mouse.brain-map.org). However, none of these have been
665 demonstrated to have synaptic activity or localization; each are largely involved in replication
666 and nuclear functions. At issue, is whether observations of CDKL5 activity, either through
667 genetic manipulations or interference with the kinase, are specific and not potentially subsumed
668 by the activity of other kinases. Given the reduction of phosphorylation of the specific substrate,
669 EB2, this is less likely here.

670 The biochemical activity of **CAF-382** (**B1**) against CDKL5 is <5 nM, based on *in vitro*
671 activity studies (Figure 4), and for studies investigating cellular target engagement as well as
672 activity in neuronal cultures and brain slices at the specific substrate, EB2, and synaptic
673 physiology we observe a 10-fold shift in potency (~50 nM). A loss in potency, albeit modest,
674 when moving from a biochemical to cell-based assay is commonly observed, mostly due to
675 suboptimal cell penetrance of the small molecule, and has been observed for several orthogonal
676 chemical series of kinase inhibitors[47, 48, 50]. As the *in vitro* assay eliminates the contribution
677 of phosphatases (and the phosphatases specific for EB2 are currently unknown), the apparent
678 mismatch could also be due to residual presence of phosphatase-dependent and previously
679 phosphorylated EB2 balanced with active phosphorylation by CDKL5. Nevertheless, CDKL5
680 kinase function is clearly necessary for the induction and/or expression long-term potentiation,
681 adding to the very short list of kinases required for this essential process linked to learning and
682 memory[71, 72, 79] and finally clarifying previous genetic studies. The increased LTP seen in
683 genetic studies suggests that observations of increased LTP in these models is compensatory
684 and not directly due to loss of CDKL5. One interpretation of those prior studies is that CDKL5

provided a limiting “brake” on LTP, with genetic loss resulting in more LTP which is in contradistinction to our findings. The role of CDKL5 at inhibitory synapses was not specifically examined. Nevertheless, synaptic function at the developmental age studied (P20–30) requires CDKL5 activity for synaptic plasticity, suggesting that strategies that boost function at this age-equivalent in humans may be clinically important. Selective stability and plasticity dependent insertion of AMPA-type glutamate receptors at CA1 hippocampal synapses likely require a balance between active CDKL5 kinase and phosphatases. Further studies are needed to determine this balance more specifically and continue to clarify CDKL5 function at pre-synapses[80].

While no clinical abnormalities were observed with *in vivo* administration of CAF-382 (**B1**), this is likely due to low brain penetration. Due to low brain penetration of CAF-382 (**B1**), strategies that optimize brain penetration or different administration routes could be considered in future studies investigating the role of CDKL5 *in vivo*. These studies, behavioral and perhaps with electrical assessments of seizure activity, may clarify the apparent mismatch of rodent knock-out with clinical observations. Using CDKL5 inhibitors *in vivo* across developmental stages can help ascertain possible therapeutic windows for CDD. More broadly, CDKL5 inhibition is beneficial for cell survival upon ischemia or nephrotoxin induced kidney injury[58, 81], suggesting that the inhibitors we characterized here may prove useful to evaluate the promise of CDKL5 inhibition in other disease models.

Contributions: TAB, SKU and ADA conceived the project. CAF, HWO, YL, FMB, IMG, and DHD designed and synthesized compounds. WR and ANB executed CDKL family thermal shift assays. AC, MS, CIW, JAS, JLS, KD, DHD, NSP, ANB, TAB, SKU, and ADA conducted experiments and analyses. TAB, SKU and ADA drafted the paper, and all contributed to revisions.

References

1. Weaving, L.S., et al., *Mutations of CDKL5 cause a severe neurodevelopmental disorder with infantile spasms and mental retardation.* Am.J Hum.Genet., 2004. **75**(6): p. 1079-1093.
2. Bahi-Buisson, N., et al., *Recurrent mutations in the CDKL5 gene: genotype-phenotype relationships.* Am.J Med.Genet.A, 2012. **158A**(7): p. 1612-1619.
3. Lindy, A.S., et al., *Diagnostic outcomes for genetic testing of 70 genes in 8565 patients with epilepsy and neurodevelopmental disorders.* Epilepsia, 2018. **59**(5): p. 1062-1071.
4. Kothur, K., et al., *Diagnostic yield of targeted massively parallel sequencing in children with epileptic encephalopathy.* Seizure, 2018. **59**: p. 132-140.
5. Symonds, J.D., et al., *The Genetic and Autoimmune Childhood Epilepsy (GACE) Study*, in *American Epilpesy Society*. 2017: Washington, D.C.
6. Bahi-Buisson, N., et al., *Key clinical features to identify girls with CDKL5 mutations.* Brain, 2008. **131**(Pt 10): p. 2647-2661.
7. Nemos, C., et al., *Mutational spectrum of CDKL5 in early-onset encephalopathies: a study of a large collection of French patients and review of the literature.* Clin.Genet., 2009. **76**(4): p. 357-371.
8. Castren, M., et al., *Epilepsy caused by CDKL5 mutations.* Eur J Paediatr Neurol, 2011. **15**(1): p. 65-9.
9. Melani, F., et al., *CDKL5 gene-related epileptic encephalopathy: electroclinical findings in the first year of life.* Developmental Medicine and Child Neurology, 2011. **53**(4): p. 354-360.
10. Fehr, S., et al., *There is variability in the attainment of developmental milestones in the CDKL5 disorder.* J Neurodev Disord, 2015. **7**(1): p. 2.
11. Muller, A., et al., *Retrospective evaluation of low long-term efficacy of antiepileptic drugs and ketogenic diet in 39 patients with CDKL5-related epilepsy.* Eur J Paediatr Neurol, 2016. **20**(1): p. 147-51.
12. Knight, E.M.P., et al., *Safety and efficacy of ganaxolone in patients with CDKL5 deficiency disorder: results from the double-blind phase of a randomised, placebo-controlled, phase 3 trial.* Lancet Neurol, 2022. **21**(5): p. 417-427.
13. Demarest, S.T., et al., *CDKL5 deficiency disorder: Relationship between genotype, epilepsy, cortical visual impairment, and development.* Epilepsia, 2019.
14. Wong, K., et al., *Factors influencing the attainment of major motor milestones in CDKL5 deficiency disorder.* Eur J Hum Genet, 2022.
15. Pini, G., et al., *Variant of Rett syndrome and CDKL5 gene: clinical and autonomic description of 10 cases.* Neuropediatrics, 2012. **43**(1): p. 37-43.
16. Hector, R.D., et al., *CDKL5 variants: Improving our understanding of a rare neurologic disorder.* Neurol Genet, 2017. **3**(6): p. e200.
17. Chen, Q., et al., *CDKL5, a protein associated with rett syndrome, regulates neuronal morphogenesis via Rac1 signaling.* J Neurosci, 2010. **30**(38): p. 12777-86.
18. Hector, R.D., et al., *Characterisation of CDKL5 Transcript Isoforms in Human and Mouse.* PLoS One, 2016. **11**(6): p. e0157758.
19. Baltussen, L.L., et al., *Chemical genetic identification of CDKL5 substrates reveals its role in neuronal microtubule dynamics.* EMBO J, 2018.
20. Zhu, Y.C. and Z.Q. Xiong, *Molecular and Synaptic Bases of CDKL5 Disorder.* Dev Neurobiol, 2018.
21. Wang, I.T., et al., *Loss of CDKL5 disrupts kinome profile and event-related potentials leading to autistic-like phenotypes in mice.* Proc.Natl.Acad.Sci.U.S.A, 2012. **109**(52): p. 21516-21521.

22. Fuchs, C., et al., *Inhibition of GSK3beta rescues hippocampal development and learning in a mouse model of CDKL5 disorder.* Neurobiol Dis, 2015. **82**: p. 298-310.
23. Fuchs, C., et al., *Loss of CDKL5 impairs survival and dendritic growth of newborn neurons by altering AKT/GSK-3beta signaling.* Neurobiol Dis, 2014. **70**: p. 53-68.
24. Schroeder, E., et al., *Neuron-Type Specific Loss of CDKL5 Leads to Alterations in mTOR Signaling and Synaptic Markers.* Mol Neurobiol, 2019. **56**(6): p. 4151-4162.
25. Ren, E., et al., *Functional and Structural Impairments in the Perirhinal Cortex of a Mouse Model of CDKL5 Deficiency Disorder Are Rescued by a TrkB Agonist.* Front Cell Neurosci, 2019. **13**: p. 169.
26. Rusconi, L., et al., *CDKL5 expression is modulated during neuronal development and its subcellular distribution is tightly regulated by the C-terminal tail.* J Biol Chem, 2008. **283**(44): p. 30101-11.
27. Oi, A., et al., *Subcellular distribution of cyclin-dependent kinase-like 5 (CDKL5) is regulated through phosphorylation by dual specificity tyrosine-phosphorylation-regulated kinase 1A (DYRK1A).* Biochem Biophys Res Commun, 2017. **482**(2): p. 239-245.
28. Zhu, Y.C., et al., *Palmitoylation-dependent CDKL5-PSD-95 interaction regulates synaptic targeting of CDKL5 and dendritic spine development.* Proc Natl Acad Sci U S A, 2013. **110**(22): p. 9118-23.
29. Ricciardi, S., et al., *CDKL5 ensures excitatory synapse stability by reinforcing NGL-1-PSD95 interaction in the postsynaptic compartment and is impaired in patient iPSC-derived neurons.* Nat.Cell Biol., 2012. **14**(9): p. 911-923.
30. Nawaz, M.S., et al., *CDKL5 and Shootin1 Interact and Concur in Regulating Neuronal Polarization.* PLoS One, 2016. **11**(2): p. e0148634.
31. Terzic, B., et al., *Temporal manipulation of Cdkl5 reveals essential postdevelopmental functions and reversible CDKL5 deficiency disorder-related deficits.* J Clin Invest, 2021. **131**(20).
32. Di Nardo, A., et al., *Phenotypic characterization of Cdkl5-knockdown neurons establishes elongated cilia as a functional assay for CDKL5 Deficiency Disorder.* Neurosci Res, 2022. **176**: p. 73-78.
33. Uezu, A., et al., *Identification of an elaborate complex mediating postsynaptic inhibition.* Science, 2016. **353**(6304): p. 1123-9.
34. Della Sala, G., et al., *Dendritic Spine Instability in a Mouse Model of CDKL5 Disorder Is Rescued by Insulin-like Growth Factor 1.* Biol Psychiatry, 2016. **80**(4): p. 302-11.
35. Negraes, P.D., et al., *Altered network and rescue of human neurons derived from individuals with early-onset genetic epilepsy.* Mol Psychiatry, 2021. **26**(11): p. 7047-7068.
36. Lupori, L., et al., *Site-specific abnormalities in the visual system of a mouse model of CDKL5 deficiency disorder.* Hum Mol Genet, 2019. **28**(17): p. 2851-2861.
37. Yennawar, M., R.S. White, and F.E. Jensen, *AMPA Receptor Dysregulation and Therapeutic Interventions in a Mouse Model of CDKL5 Deficiency Disorder.* J Neurosci, 2019. **39**(24): p. 4814-4828.
38. Okuda, K., et al., *CDKL5 controls postsynaptic localization of GluN2B-containing NMDA receptors in the hippocampus and regulates seizure susceptibility.* Neurobiol Dis, 2017. **106**: p. 158-170.
39. Tang, S., et al., *Loss of CDKL5 in Glutamatergic Neurons Disrupts Hippocampal Microcircuitry and Leads to Memory Impairment in Mice.* J Neurosci, 2017. **37**(31): p. 7420-7437.
40. de Oliveira, L.S., et al., *Enhanced hippocampal LTP but typical NMDA receptor and AMPA receptor function in a novel rat model of CDKL5 deficiency disorder.* bioRxiv, 2022: p. 2022.06.29.497927.

41. Amendola, E., et al., *Mapping pathological phenotypes in a mouse model of CDKL5 disorder.* PLoS One, 2014. **9**(5): p. e91613.
42. Manning, G., et al., *The protein kinase complement of the human genome.* Science, 2002. **298**(5600): p. 1912-34.
43. Davis, M.I., et al., *Comprehensive analysis of kinase inhibitor selectivity.* Nat Biotechnol, 2011. **29**(11): p. 1046-51.
44. Peineau, S., et al., *The role of GSK-3 in synaptic plasticity.* Br.J Pharmacol, 2008. **153 Suppl 1**: p. S428-S437.
45. Wada, A., *Lithium and neuropsychiatric therapeutics: neuroplasticity via glycogen synthase kinase-3beta, beta-catenin, and neurotrophin cascades.* J Pharmacol Sci, 2009. **110**(1): p. 14-28.
46. Wells, C., et al., *SGC-AAK1-1: A Chemical Probe Targeting AAK1 and BMP2K.* ACS Med Chem Lett, 2020. **11**(3): p. 340-345.
47. Wells, C.I., et al., *Development of a potent and selective chemical probe for the pleiotropic kinase CK2.* Cell Chem Biol, 2021. **28**(4): p. 546-558 e10.
48. Drewry, D.H., et al., *Identification and Utilization of a Chemical Probe to Interrogate the Roles of PIKfyve in the Lifecycle of beta-Coronaviruses.* J Med Chem, 2022. **65**(19): p. 12860-12882.
49. Jester, B.W., et al., *A coiled-coil enabled split-luciferase three-hybrid system: applied toward profiling inhibitors of protein kinases.* J Am Chem Soc, 2010. **132**(33): p. 11727-35.
50. Drewry, D.H., et al., *Identification of Pyrimidine-Based Lead Compounds for Understudied Kinases Implicated in Driving Neurodegeneration.* J Med Chem, 2022. **65**(2): p. 1313-1328.
51. Canning, P., et al., *CDKL Family Kinases Have Evolved Distinct Structural Features and Ciliary Function.* Cell Rep, 2018. **22**(4): p. 885-894.
52. Winter, G., C.M. Lobley, and S.M. Prince, *Decision making in xia2.* Acta Crystallogr D Biol Crystallogr, 2013. **69**(Pt 7): p. 1260-73.
53. Winter, G., et al., *DIALS: implementation and evaluation of a new integration package.* Acta Crystallogr D Struct Biol, 2018. **74**(Pt 2): p. 85-97.
54. Liebschner, D., et al., *Macromolecular structure determination using X-rays, neutrons and electrons: recent developments in Phenix.* Acta Crystallogr D Struct Biol, 2019. **75**(Pt 10): p. 861-877.
55. Emsley, P. and K. Cowtan, *Coot: model-building tools for molecular graphics.* Acta Crystallogr D Biol Crystallogr, 2004. **60**(Pt 12 Pt 1): p. 2126-32.
56. Fedorov, O., et al., *A systematic interaction map of validated kinase inhibitors with Ser/Thr kinases.* Proc Natl Acad Sci U S A, 2007. **104**(51): p. 20523-8.
57. Lin, C., B. Franco, and M.R. Rosner, *CDKL5/Stk9 kinase inactivation is associated with neuronal developmental disorders.* Hum Mol Genet, 2005. **14**(24): p. 3775-86.
58. Kim, J.Y., et al., *A kinome-wide screen identifies a CDKL5-SOX9 regulatory axis in epithelial cell death and kidney injury.* Nat Commun, 2020. **11**(1): p. 1924.
59. Rosianu, F., et al., *Loss of NDR1/2 kinases impairs endomembrane trafficking and autophagy leading to neurodegeneration.* Life Sci Alliance, 2023. **6**(2).
60. Cornejo, B.J., et al., *A single episode of neonatal seizures permanently alters glutamatergic synapses.* Ann Neurol, 2007. **61**(5): p. 411-426.
61. Bernard, P.B., et al., *Necessary, but not sufficient: Insights into the mechanisms of mGluR mediated long-term depression from a rat model of early life seizures.* Neuropharmacology, 2014. **84**: p. 1-12.
62. Bernard, P.B., et al., *Phosphorylation of FMRP and alterations of FMRP complex underlie enhanced mLTD in adult rats triggered by early life seizures.* Neurobiol.Dis., 2013. **59**: p. 1-17.

63. Anderson, W.W. and G.L. Collingridge, *The LTP program: a data acquistion program for on-line analysis of long-term potentiation and other synaptic events.* J Neurosci Methods, 2001. **108**: p. 71-83.
64. Coan, E.J. and G.L. Collingridge, *Magnesium ions block an N-methyl-D-aspartate receptor-mediated component of synaptic transmission in rat hippocampus.* Neuroscience Letters, 1985. **53**: p. 21-26.
65. Sanderson, J.L., et al., *beta-Amyloid disruption of LTP/LTD balance is mediated by AKAP150-anchored PKA and Calcineurin regulation of Ca(2+)-permeable AMPA receptors.* Cell Rep, 2021. **37**(1): p. 109786.
66. Sanderson, J.L., J.A. Gorski, and M.L. Dell'Acqua, *NMDA Receptor-Dependent LTD Requires Transient Synaptic Incorporation of Ca(2)(+)-Permeable AMPARs Mediated by AKAP150-Anchored PKA and Calcineurin.* Neuron, 2016. **89**(5): p. 1000-15.
67. Osterweil, E.K., et al., *Hypersensitivity to mGluR5 and ERK1/2 leads to excessive protein synthesis in the hippocampus of a mouse model of fragile X syndrome.* J Neurosci, 2010. **30**(46): p. 15616-15627.
68. Grosshans, D.R. and M.D. Browning, *Protein kinase C activatio induces tyrosine phosphorylation of the NR2A and NR2B subunits of the NMDA receptor.* J Neurochem, 2001. **76**: p. 737-744.
69. Vasta, J.D., et al., *Quantitative, Wide-Spectrum Kinase Profiling in Live Cells for Assessing the Effect of Cellular ATP on Target Engagement.* Cell Chem Biol, 2018. **25**(2): p. 206-214 e11.
70. Sekiguchi, M., et al., *Identification of amphiphysin 1 as an endogenous substrate for CDKL5, a protein kinase associated with X-linked neurodevelopmental disorder.* Arch Biochem Biophys, 2013. **535**(2): p. 257-67.
71. Collingridge, G.L. and W.C. Abraham, *Glutamate receptors and synaptic plasticity: The impact of Evans and Watkins.* Neuropharmacology, 2022. **206**: p. 108922.
72. Nicoll, R.A., *A Brief History of Long-Term Potentiation.* Neuron, 2017. **93**(2): p. 281-290.
73. Trazzi, S., et al., *CDKL5 protein substitution therapy rescues neurological phenotypes of a mouse model of CDKL5 disorder.* Hum Mol Genet, 2018. **27**(9): p. 1572-1592.
74. Gao, Y., et al., *Gene replacement ameliorates deficits in mouse and human models of cyclin-dependent kinase-like 5 disorder.* Brain, 2020. **(in press)**.
75. Yu, D.S. and D. Cortez, *A role for CDK9-cyclin K in maintaining genome integrity.* Cell Cycle, 2011. **10**(1): p. 28-32.
76. Mikolcevic, P., J. Rainer, and S. Geley, *Orphan kinases turn eccentric: a new class of cyclin Y-activated, membrane-targeted CDKs.* Cell Cycle, 2012. **11**(20): p. 3758-68.
77. Liu, M., et al., *The Identification of Key Genes and Pathways in Glioma by Bioinformatics Analysis.* J Immunol Res, 2017. **2017**: p. 1278081.
78. de Oliveira Pepino, R., et al., *Overview of PCTK3/CDK18: A Cyclin-Dependent Kinase Involved in Specific Functions in Post-Mitotic Cells.* Curr Med Chem, 2021. **28**(33): p. 6846-6865.
79. Giese, K.P. and K. Mizuno, *The roles of protein kinases in learning and memory.* Learn Mem, 2013. **20**(10): p. 540-52.
80. Kontaxi, C., et al., *Epilepsy-related CDKL5 deficiency slows synaptic vesicle endocytosis in central nerve terminals.* J Neurosci, 2023.
81. Kim, J.Y., et al., *Involvement of the CDKL5-SOX9 signaling axis in rhabdomyolysis-associated acute kidney injury.* Am J Physiol Renal Physiol, 2020. **319**(5): p. F920-F929.

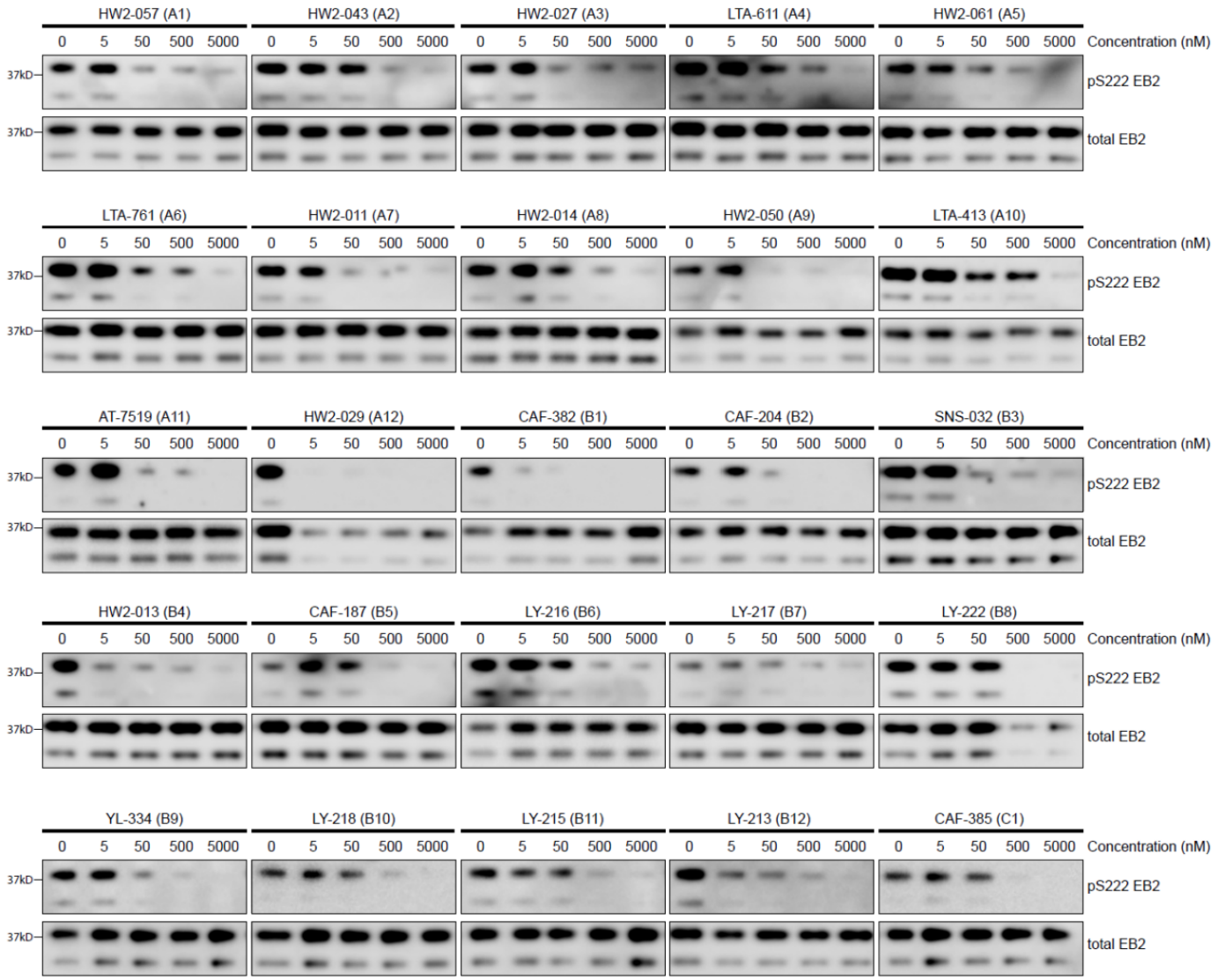

Figure 1. Screening of CDKL5 inhibitors in rat primary neurons using Western blotting. Western blots showing expression of total EB2 and levels of Ser222 EB2 phosphorylation in DIV14-16 rat primary neurons upon treatment of 1 hour with 5 nM, 50 nM, 500 nM and 5000 nM of selected CDKL5 inhibitors.

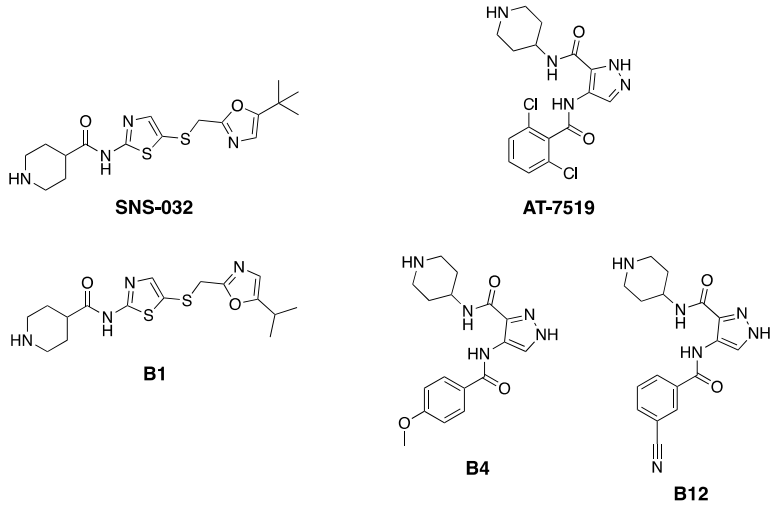

Figure 2. Structures of CDKL5 inhibitor leads and corresponding parent compounds.

A

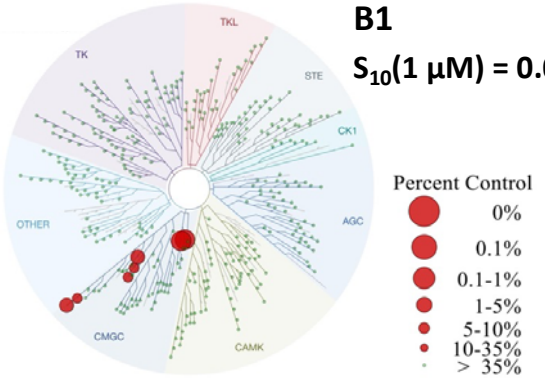

B1

S_{10}(1 μM) = 0.017

Kinase	DiscoverX PoC value	Assay format	IC_{50} value (nM)
GSK3A	0.7	Enzymatic and NB	470 and 1900
CDKL5	0.7	Binding and NB	6.7 and 11
PCTK2	1.3	Enzymatic	89
CDK7	1.9	Enzymatic	300
PCTK1	5.5	Enzymatic	62
CDC2L5	5.9	Enzymatic	>10000
CDK9	8.3	Enzymatic	20
YSK4	14	Enzymatic	>10000
PCTK3	17	Enzymatic	100
CDK4	20	Enzymatic	1900
GSK3B	51	Enzymatic and NB	2200 and 4500

B

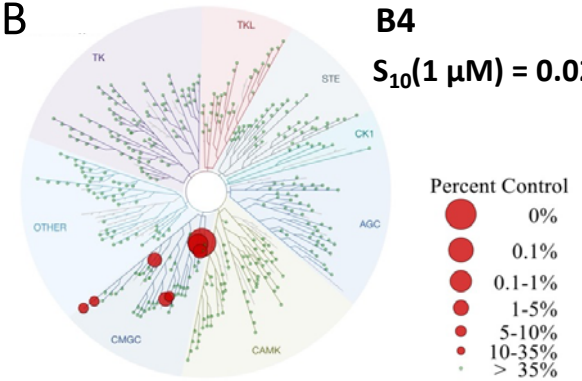

B4

S_{10}(1 μM) = 0.02

Kinase	DiscoverX PoC value	Assay format	IC_{50} value (nM)
GSK3A	0	Enzymatic and NB	11 and 120
CDKL5	0.2	Binding and NB	6.4 and 17
GSK3B	2.1	Enzymatic and NB	38 and 250
DYRK2	4.4	Enzymatic	240
CDK7	4.4	Enzymatic	>10000
PCTK1	6.3	Enzymatic	1200
DYRK1A	9.1	Enzymatic	900
PCTK2	9.5	Enzymatic	1600

C

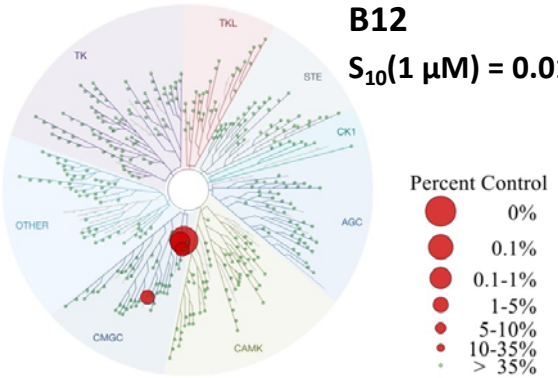

B12

S_{10}(1 μM) = 0.01

Kinase	DiscoverX PoC value	Assay format	IC_{50} value (nM)
GSK3A	0	Enzymatic and NB	16 and 190
CDKL5	0.6	Binding and NB	8.7 and 23
GSK3B	1.7	Enzymatic and NB	48 and 1200
DYRK2	4.6	Enzymatic	920
CDK7	17	Enzymatic	>10000
PCTK1	19	Enzymatic	1700
RPS6KA4	27	Enzymatic	>10000
DYRK1A	29	Enzymatic	4800
DYRK1B	34	Enzymatic	1700

Figure 3. Kinome-wide selectivity data for CDKL5 lead compounds. Kinome tree diagrams illustrate the selectivity of these compounds when profiled against 403 wild-type (WT) human kinases at 1 μM at Eurofins DiscoverX in their *scan*MAX panel. The percent control legend shows red circles of different sizes corresponding with percent control value each kinase binds the small molecule in this large binding panel. Also included are selectivity scores (S_{10}(1 μM)), which were calculated using the PoC values for WT human kinases in the *scan*MAX panel only. The S_{10} score is a way to express selectivity that corresponds with the percent of the kinases screened that bind with a PoC value <10. In the embedded tables kinases are listed by their gene names and ranked by their percent of control (PoC) value generated in the *scan*MAX panel. Rows colored green demonstrate enzymatic IC_{50} values within a 30-fold window of the CDKL5 binding IC_{50} value. Correlating assay format used to generate data in the last column of nested table is listed in the preceding column, with NB = NanoBRET.

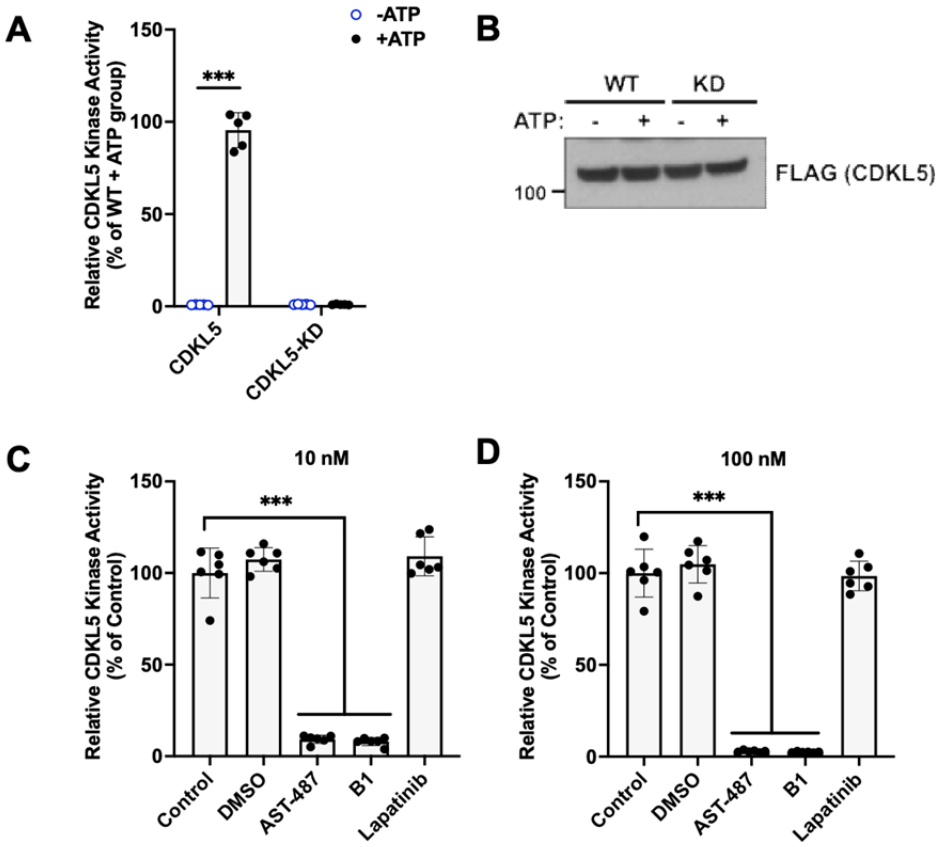

Figure 4. B1 potently inhibits the kinase activity of CDKL5. (A) Representative graph from a CDKL5 kinase assay demonstrating that purified WT human CDKL5 retains kinase activity, while the kinase dead (KD, CDKL5 K42R) human protein is functionally inactive (n = 3). (B) Representative western blot illustrating that equal expression of WT and KD proteins was observed in the kinase assay experiments. (C and D) Kinase assays using purified WT human CDKL5 in the presence of 10 or 100 nM of the indicated compounds (n = 3). One-way ANOVA with Dunnett's multiple comparison test used. *** = $p < 0.0001$ and non-significant comparisons not shown.

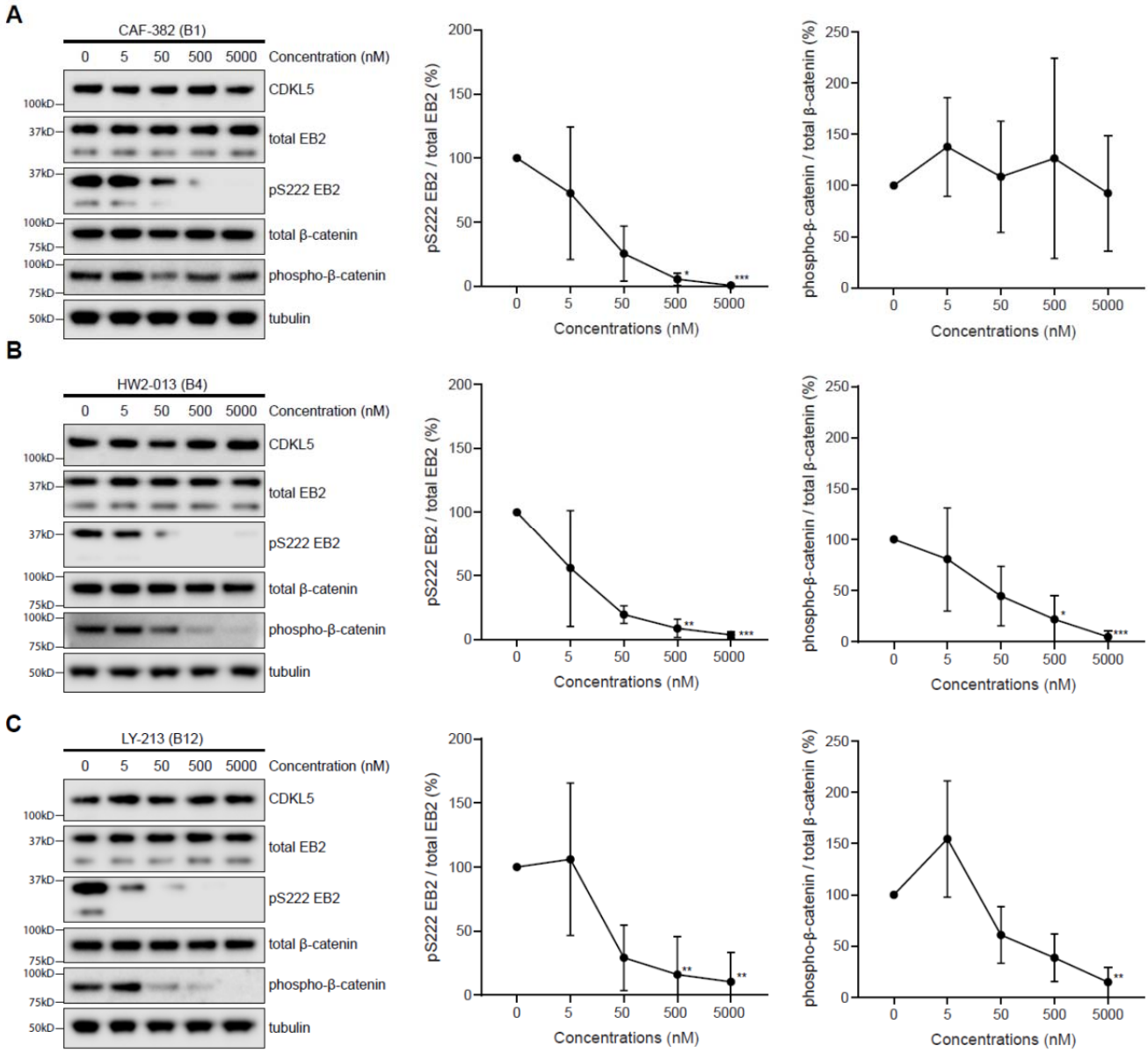

Figure 5. CAF-382 (**B1**), HW2-013 (**B4**), and LY-213 (**B12**) compounds reduce CDKL5 activity in rat primary neurons. HW2-013 (**B4**) and LY-213 (**B12**) also downregulate GSK3 activity. (A) Western blot and quantification showing expression of EB2 phosphorylation and β-catenin phosphorylation in DIV14-15 rat primary neurones after an hour treatment with different concentrations of CAF-382 (**B1**). (B) Western blot and quantification showing expression of EB2 phosphorylation and β-catenin phosphorylation in DIV14-15 rat primary neurons after an hour treatment with different concentrations of HW2-013 (**B4**). (C) Western blot and quantification showing expression of EB2 phosphorylation and β-catenin phosphorylation in DIV14-15 rat primary neurons after an hour treatment with different concentrations of LY-213 (**B12**). Each concentration was compared to the control using a Kruskal-Wallis test. n = 3 biological replicates with 2 repetitions. *p≤0.05. **p≤0.01. ***p≤0.001. Error bars are SD.

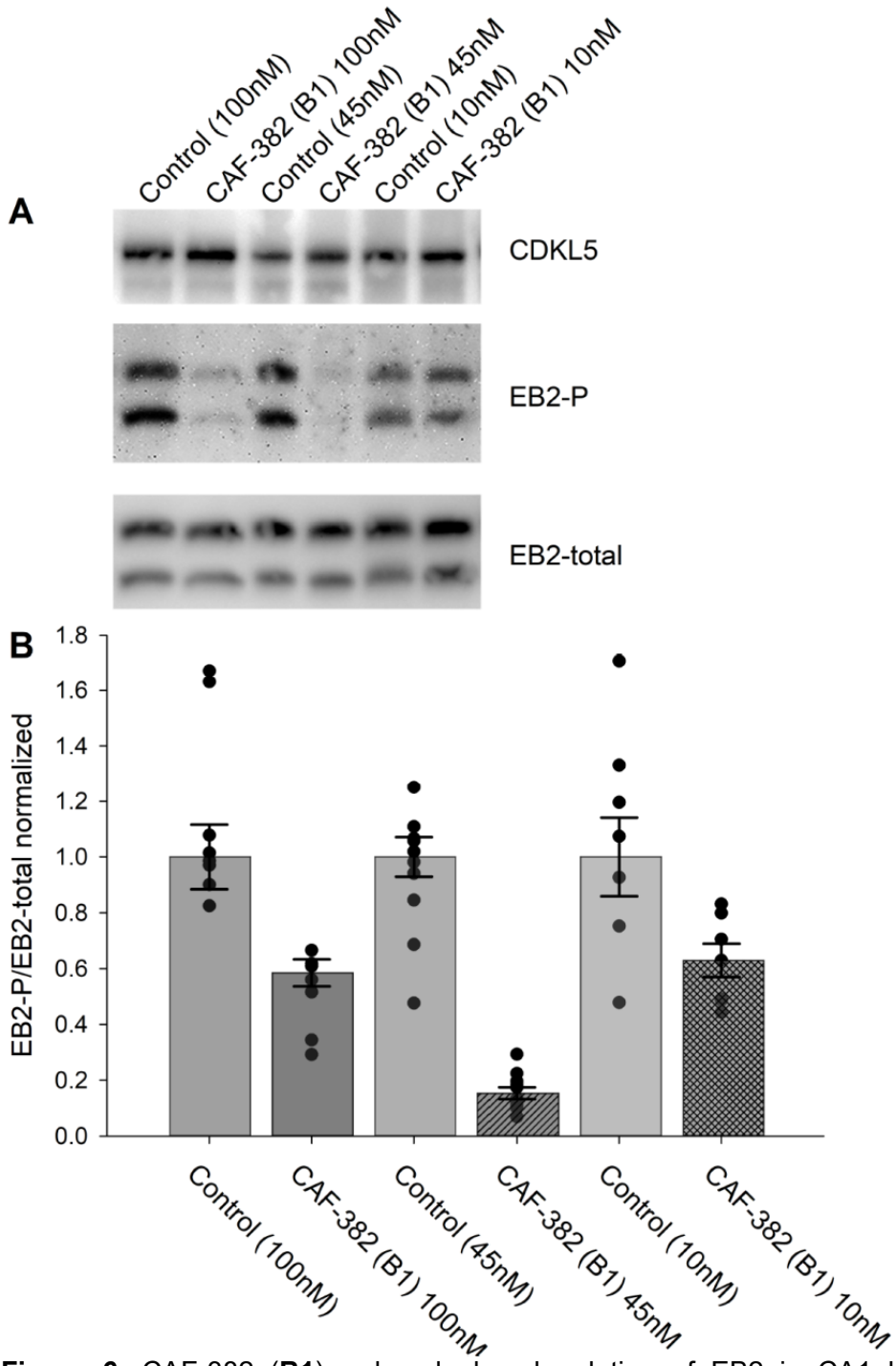

Figure 6. CAF-382 (**B1**) reduced phosphorylation of EB2 in CA1 hippocampal slices. (A) Example blots demonstrate no alterations in CDKL5 expression across treatments (stats in text) and suggest relative CAF-382 (**B1**) dose-dependent differences in EB2 phosphorylation. (B) Normalized quantification of EB2-phosphorylation (density of EB2-phosphorylation bands/ density of EB2-total bands). CAF 382 (**B1**) (control: 1±0.10 versus 100 nM: 0.49±0.02, n = 8, p = 0.002, RM-ANOVA) (control: 1±0.08 versus 45 nM: 0.16±0.03, n = 10, p < 0.001, RM-ANOVA) (control: 1± 0.14 versus 10 nM: 0.62± 0.11, n=7, p = 0.003, RM-ANOVA) reduced EB2 phosphorylation at all concentrations.

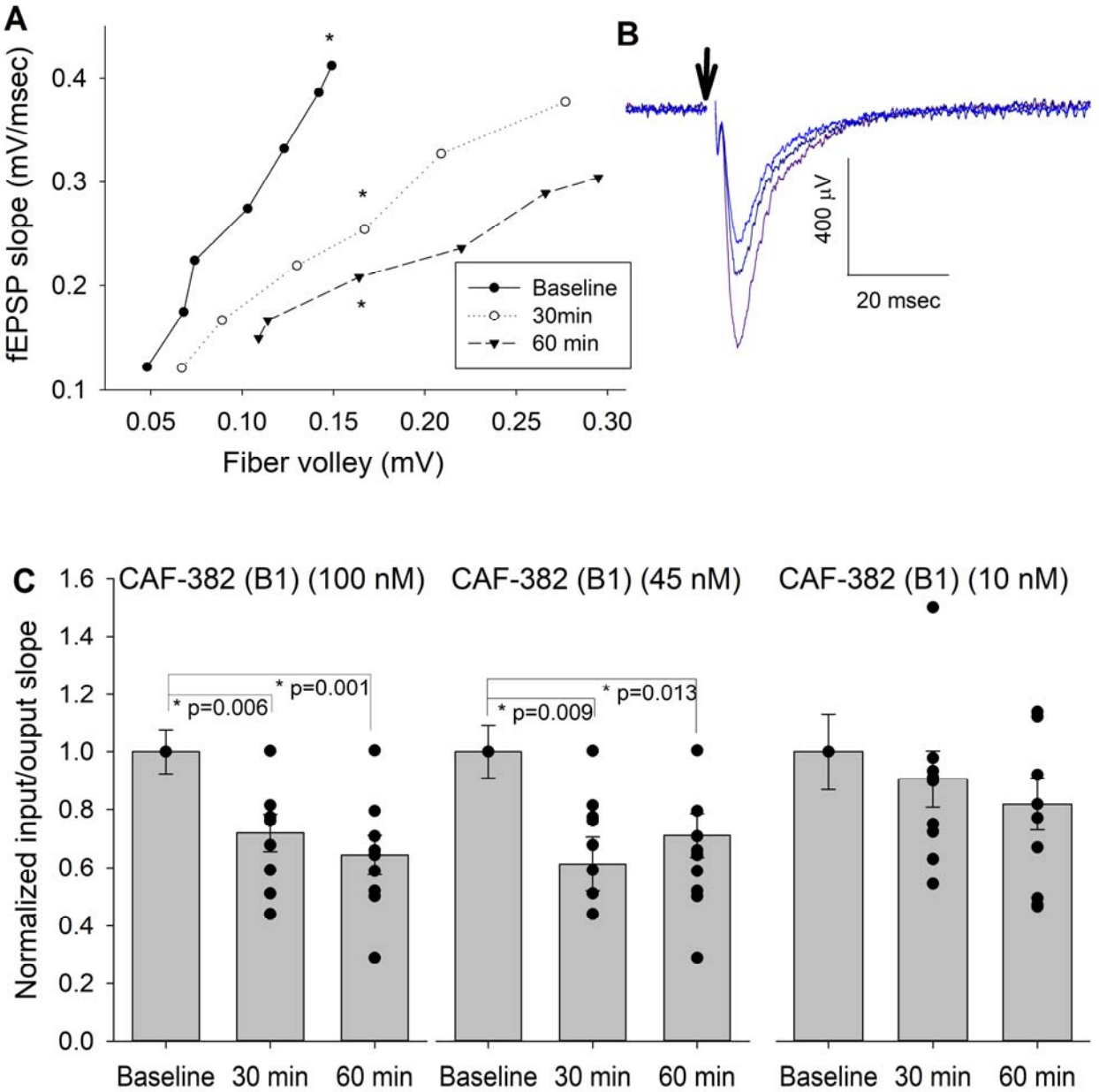

Figure 7. CAF-382 (**B1**) reduced post-synaptic fEPSP responsiveness, as measured by input-output curves. (A) Sample input (fiber volley) / output (fEPSP slope) (I/O) curves at baseline, 30 minutes and 60 minutes after CAF-382 (**B1**) (100nM) in a hippocampal slice. Slopes of I/O curves were obtained at baseline, and 30 minutes and 60 minutes after treatment with CAF-382 (**B1**). Asterisks indicate sample traces (B) from treated slice; stimulus artifact (arrow) has been removed for clarity. Initial negative deflection after the artifact is the fiber volley, followed by the fEPSP. (C) RM-ANOVA of I/O slopes of CAF-382 (**B1**) (100 nM and 45 nM) were significantly decreased after 30 minutes (100 nM: 1.91±0.23, n = 9, p = 0.006; 45 nM: 1.58±0.24, n=10, p = 0.013) and 60 minutes (100 nM: 2.00±0.30, n = 9, p = 0.001; 45 nM: 1.57±0.22, n=10, p = 0.009) compared to baseline (100 nM: 3.24±0.52, n = 9; 45 nM: 2.29±0.23, n=10). Baseline I/O slope was used to normalize each recording to allow comparisons across all treatments. CAF-382 (**B1**) (10 nM) did not alter I/O slopes after 30 or 60 minutes (RM-ANOVA, n = 9, p = 0.07). Error bars are SE.

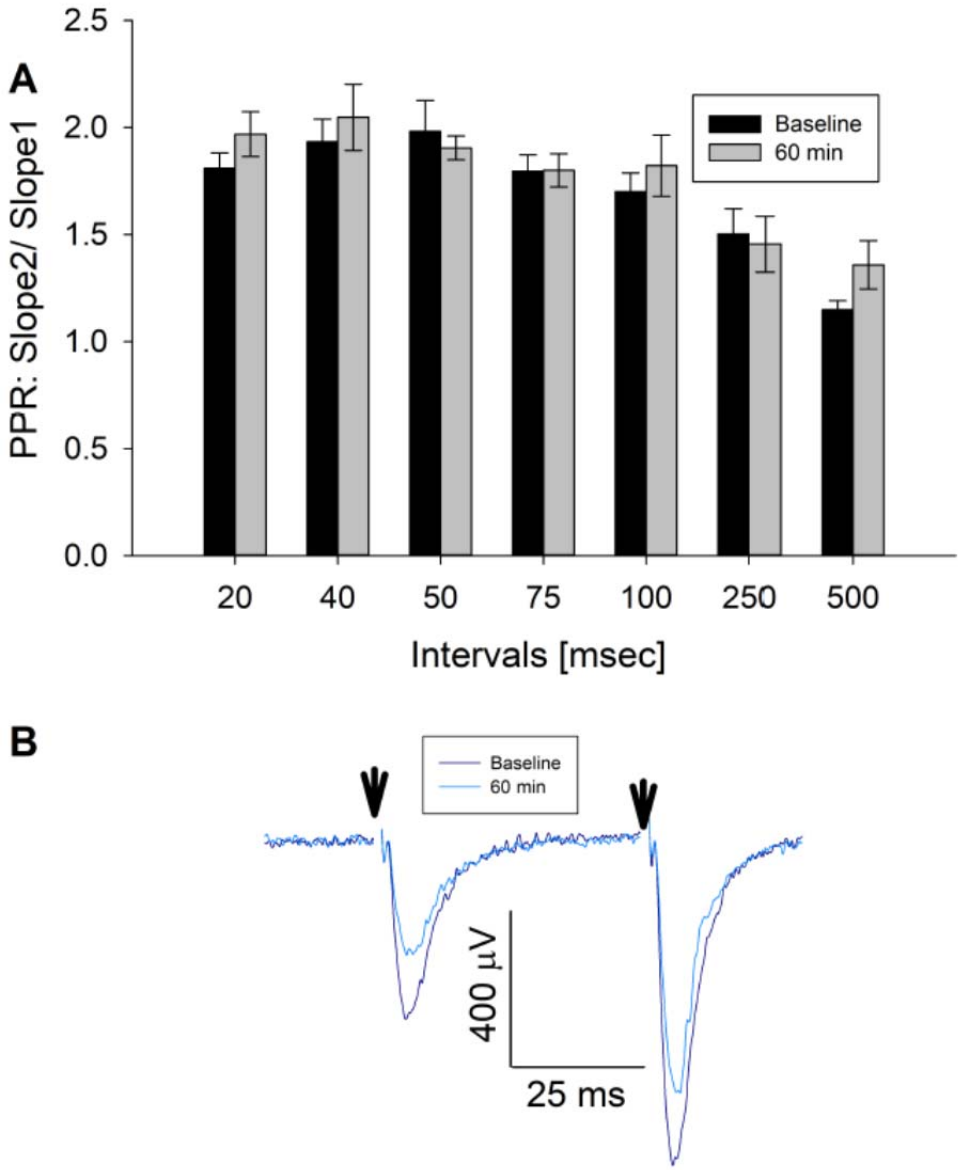

Figure 8. CAF-382 (**B1**) did not alter presynaptic release as measured by paired-pulse ratio. (A) Paired-pulse ratios (PPR) of fEPSPs (Slope of fEPSP2/Slope of fEPSP1), reflective of pre-synaptic release, were unaltered across a range of stimulus intervals (RM-ANOVA, n=7) by CAF-382 (**B1**) (100nM) for 60 minutes compared to baseline. (B) Sample trace for 50 ms interval. Reduction of initial fEPSP slopes were consistent with Figure 7. Stimulus artifacts (arrows) have been removed for clarity. Error bars are SE.

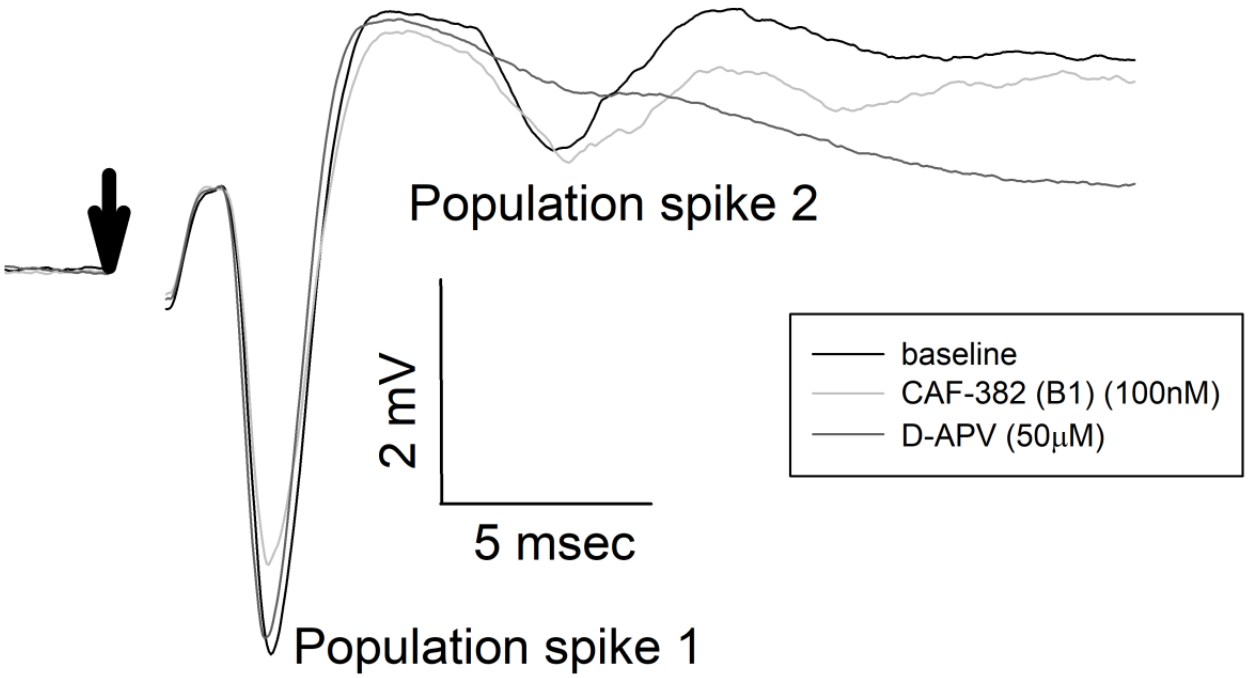

Figure 9. CAF-382 (**B1**) did not alter NMDAR-mediated component of fEPSPs. Maximal fEPSPs recorded in stratum pyramidale of CA1 with reduced extracellular Mg^{2+} demonstrate multiple population spikes; previous studies have demonstrated that secondary population spikes in these conditions are NMDAR-dependent[64]. CAF-382 (**B1**) (100 nM) did not alter population spike 1 (control -4.057±0.584mV, CAF-382 (**B1**) 3.929±0.736mV, n=10, p=0.742, RM-ANOVA) or NMDAR-mediated population spike 2 (control -2.093±0.568mV, CAF-382 (**B1**) -1.656±0.4442, n=10, p=0.867, RM-ANOVA). For comparison, the selective NMDAR antagonist D-APV (50 μM) completely blocked population spike 2, as previously reported [64]. Stimulation artifact has been removed (arrow) for clarity.

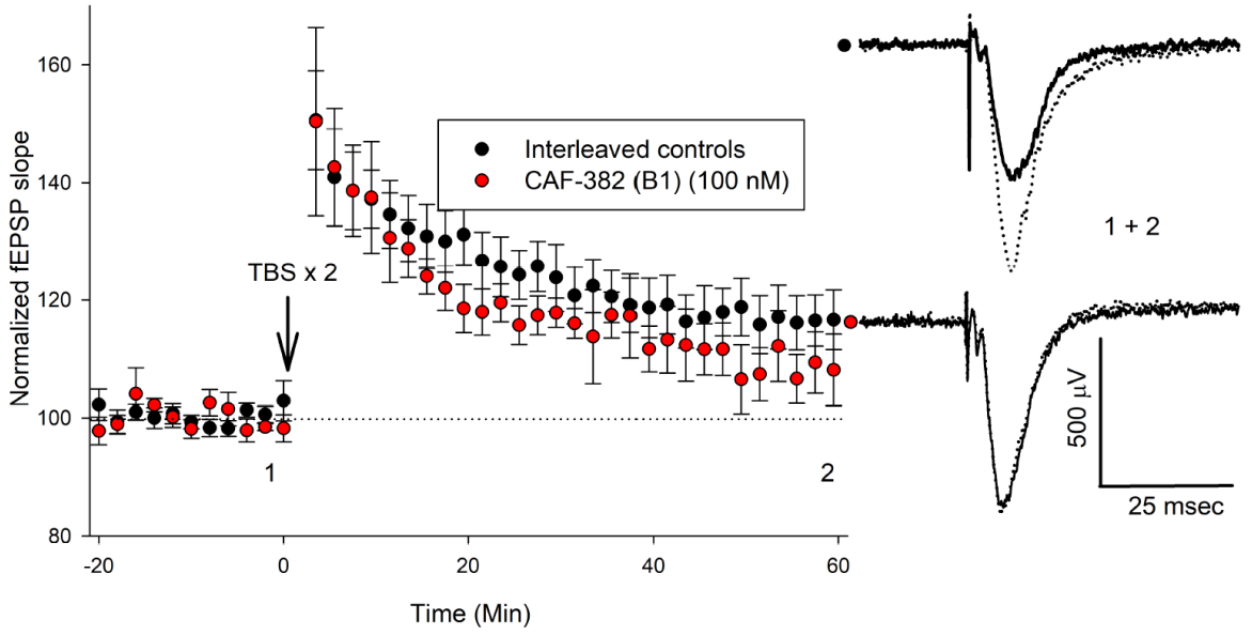

Figure 10. CAF-382 (**B1**) acutely reduces the expression of LTP in CA1 hippocampus. Hippocampal slices were initially incubated in CAF-382 (**B1**) for at least 30 minutes and then continuously perfused with CAF-382 (**B1**) (100 nM). fEPSP slope was normalized to initial baseline, expressed as 100% (dotted line); mean±SEM shown. Following stable baseline of fEPSP slope (> 20 minutes), LTP was induced by two theta-burst (TBS) trains. Compared to interleaved control slices, CAF-382 (**B1**) significantly reduced LTP as measured by fEPSP slope at 56-60 minutes post theta-burst (control: 115.6±2.2 n = 13 slices, 12 rats; CAF-382 (**B1**): 106.4±3.5, n = 5 slices, 4 rats; p = 0.029, 2-way ANOVA, Holm-Sidak post-hoc). Sample traces for control (black filled circle) and CAF-382 (**B1**) (red filled circle) before (1, solid trace) and after LTP (2, dotted trace) are shown to the right. Error bars are SE.

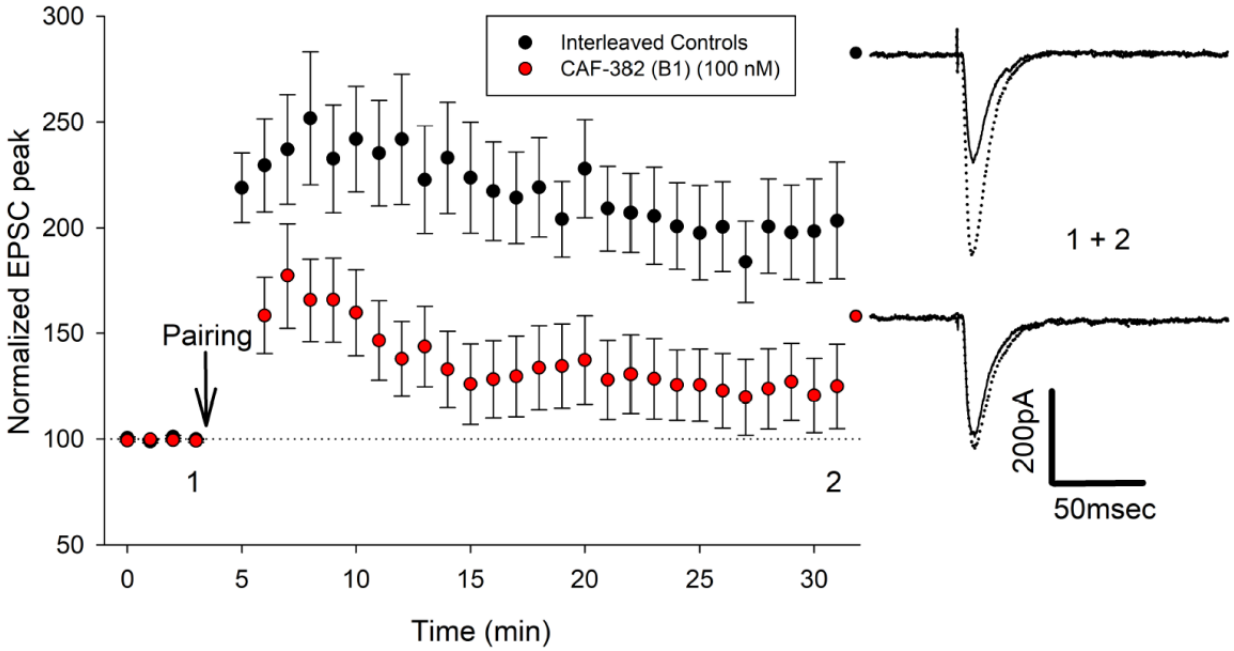

Figure 11. CAF-382 (**B1**) acutely reduces the expression of LTP mediated by AMPA-type glutamate receptors in CA1 hippocampus. Hippocampal slices were initially incubated in CAF-382 (**B1**) (100 nM) for at least 60 minutes prior to recording. Peak negative current of AMPA-type glutamate receptor mediated synaptic responses were normalized to initial baseline post break-in (time = 0), expressed as 100% (dotted line); mean±SEM shown. Following baseline, LTP was induced by a pairing protocol. Compared to interleaved control slices, CAF-382 (**B1**) significantly reduced LTP at 27-31 minutes post break-in (control: 197.5±8.4 n = 14 slices, 14 rats; CAF-382 (**B1**): 123.14±9.0, n = 12-13 slices, 13 rats; $p < 0.001$, 2-way ANOVA, Holm-Sidak post-hoc). Sample traces for control (black filled circle) and CAF-382 (**B1**, red filled circle) before (1, solid trace) and after LTP (2, dotted trace) are shown to the right. Error bars are SE.

1020 **Table 1**. Solubility and microsomal stability data for **B1**

Compound	Kinetic solubility		Mouse liver microsomal stability (%)		
	μM	μg/mL	T = 0 min	T = 30 min	T = 30 min (-NADPH)
B1	196.8[a]	72.1[a]	100	86.1	87.5

1021 [a] Measured solubility is >75% dose concentration, actual solubility may be higher.
1022

1023
1024

Supplementary Information

Synthesis of key compounds. Chemistry General Information. Reagents were purchased from reputable commercial vendors and used in accordance with safety data sheets. A rotary evaporator was employed to remove solvent(s) under reduced pressure (*in vacuo*). Thin layer chromatography (TLC) as well as LC–MS were used to monitor reaction progress. The following abbreviations are used in experimental procedures: mmol (millimoles), µmol (micromoles), µL (microliters), mg (milligrams), equiv (equivalent(s)), min (minutes), and h (hours). ^{1}H NMR and ^{13}C NMR spectra as well as microanalytical data were collected for a key intermediate and final compound **B1** to confirm their identity and evaluate their purity prior to initiating cell- and animal-based studies. ^{1}H and ^{13}C NMR spectra were collected in DMSO-d_6 using Bruker spectrometers. Magnet strength is indicated in each corresponding line listing. Peak positions are included in parts per million (ppm) and calibrated versus the shift of DMSO-d_6; coupling constants (*J* values) are noted in hertz (Hz); and multiplicities are included as follows: singlet (s), doublet (d), pentet of doublets (pd), and multiplet (m).

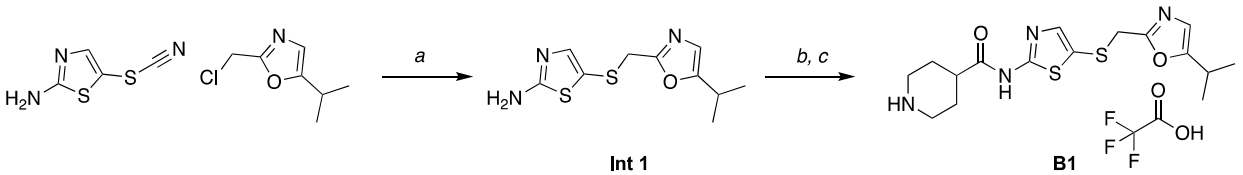

Scheme 1. Preparation of compound **B1**. a) EtOH, $NaBH_4$, acetone, 80 °C, 1 h, 57% yield; b) HATU, DIPEA, 1-(*tert*-butoxycarbonyl)piperidine-4-carboxylic acid, DMF; c) TFA, CH_2Cl_2, 36% yield over two steps.

*5-(((5-isopropyloxazol-2-yl)methyl)thio)thiazol-2-amine (**Int 1**)*. To a flask was added 5-thiocyanatothiazol-2-amine (400 mg, 1.0 equiv, 2.5 mmol) in EtOH (24 mL), followed by addition of $NaBH_4$ (183 mg, 1.9 equiv, 4.8 mmol) portion-wise at room temperature. The mixture was stirred for 1 h at room temperature then acetone (12 mL) was added. After 1 hr, a solution of 2-(chloromethyl)-5-isopropyloxazole (412 mg, 1.0 equiv, 2.6 mmol) in EtOH (4mL) was added, and the reaction was heated at 80 °C for 1 h. The resulting mixture was cooled, concentrated *in vacuo*, and then partitioned between EtOAc and brine. The organic phase was separated, dried with $MgSO_4$, and concentrated *in vacuo* to give a crude solid. The crude material was triturated with diethyl ether/hexane to provide the desired product 4-(((5-isopropyloxazol-2-yl)methyl)thio)thiazol-2-amine as a red oil (368 mg, 57 %).

*N-(5-(((5-isopropyloxazol-2-yl)methyl)thio)thiazol-2-yl)piperidine-4-carboxamide 2,2,2-trifluoroacetate (**B1**).* To a flask was added 1-(*tert*-butoxycarbonyl)piperidine-4-carboxylic acid (99 mg, 1.1 equiv, 431 μmol) and DIPEA (205 μL, 3 equiv, 1.2 mmol) and HATU (194 mg, 1.3 equiv, 509 μmol) and the flask was stirred at room temperature for approximately 15 min. Next, 5-(((5-isopropyloxazol-2-yl)methyl)thio)thiazol-2-amine (100 mg, 1.0 equiv, 392 μmol) was added and the reaction was stirred at room temperature for 16 h. The reaction mixture was concentrated and purified by column chromatography (SiO_2, MeOH 0–10% in CH_2Cl_2) to yield the desired product as a white solid to yield the intermediate *tert*-butyl 4-((5-(((5-isopropyloxazol-2-yl)methyl)thio)thiazol-2-yl)carbamoyl)piperidine-1-carboxylate. To this intermediate was added 20% TFA and CH_2Cl_2 (5 mL) and the reaction stirred for 1 h. The reaction was concentrated *in vacuo* and after addition of MeOH a white precipitate crashed out. The solid was filtered under vacuum to yield the desired product *N*-(5-(((5-isopropyloxazol-2-yl)methyl)thio)thiazol-2-yl)piperidine-4-carboxamide 2,2,2-trifluoroacetate as a white solid (20 mg). The remaining crude material was purified by preparative HPLC (MeOH 10–100% in H_2O (+0.05% TFA)) to yield the desired product *N*-(5-(((5-isopropyloxazol-2-yl)methyl)thio)thiazol-2-yl)piperidine-4-carboxamide 2,2,2-trifluoroacetate (**B1**) as a white solid (32 mg). Yield over two steps *N*-(5-(((5-isopropyloxazol-2-yl)methyl)thio)thiazol-2-yl)piperidine-4-carboxamide 2,2,2-trifluoroacetate (52 mg, 36 %). ^{1}H NMR (400 MHz, DMSO-d_6) δ 7.38 (s, 1H), 6.72 (d, J = 1.1 Hz, 1H), 4.03 (s, 2H), 3.21 (d, J = 12.8 Hz, 2H), 2.93 – 2.85 (m, 1H), 2.84 – 2.75 (m, 2H), 2.70 (s, 1H), 1.89 (d, J = 13.6 Hz, 2H), 1.77 – 1.63 (m, 2H), 1.12 (d, J = 6.9 Hz, 6H). ^{13}C NMR (214 MHz, DMSO-d_6) δ 172.45, 161.00, 158.76, 158.31, 145.12, 120.91, 119.04, 42.48, 38.65, 34.03, 25.29, 24.83, 20.48. HPLC purity: >95%. HRMS Calculated for $[M+H]^+$ $C_{16}H_{23}N_4O_2S_2$: 367.1184; observed $[M+H]^+$: 367.1248.

Figure S1. Characterization of N-(5-(((5-isopropyloxazol-2-yl)methyl)thio)thiazol-2-yl)piperidine-4-carboxamide 2,2,2-trifluoroacetate (**B1**) A) ^{1}H Spectra and chemical structure (inset). B) ^{13}C Spectra C) HPLC-UV Trace D) HRMS Trace.

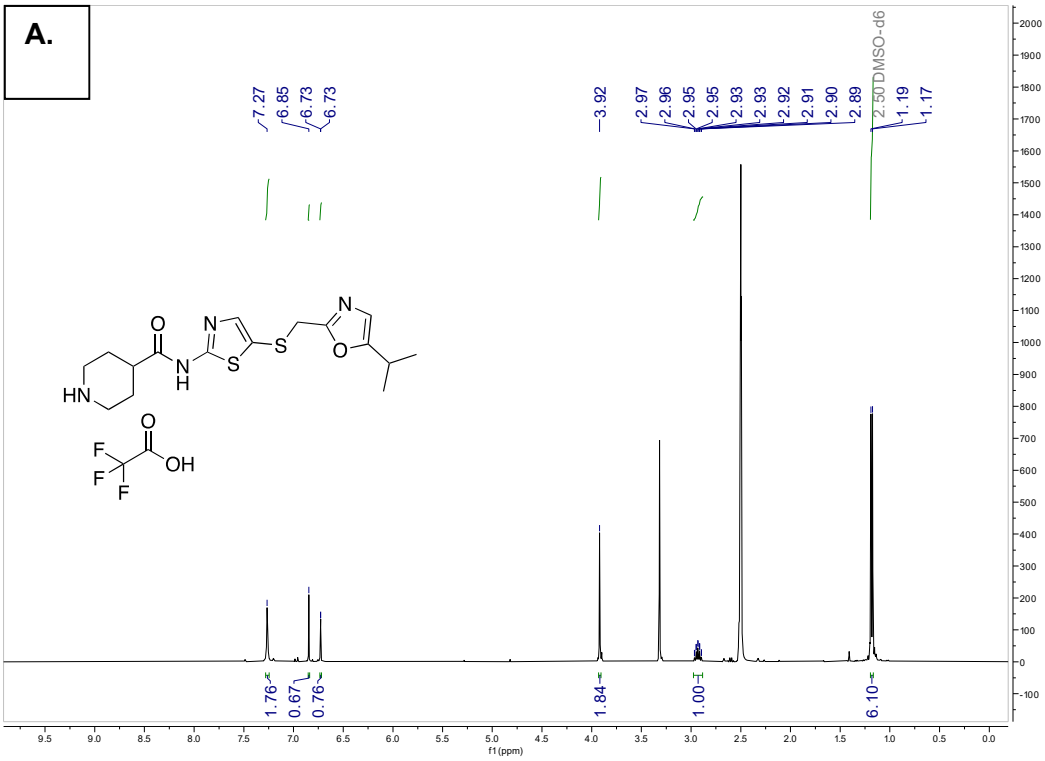

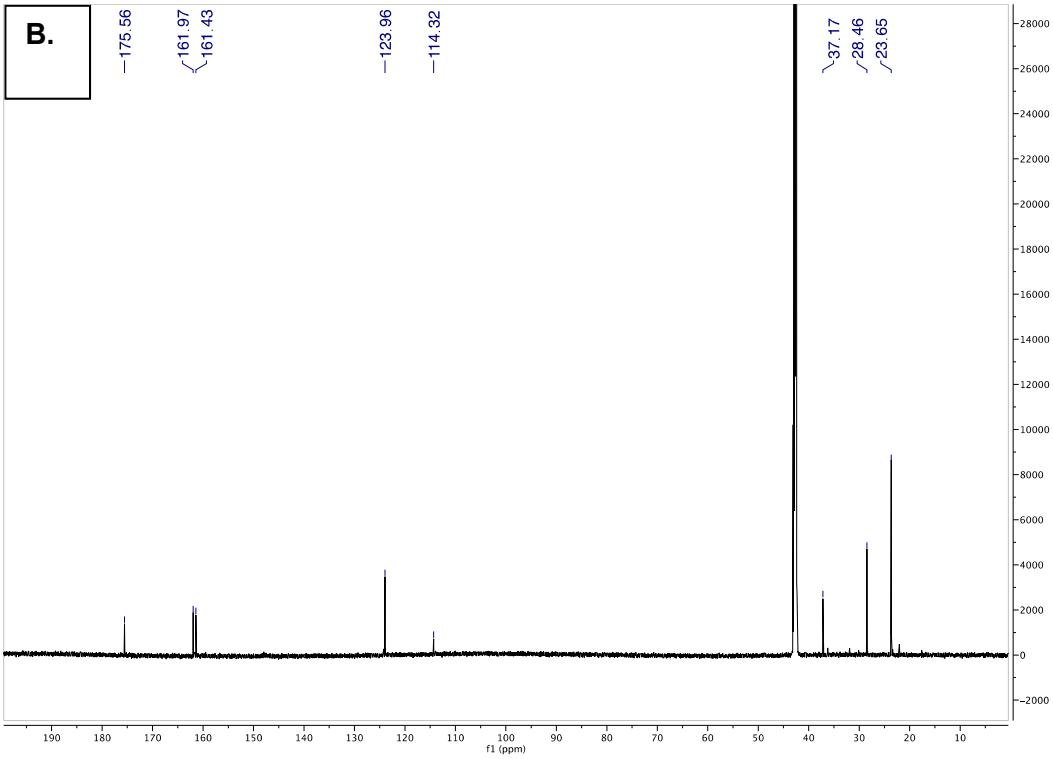
B.
175.56
161.97
161.43
123.96
114.32
37.17
28.46
23.65
f1 (ppm)

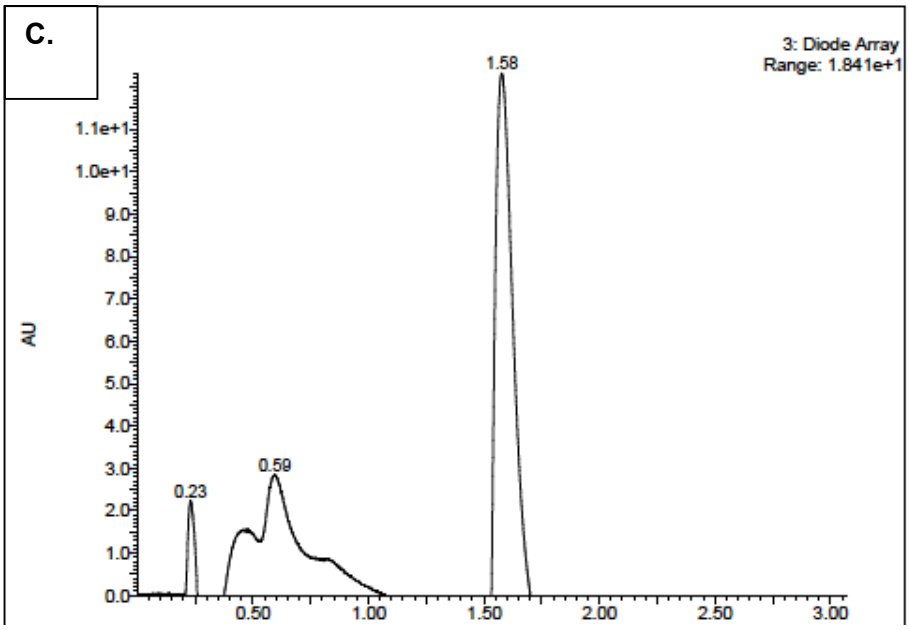
C.
3: Diode Array
Range: 1.841e+1
AU
0.23
0.59
1.58

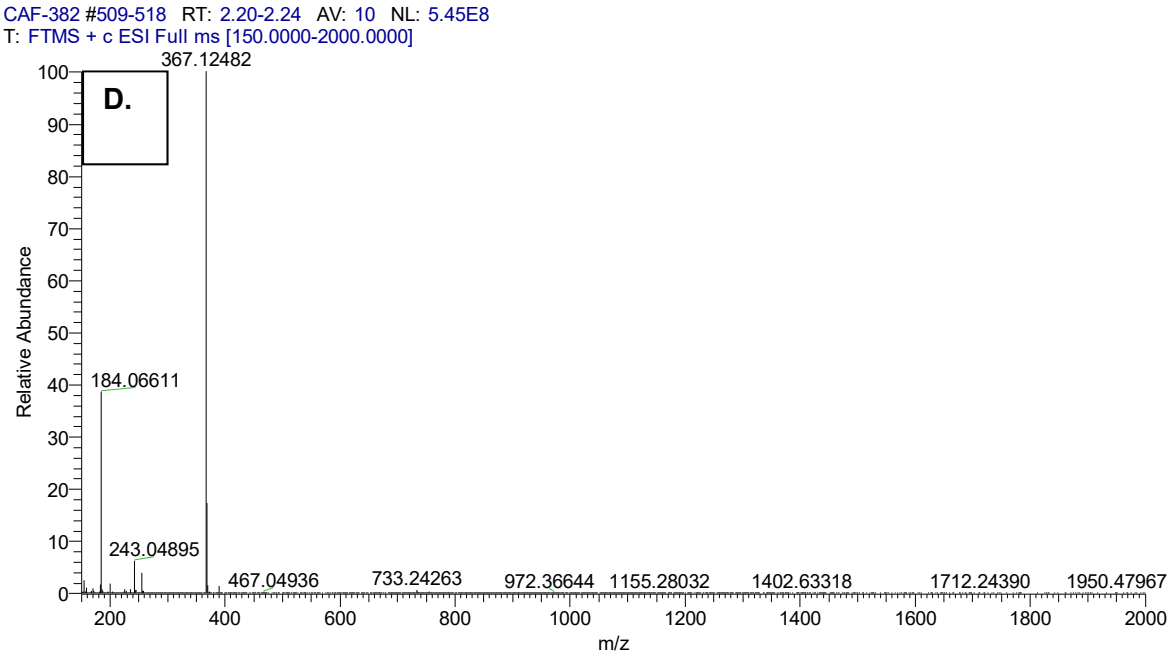

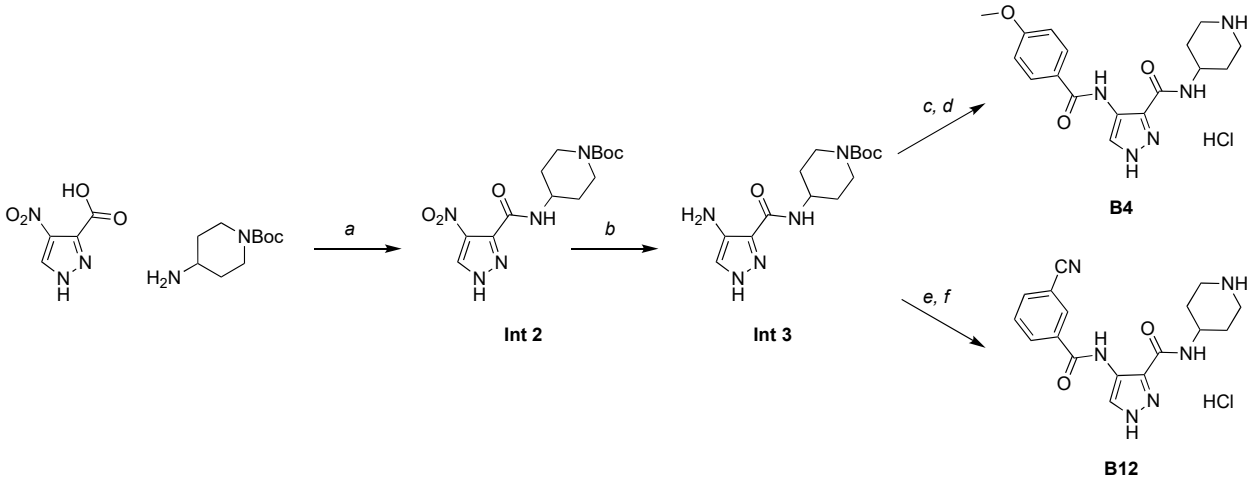

Scheme 2. Preparation of compounds **B4** and **B12**. a) Propylphosphonic anhydride (T3P), DIPEA, THF, 0°C, 1 h, 93% yield; b) Palladium on carbon (Pd/C), MeOH, THF, 25°C, 16 h, 99% yield; c) 4-methoxybenzoic acid, HATU, DIPEA, THF, 25°C, 17 h, 72% yield; d) HCl, dioxane, 25°C, 1h, 58% yield; e) 3-cyanobenzoic acid, T3P, DIPEA, THF, 25°C, 16 h; f) HCl, dioxane, 25°C, 1h, 39% yield over two steps.

1100 General procedure for preparation **B4** and **B12**: To a flask was added 4-nitro-1*H*-pyrazole-3-
1101 carboxylic acid (1.00 g, 1.0 equiv, 6.4 mmol), 1-Boc-4-aminopiperidine (1.28 g, 1.0 equiv, 6.4
1102 mmol), and DIPEA (4.21 mL, 4.0 equiv, 25.5 mmol) in THF (20 mL). The reaction mixture was
1103 cooled to 0°C, and then T3P (6.08 mL, 1.5 equiv, 9.5 mmol) was slowly added. After stirring for
1104 1 h at 0°C, the reaction mixture was concentrated *in vacuo*, and then partitioned between EtOAc
1105 and brine. The organic phase was separated, dried with $MgSO_4$, and concentrated *in vacuo* to
1106 give a crude solid. The crude material was purified using an automated purification system
1107 (SiO_2) 90%/10% hexanes/EtOAc to 100% EtOAc to give *tert*-butyl 4-(4-nitro-1*H*-pyrazole-3-
1108 carboxamido)piperidine-1-carboxylate (**Int 2**) as an amorphous solid (2.00 g, 93% yield).

1109 Palladium on carbon (5%, 31.3 mg, 0.1 equiv, 0.295 mmol) was added to *tert*-butyl 4-(4-
1110 nitro-1*H*-pyrazole-3-carboxamido)piperidine-1-carboxylate (**Int 2**, 1.0 g, 1.0 equiv, 2.95 mmol) in
1111 a mixture of methanol (10 mL) and THF (3.0 mL). The solution was placed under an
1112 atmosphere of H_2 at room temperature. After 16h, the solution was filtered through SiO_2 and the
1113 eluent was concentrated to afford *tert*-butyl 4-(4-amino-1*H*-pyrazole-3-carboxamido)piperidine-
1114 1-carboxylate (**Int 3**) as an amorphous solid (900 mg, 99% yield).

1115 To a flask was added *tert*-butyl 4-(4-amino-1*H*-pyrazole-3-carboxamido)piperidine-1-
1116 carboxylate (**Int 3**, 1 equiv) and the corresponding carboxylic acid (1.2 equiv) and DIPEA (4.0
1117 equiv) in THF (0.5 M) at room temperature. The reaction mixture was then treated slowly with
1118 T3P (3.0 equiv). After stirring for 16–17 h, the reaction mixture was concentrated *in vacuo*, and
1119 then partitioned between EtOAc and brine. The organic phase was separated, dried with
1120 $MgSO_4$, and concentrated *in vacuo* to give a crude solid. The crude material was purified using
1121 an automated purification system (SiO_2) 90%/100% hexanes/EtOAc to 100% EtOAc) to give an
1122 intermediate, which was stirred in HCl/dioxane (3.3 mL) for 1 h at room temperature. Solvent
1123 was removed and the crude material was purified using an automated purification system (SiO_2)
1124 90%/100% hexanes/EtOAc to 100% EtOAc) to give the desired product (**B4** or **B12**) as an
1125 amorphous solid (39–42% yield over 2 steps).

1126 *4-(4-methoxybenzamido)-N-(piperidin-4-yl)-1H-pyrazole-3-carboxamide* (**B4**) ^{1}H NMR
1127 (850 MHz, Methanol-d_4) δ 8.30 (s, 1H), 7.89 (d, J = 8.8 Hz, 2H), 7.07 (d, J = 8.8 Hz, 2H), 4.22
1128 (tt, J = 10.8, 4.1 Hz, 1H), 3.89 (s, 3H), 3.48 (dt, J = 13.4, 3.9 Hz, 2H), 3.18 (td, J = 12.7, 3.1 Hz,
1129 2H), 2.22 (dd, J = 14.3, 3.9 Hz, 2H), 1.96 – 1.85 (m, 2H). ^{13}C NMR (214 MHz, Methanol-d_4) δ
1130 165.66, 165.58, 164.53, 134.00, 130.01, 126.71, 124.57, 121.57, 115.24, 56.06, 45.26, 44.25,
1131 29.54. ^{1}H NMR purity: >95%. HRMS Calculated for $[M + H]^+$ $C_{17}H_{22}N_5O_3$: 344.1723; observed
1132 $[M+H]^+$: 344.1717.

Figure S2. Characterization of 4-(4-methoxybenzamido)-N-(piperidin-4-yl)-1H-pyrazole-3-carboxamide (**B4**) A) ^{1}H Spectra and chemical structure (inset). B) ^{13}C Spectra C) HRMS Trace.

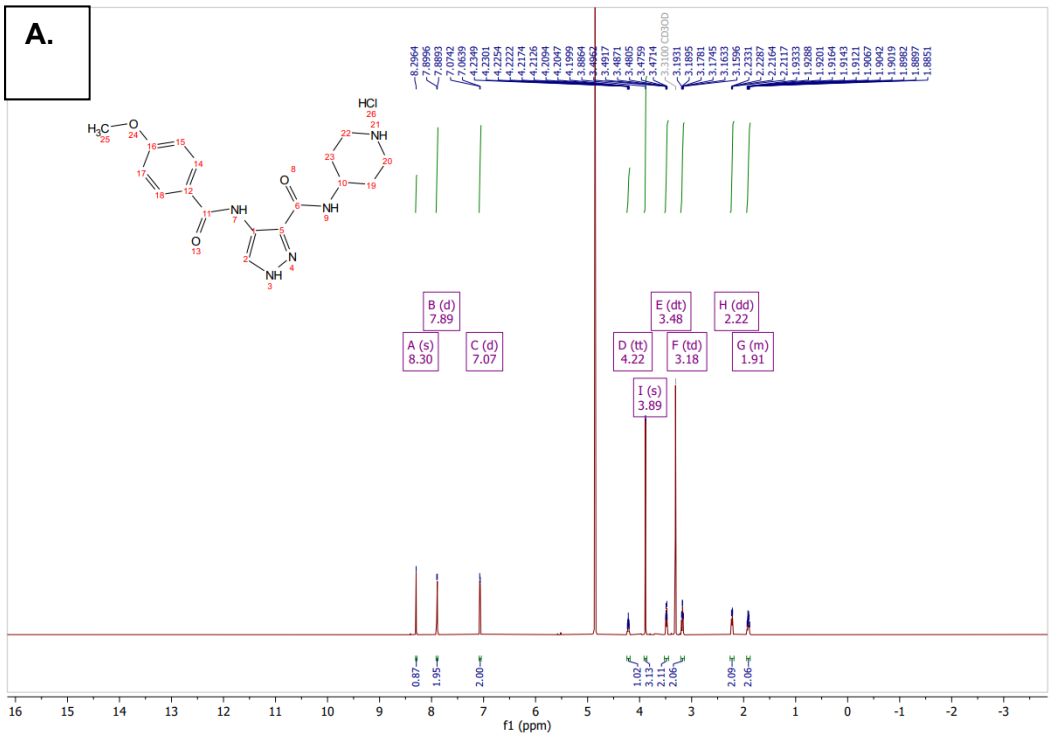

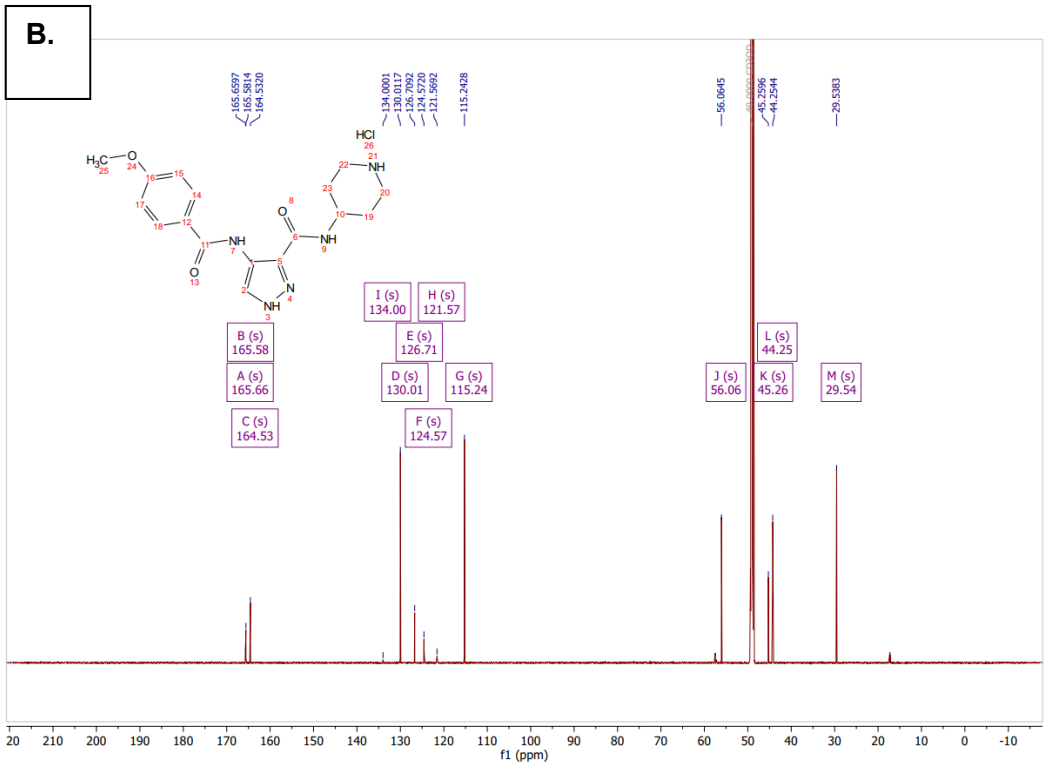

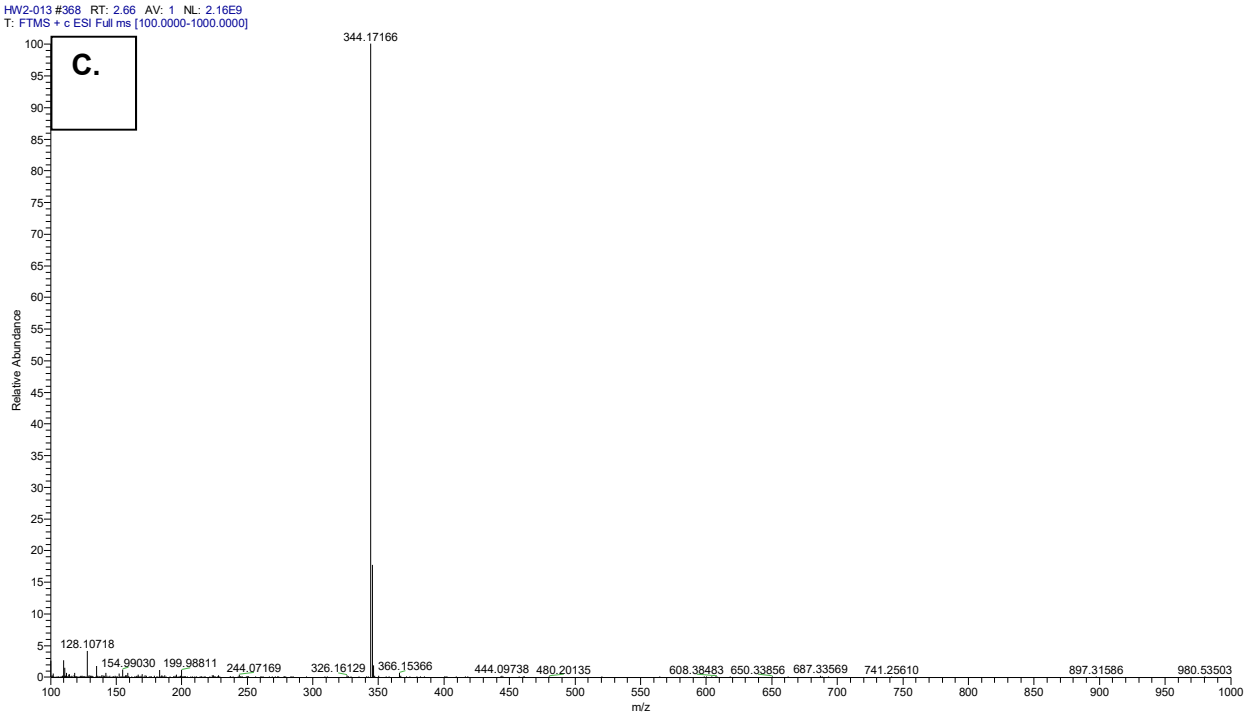

4-(3-cyanobenzamido)-N-(piperidin-4-yl)-1H-pyrazole-3-carboxamide (**B12**) ^{1}H NMR (850 MHz, Methanol-d_4) δ 8.33 (s, 1H), 8.26 (t, *J* = 1.7 Hz, 1H), 8.22 (dt, *J* = 7.9, 1.5 Hz, 1H), 7.97 (dt, *J* = 7.7, 1.4 Hz, 1H), 7.75 (t, *J* = 7.8 Hz, 1H), 4.22 (tt, *J* = 10.9, 4.1 Hz, 1H), 3.49 (dt, *J* = 14.1, 3.5 Hz, 2H), 3.18 (td, *J* = 12.9, 3.1 Hz, 2H), 2.22 (dd, *J* = 14.2, 3.7 Hz, 2H), 1.95 – 1.88 (m, 2H). ^{13}C NMR (214 MHz, Methanol-d_4) δ 165.57, 163.51, 136.50, 136.14, 134.35, 132.50, 131.84, 131.32, 124.01, 122.04, 118.88, 114.39, 45.33, 44.29, 29.53. ^{1}H NMR purity: >95%. HRMS Calculated for $[M + H]^+$ $C_{17}H_{19}N_6O_2$: 339.1569; observed $[M+H]^+$: 339.1563.

Figure S3. Characterization of 4-(3-cyanobenzamido)-N-(piperidin-4-yl)-1H-pyrazole-3-carboxamide (**B12**) A) ^{1}H Spectra and chemical structure (inset). B) ^{13}C Spectra C) HRMS Trace.

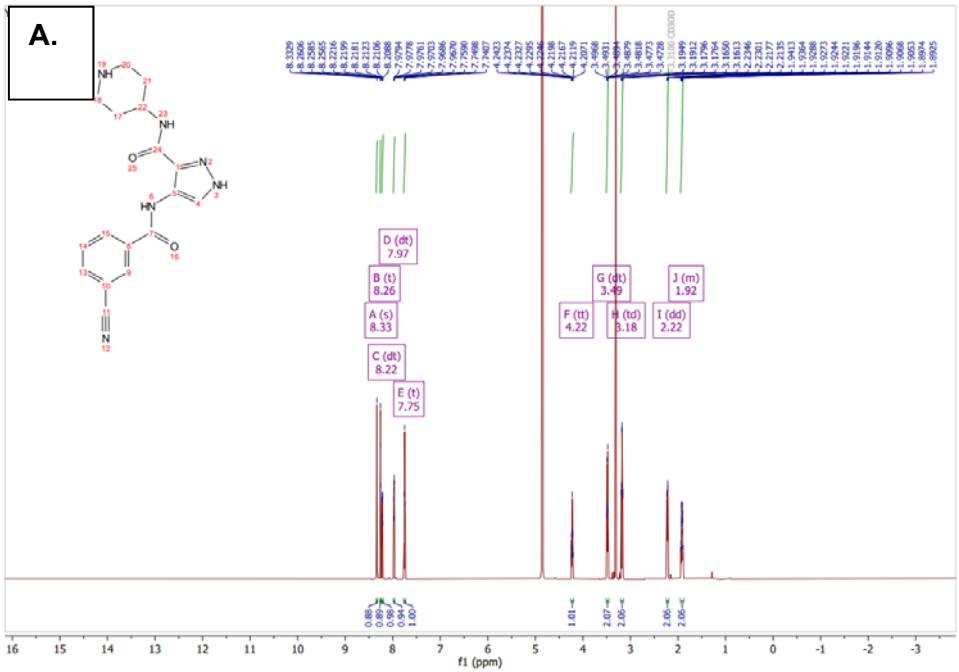

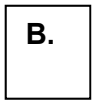

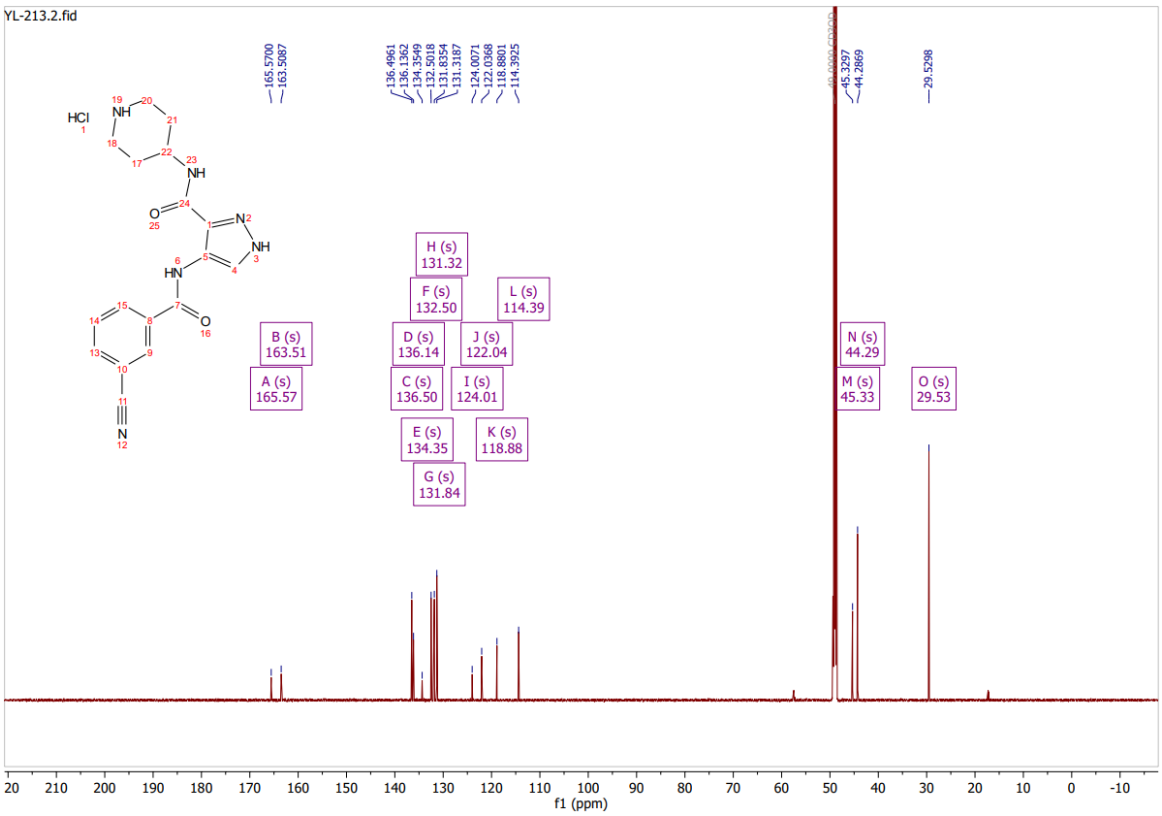

1156

1157

1158

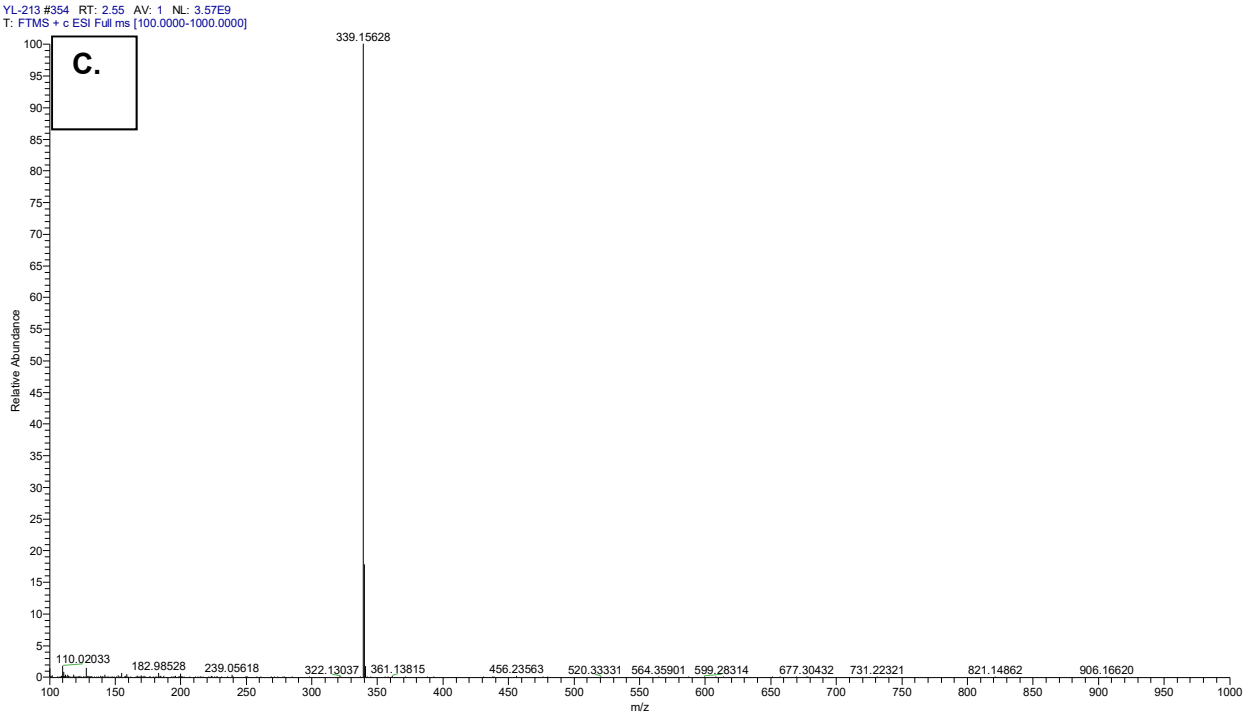

1159

1164 **Table S1.** NanoBRET data corresponding to compounds selected for initial study.

Compound	Parent	CDKL5 NB IC_{50} (nM)	GSK3β NB IC_{50} (nM)	fold
A01	AT-7519	363	>10,000	27.5
A02	AT-7519	178	4135	23.2
A03	AT-7519	19	404.8	21.3
A04	SNS-032	108	5688	52.7
A05	AT-7519	12	308.2	25.7
A06	SNS-032	221	7787	35.2
A07	AT-7519	6	192	32.0
A08	AT-7519	56	1374	24.5
A09	AT-7519	21	481	22.9
A10	SNS-032	424	>10,000	23.6
A11	AT-7519	9	3699	411.0
A12	AT-7519	20	524.8	26.2
B01	SNS-032	8	>10,000	1250.0
B02	SNS-032	190	9100	47.9
B03	SNS-032	10	>10,000	1000.0
B04	AT-7519	14	553.9	39.6
B05	SNS-032	388	8000	20.6
B06	AT-7519	155	8193	52.9
B07	AT-7519	36	3256	90.4
B08	AT-7519	161	>10,000	62.1
B09	AT-7519	37	3627	98.0
B10	AT-7519	90	4945	54.9
B11	AT-7519	141	3101	22.0
B12	AT-7519	69	3631	52.6
C01	SNS-032	323	>10,000	31.0

1165

1166

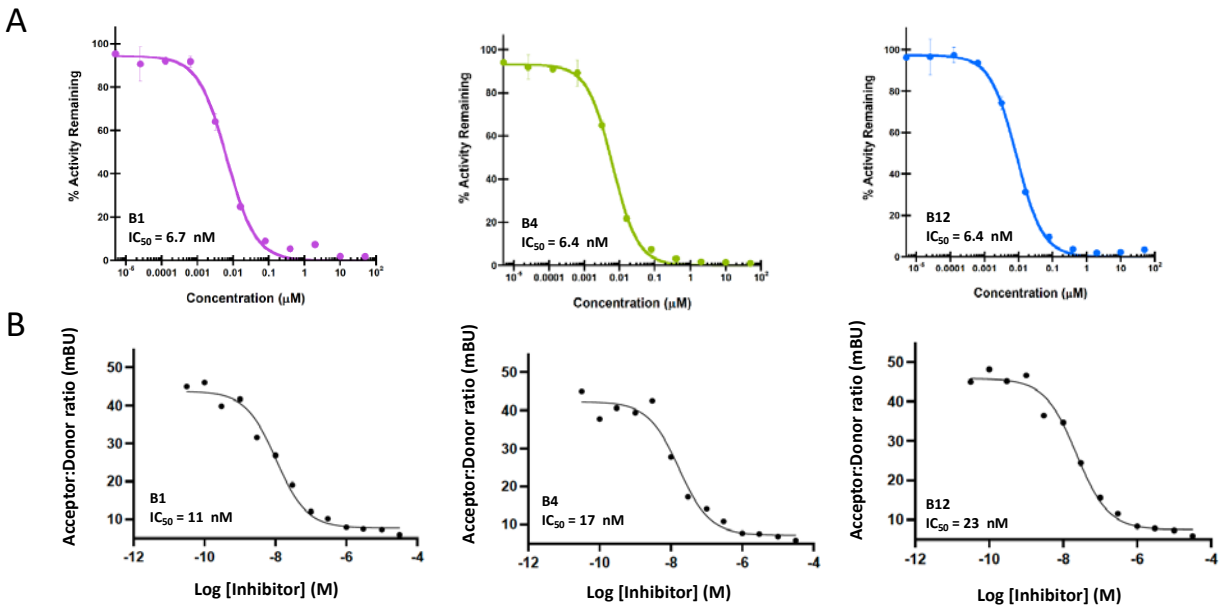

Figure S4. Curves corresponding with CDKL5 affinity measurements in Figure 2. (A) Curves generated in CDKL5 split-luciferase assay for B1, B4, and B12. (B) Curves generated in CDKL5 NanoBRET assay for B1, B4, and B12.

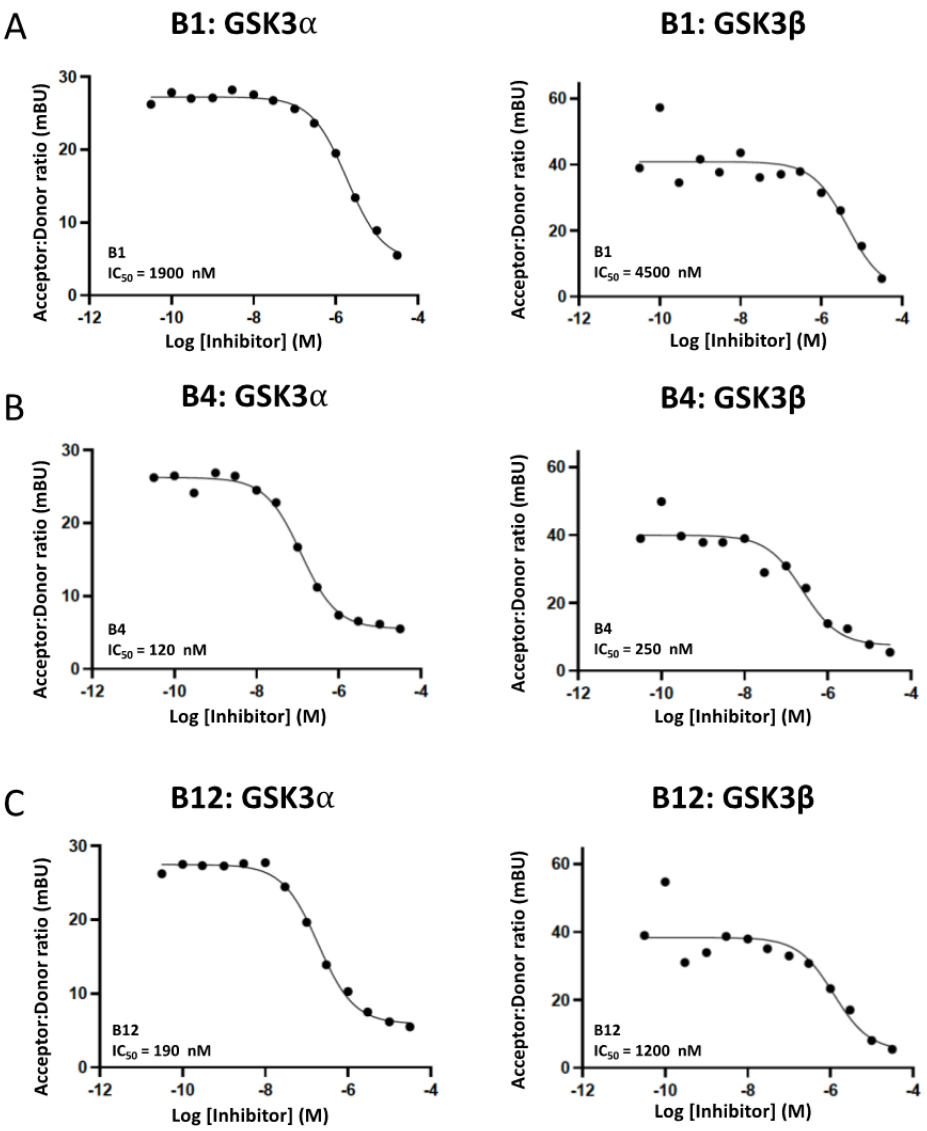

Figure S5. Curves corresponding with GSK3 NanoBRET measurements in Figure 2. (A) Curves generated in GSK3α and GSK3β NanoBRET assays for B1. (B) Curves generated in GSK3α and GSK3β NanoBRET assays for B4. (C) Curves generated in GSK3α and GSK3β NanoBRET assays for B12.

1177

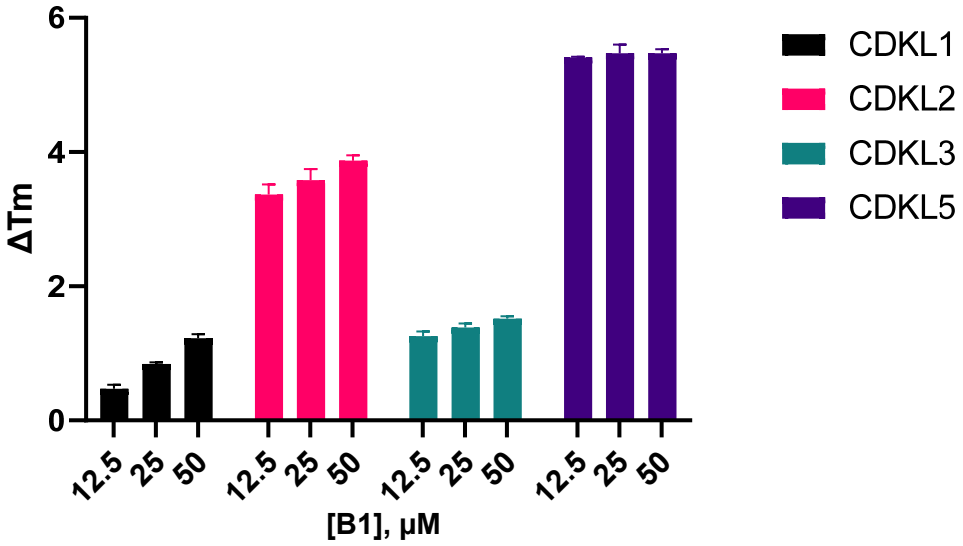

1178

1179

1180 **Figure S6.** CDKL family selectivity evaluation via thermal shift assays.

1181

1182

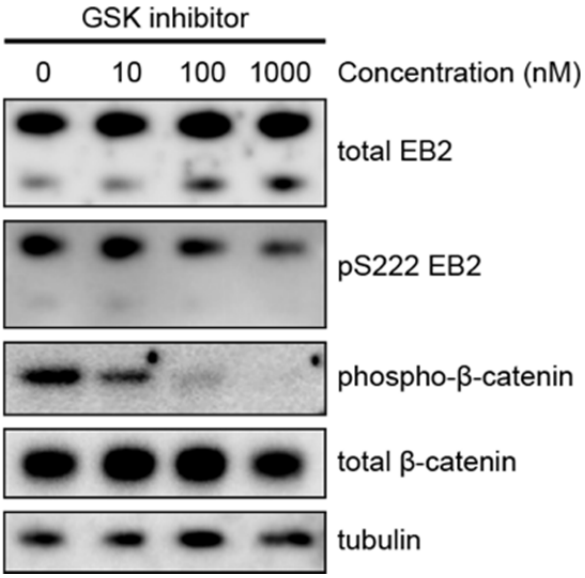

1183

1184

1185 **Figure S7.** Phosphorylation of β-catenin, a substrate of GSK, is reduced upon treatment with a
1186 GSK inhibitor CHIR 99021 (Tocris) but EB2 phosphorylation is not changed. Western blot
1187 showing expression of total EB2, pS222 EB2, total β-catenin, phospho-β-catenin and tubulin in
1188 DIV14-15 rat primary neurones after an hour treatment with a GSK inhibitor.

1189

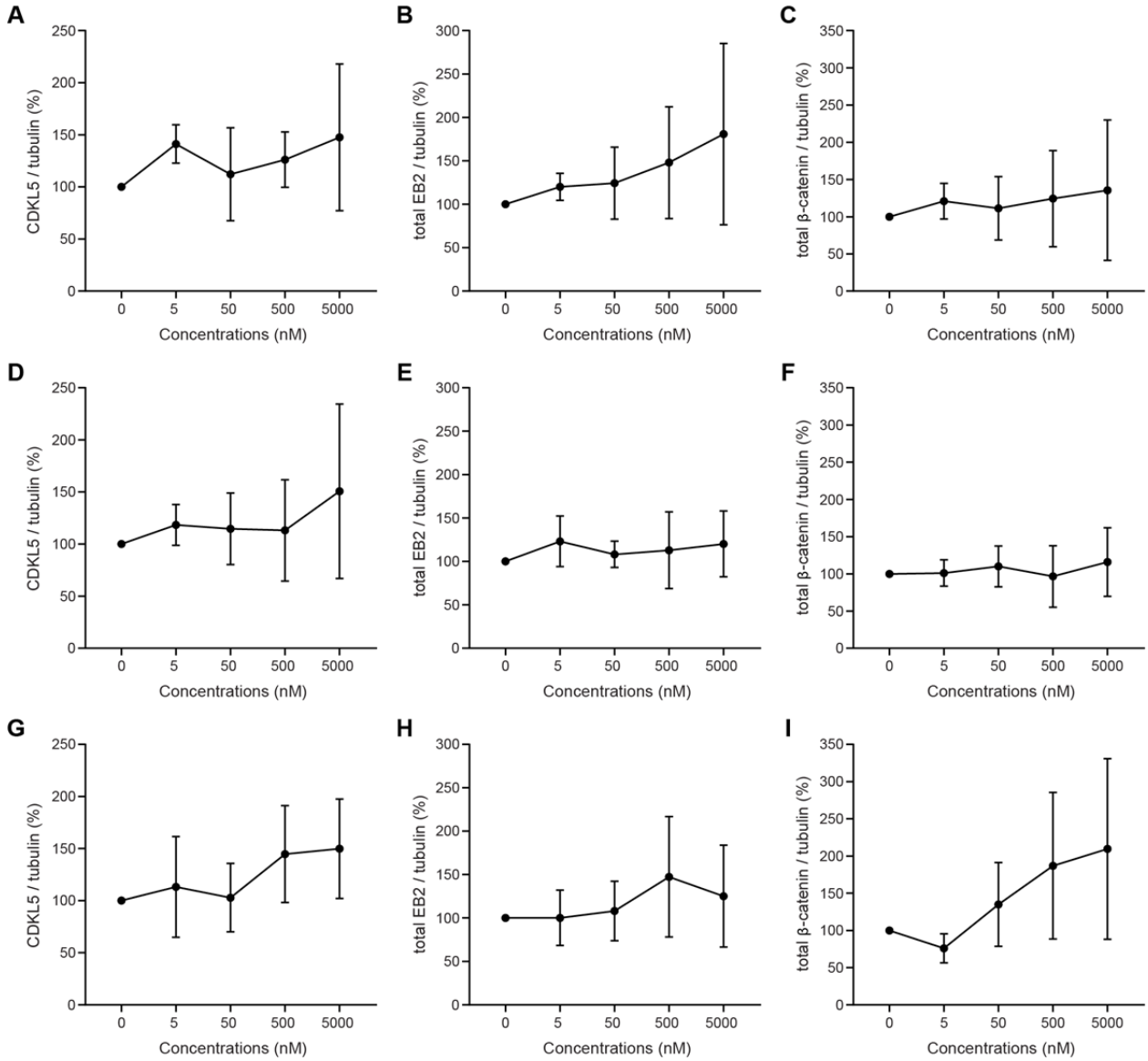

Figure S8. CDKL5, total EB2 and β-catenin expression in rat primary neurons after treatment with CAF-382, HW2-013 and LY-213 compounds. A, D, G, Quantification of CDKL5 expression in DIV14-15 rat primary neurones after an hour treatment with different concentrations of CAF-382, HW2-013 and LY-213 compounds respectively. Each concentration was compared to the control using a one-way ANOVA test. N = 3 biological replicates with 2 repetitions. Error bars are SD. B, E, H, Quantification of total EB2 expression in DIV14-15 rat primary neurones after an hour treatment with different concentrations of CAF-382, HW2-013 and LY-213 compounds respectively. Each concentration was compared to the control using a one-way ANOVA test. N = 3 biological replicates with 2 repetitions. Error bars are SD. C, F, I, Quantification of total β-

1201 catenin expression in DIV14-15 rat primary neurones after an hour treatment with different
1202 concentrations of CAF-382, HW2-013 and LY-213 compounds respectively. Each concentration
1203 was compared to the control using a one-way ANOVA test. N = 2 biological replicates with 2
1204 repetitions. Error bars are SD.

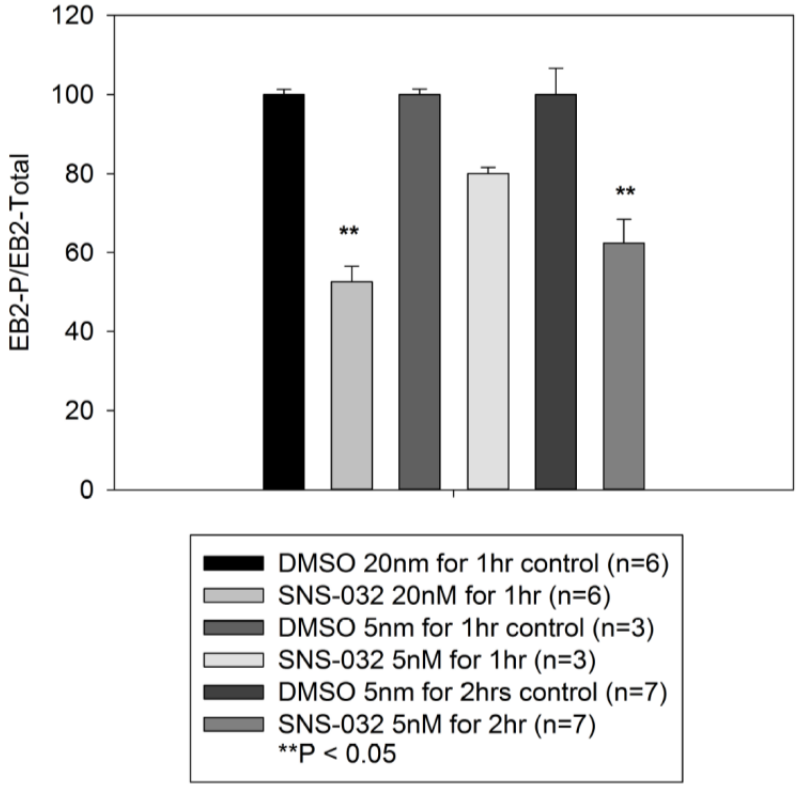

1205

1206

1207 **Figure S9.** SNS-032 (Selleck Chemicals) inhibits phosphorylation of EB2 in rat hippocampal
1208 slices in a time and concentration-dependent fashion. Effect of SNS-032 is compared to control
1209 slices with similar concentration of DMSO vehicle under three different conditions. Compare to
1210 Figure 6.

1211

1212

A

Time (h)	Concentration (ng/mL)
0.5	508
1	317
2	79.1
4	17.3

B

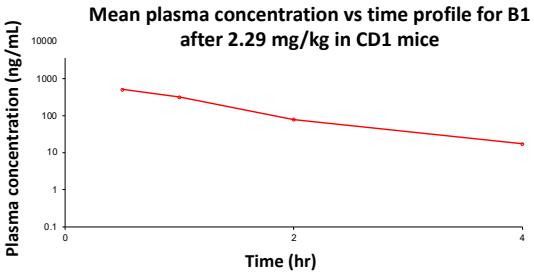

C

PK parameters	Unit	Mean
T1/2	h	0.738
Tmax	h	0.500
Cmax	ng/mL	508
AUC_{last}	h*ng/mL	628
AUC_{Inf}	h*ng/mL	646
$AUC_{_\%Extrap_}$obs	%	2.85
$MRT_{Inf_}$obs	h	1.18
AUC_{last}/D	h*mg/mL	274
F	%	NA

1213
1214 **Figure S10.** Snapshot pharmacokinetic (PK) results for B1. (A) Plasma concentration
1215 measurements at timepoints post-administration. (B) Plot of mean plasma concentration over
1216 the time course of the PK study. (C) Summary of B1 PK properties (n = 2).

1217

1218

A

IP dose: 2.29 mg/kg

Time (h)	Brain Conc (ng/g)	Plasma (ng/mL)	Ratio (Brain/plasma)
1	15.6	340	0.0459

B

IP dose: 7.63 mg/kg

Time (h)	Brain Conc (ng/g)	Plasma (ng/mL)	Ratio (Brain/plasma)
1	158	750	0.210*

1219

1220

1221 **Table S2.** Brain exposure results for B1. (A) Brain/plasma concentration-time data after 2.29
1222 mg/kg dose. (B) Brain/plasma concentration-time data after 7.63 mg/kg dose. *One animal
1223 artificially drove up blood/plasma ratio. N = 3 per dose.

1224

1225

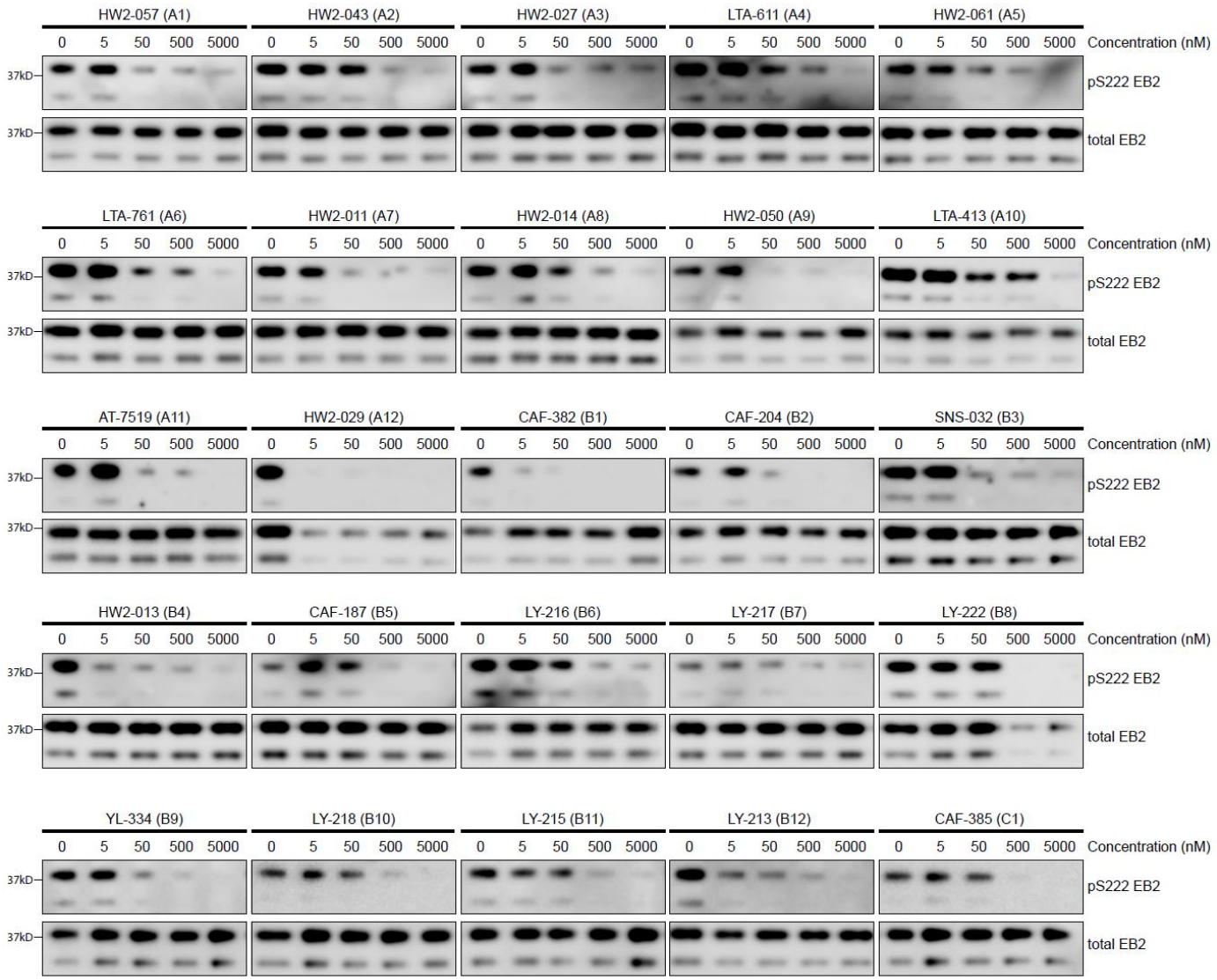

Figure 1. Screening of CDKL5 inhibitors in rat primary neurons using Western blotting. Western blots showing expression of total EB2 and levels of Ser222 EB2 phosphorylation in DIV14-16 rat primary neurons upon treatment of 1 hour with 5 nM, 50 nM, 500 nM and 5000 nM of selected CDKL5 inhibitors.

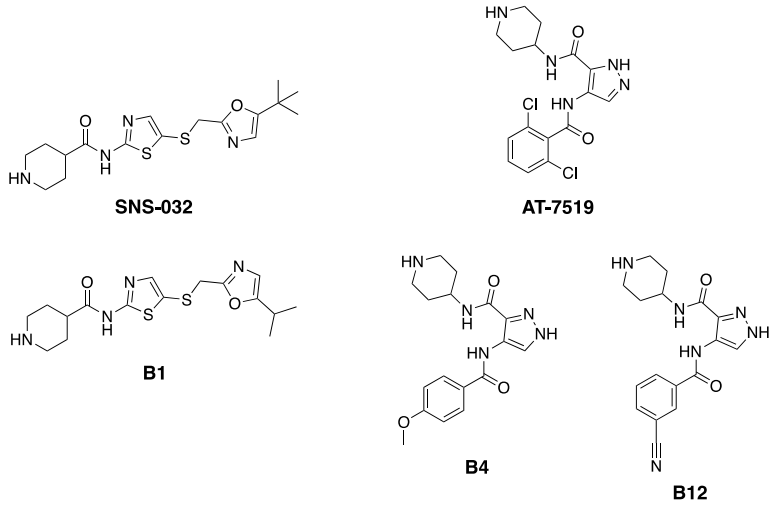

Figure 2. Structures of CDKL5 inhibitor leads and corresponding parent compounds.

A

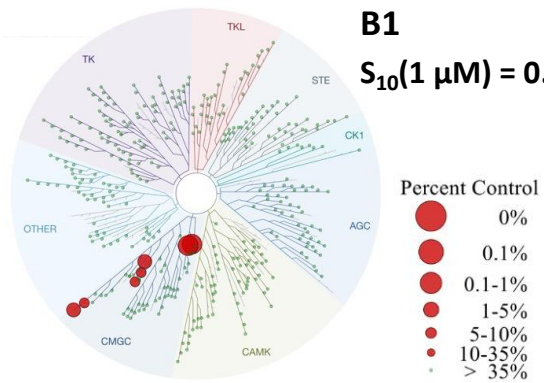

B1

S_{10}(1 µM) = 0.017

Kinase	DiscoverX PoC value	Assay format	IC_{50} value (nM)
GSK3A	0.7	Enzymatic and NB	470 and 1900
CDKL5	0.7	Binding and NB	6.7 and 11
PCTK2	1.3	Enzymatic	89
CDK7	1.9	Enzymatic	300
PCTK1	5.5	Enzymatic	62
CDC2L5	5.9	Enzymatic	>10000
CDK9	8.3	Enzymatic	20
YSK4	14	Enzymatic	>10000
PCTK3	17	Enzymatic	100
CDK4	20	Enzymatic	1900
GSK3B	51	Enzymatic and NB	2200 and 4500

B

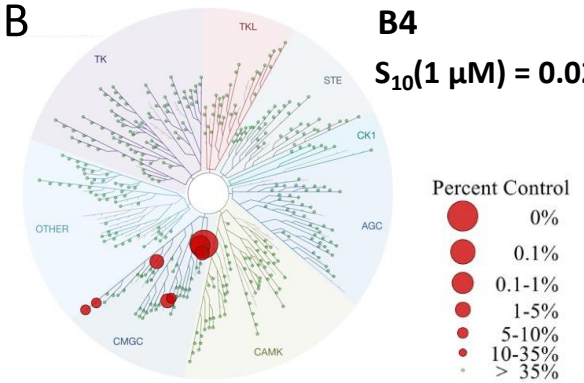

B4

S_{10}(1 µM) = 0.02

Kinase	DiscoverX PoC value	Assay format	IC_{50} value (nM)
GSK3A	0	Enzymatic and NB	11 and 120
CDKL5	0.2	Binding and NB	6.4 and 17
GSK3B	2.1	Enzymatic and NB	38 and 250
DYRK2	4.4	Enzymatic	240
CDK7	4.4	Enzymatic	>10000
PCTK1	6.3	Enzymatic	1200
DYRK1A	9.1	Enzymatic	900
PCTK2	9.5	Enzymatic	1600

C

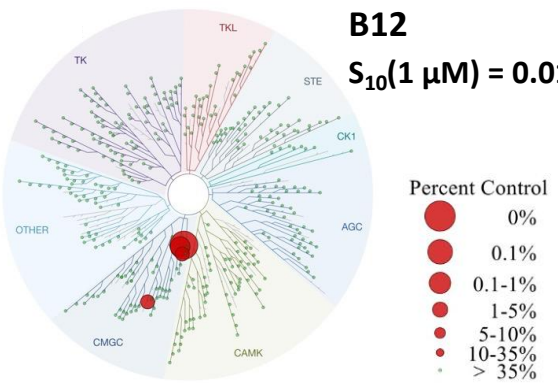

B12

S_{10}(1 µM) = 0.01

Kinase	DiscoverX PoC value	Assay format	IC_{50} value (nM)
GSK3A	0	Enzymatic and NB	16 and 190
CDKL5	0.6	Binding and NB	8.7 and 23
GSK3B	1.7	Enzymatic and NB	48 and 1200
DYRK2	4.6	Enzymatic	920
CDK7	17	Enzymatic	>10000
PCTK1	19	Enzymatic	1700
RPS6KA4	27	Enzymatic	>10000
DYRK1A	29	Enzymatic	4800
DYRK1B	34	Enzymatic	1700

Figure 3. Kinome-wide selectivity data for CDKL5 lead compounds. Kinome tree diagrams illustrate the selectivity of these compounds when profiled against 403 wild-type (WT) human kinases at 1 µM at Eurofins DiscoverX in their *scan*MAX panel. The percent control legend shows red circles of different sizes corresponding with percent control value each kinase binds the small molecule in this large binding panel. Also included are selectivity scores (S_{10}(1 µM)), which were calculated using the PoC values for WT human kinases in the *scan*MAX panel only. The S_{10} score is a way to express selectivity that corresponds with the percent of the kinases screened that bind with a PoC value <10. In the embedded tables kinases are listed by their gene names and ranked by their percent of control (PoC) value generated in the *scan*MAX panel. Rows colored green demonstrate enzymatic IC_{50} values within a 30-fold window of the CDKL5 binding IC_{50} value. Correlating assay format used to generate data in the last column of nested table is listed in the preceding column, with NB = NanoBRET.

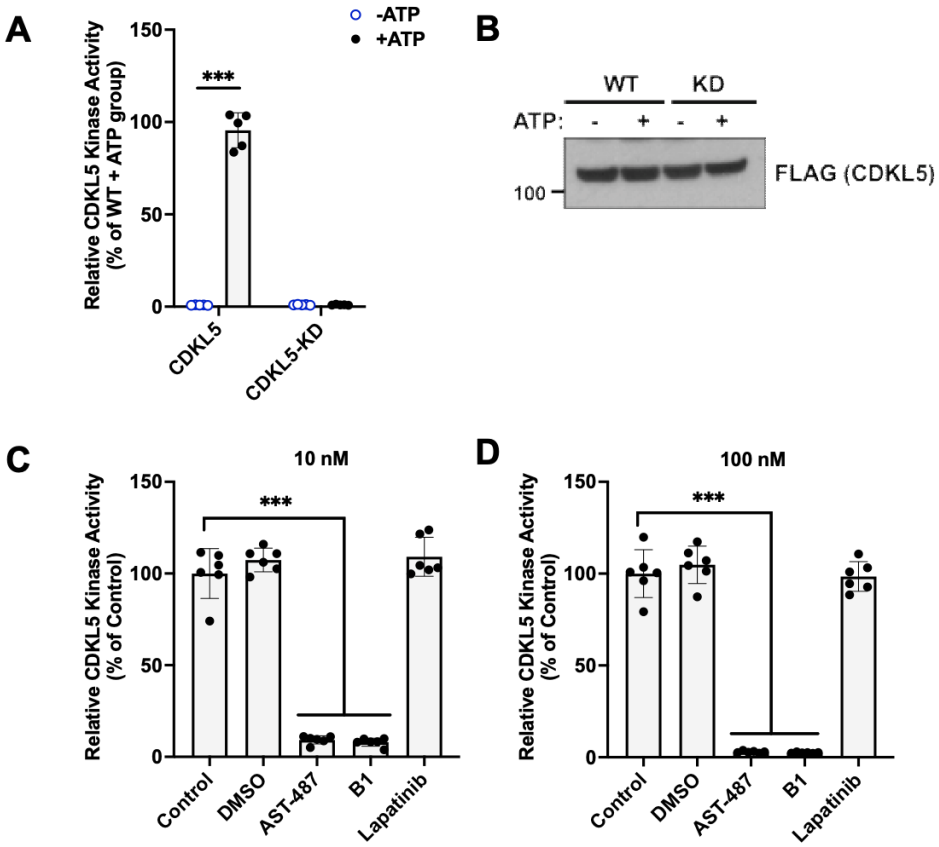

Figure 4. B1 potently inhibits the kinase activity of CDKL5. (A) Representative graph from a CDKL5 kinase assay demonstrating that purified WT human CDKL5 retains kinase activity, while the kinase dead (KD, CDKL5 K42R) human protein is functionally inactive (n = 3). (B) Representative western blot illustrating that equal expression of WT and KD proteins was observed in the kinase assay experiments. (C and D) Kinase assays using purified WT human CDKL5 in the presence of 10 or 100 nM of the indicated compounds (n = 3). One-way ANOVA with Dunnett's multiple comparison test used. *** = $p < 0.0001$ and non-significant comparisons not shown.

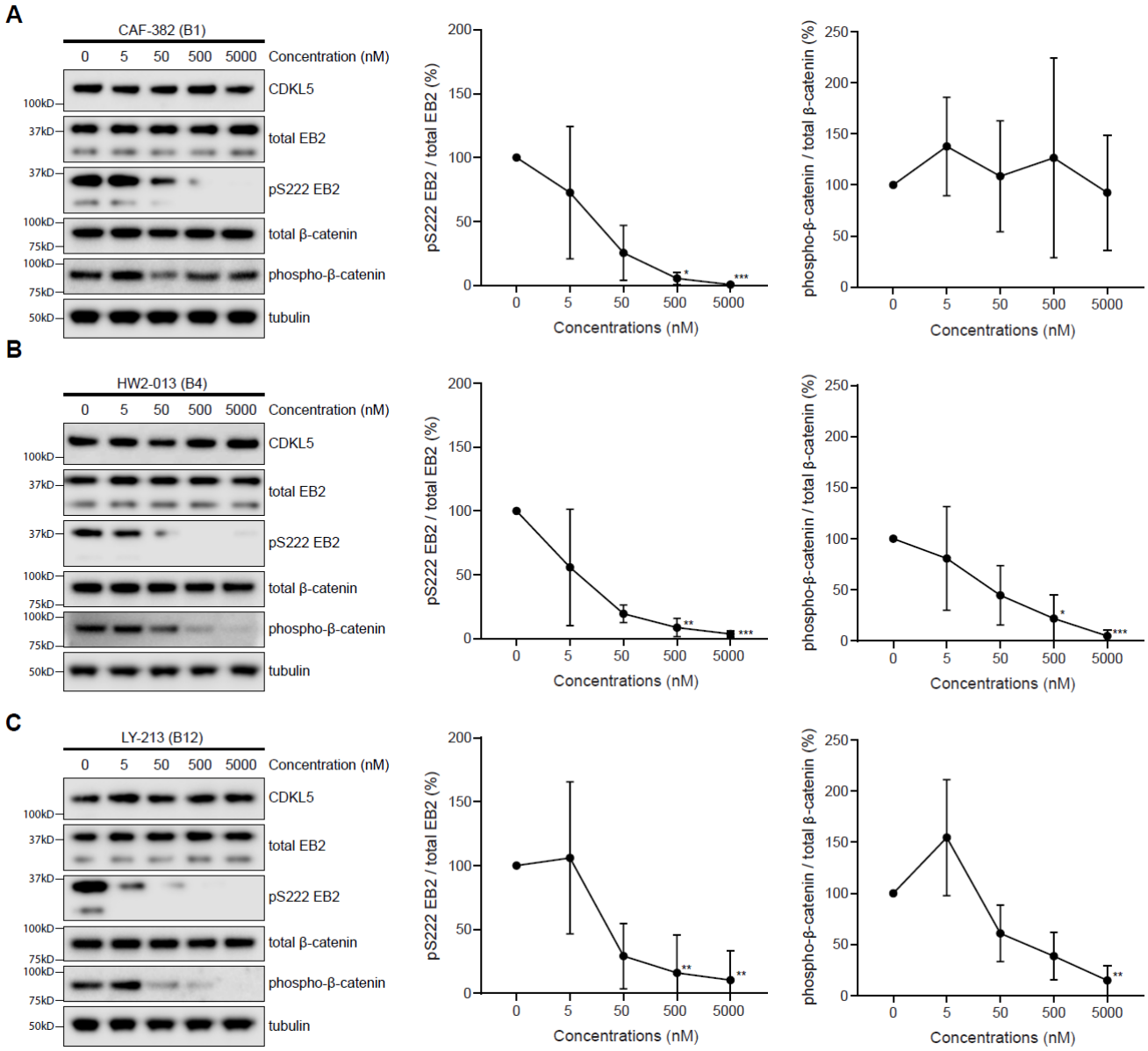

Figure 5. CAF-382 (**B1**), HW2-013 (**B4**), and LY-213 (**B12**) compounds reduce CDKL5 activity in rat primary neurons. HW2-013 (**B4**) and LY-213 (**B12**) also downregulate GSK3 activity. (A) Western blot and quantification showing expression of EB2 phosphorylation and β-catenin phosphorylation in DIV14-15 rat primary neurones after an hour treatment with different concentrations of CAF-382 (**B1**). (B) Western blot and quantification showing expression of EB2 phosphorylation and β-catenin phosphorylation in DIV14-15 rat primary neurons after an hour treatment with different concentrations of HW2-013 (**B4**). (C) Western blot and quantification showing expression of EB2 phosphorylation and β-catenin phosphorylation in DIV14-15 rat primary neurons after an hour treatment with different concentrations of LY-213 (**B12**). Each concentration was compared to the control using a Kruskal-Wallis test. n = 3 biological replicates with 2 repetitions. *p≤0.05. **p≤0.01. ***p≤0.001. Error bars are SD.

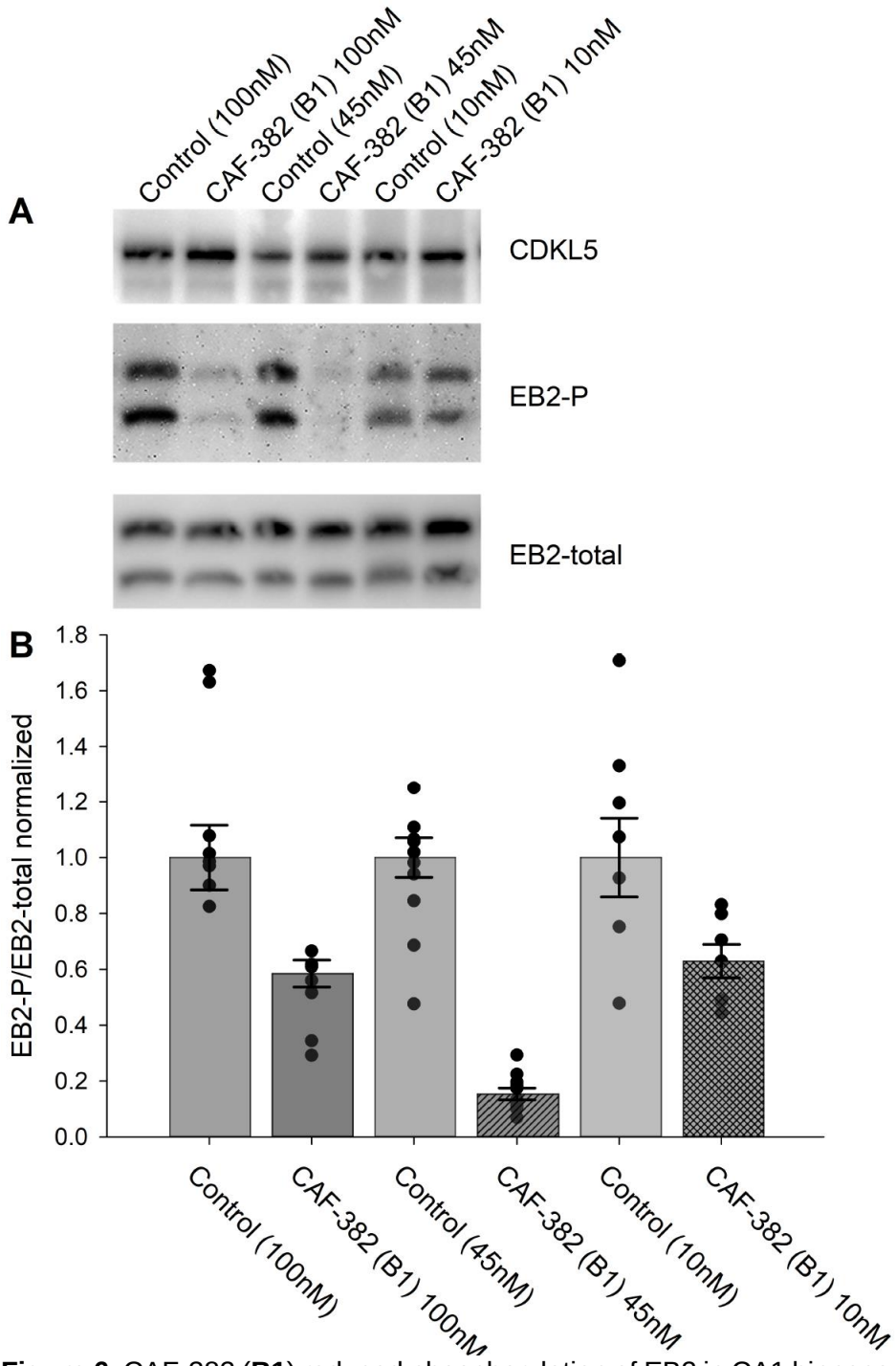

Figure 6. CAF-382 (**B1**) reduced phosphorylation of EB2 in CA1 hippocampal slices. (A) Example blots demonstrate no alterations in CDKL5 expression across treatments (stats in text) and suggest relative CAF-382 (**B1**) dose-dependent differences in EB2 phosphorylation. (B) Normalized quantification of EB2-phosphorylation (density of EB2-phosphorylation bands/ density of EB2-total bands). CAF 382 (**B1**) (control: 1±0.10 versus 100 nM: 0.49±0.02, n = 8, p = 0.002, RM-ANOVA) (control: 1±0.08 versus 45 nM: 0.16±0.03, n = 10, p < 0.001, RM-ANOVA) (control: 1± 0.14 versus 10 nM: 0.62± 0.11, n=7, p = 0.003, RM-ANOVA) reduced EB2 phosphorylation at all concentrations.

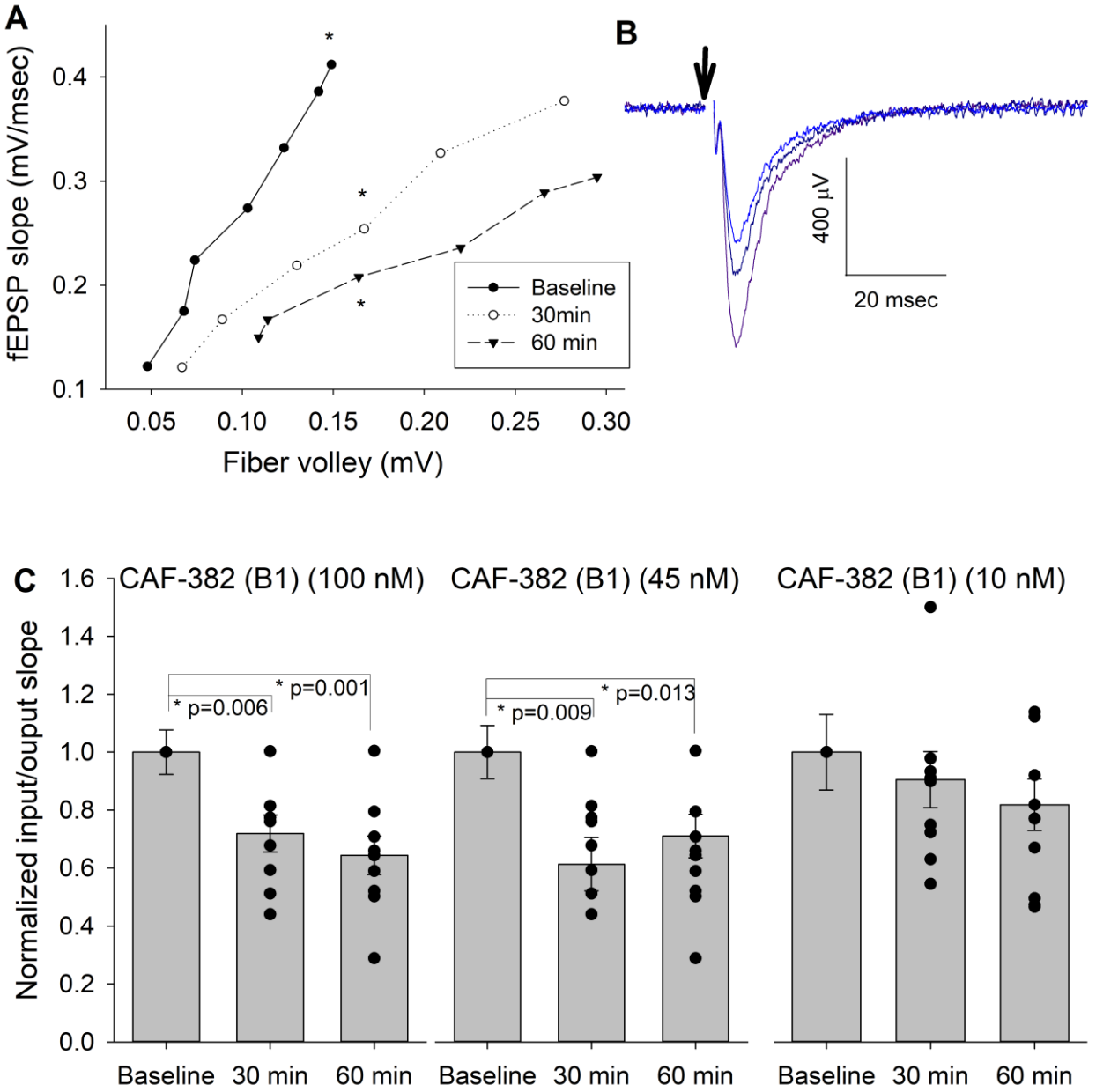

Figure 7. CAF-382 (**B1**) reduced post-synaptic fEPSP responsiveness, as measured by input-output curves. (A) Sample input (fiber volley) / output (fEPSP slope) (I/O) curves at baseline, 30 minutes and 60 minutes after CAF-382 (**B1**) (100nM) in a hippocampal slice. Slopes of I/O curves were obtained at baseline, and 30 minutes and 60 minutes after treatment with CAF-382 (**B1**). Asterisks indicate sample traces (B) from treated slice; stimulus artifact (arrow) has been removed for clarity. Initial negative deflection after the artifact is the fiber volley, followed by the fEPSP. (C) RM-ANOVA of I/O slopes of CAF-382 (**B1**) (100 nM and 45 nM) were significantly decreased after 30 minutes (100 nM: 1.91±0.23, n = 9, p = 0.006; 45 nM: 1.58±0.24, n=10, p = 0.013) and 60 minutes (100 nM: 2.00±0.30, n = 9, p = 0.001; 45 nM: 1.57±0.22, n=10, p = 0.009) compared to baseline (100 nM: 3.24±0.52, n = 9; 45 nM: 2.29±0.23, n=10). Baseline I/O slope was used to normalize each recording to allow comparisons across all treatments. CAF-382 (**B1**) (10 nM) did not alter I/O slopes after 30 or 60 minutes (RM-ANOVA, n = 9, p = 0.07). Error bars are SE.

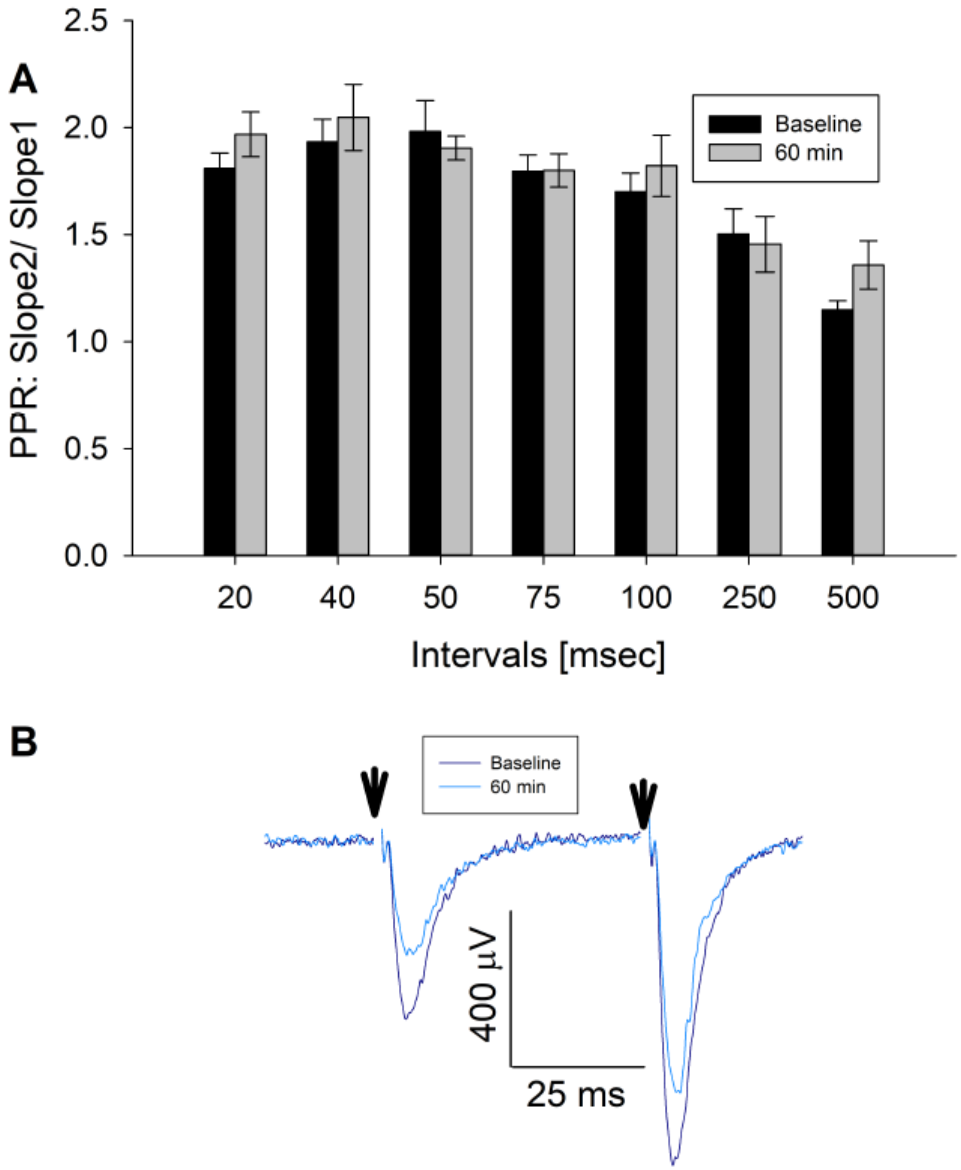

Figure 8. CAF-382 (**B1**) did not alter presynaptic release as measured by paired-pulse ratio. (A) Paired-pulse ratios (PPR) of fEPSPs (Slope of fEPSP2/Slope of fEPSP1), reflective of pre-synaptic release, were unaltered across a range of stimulus intervals (RM-ANOVA, n=7) by CAF-382 (**B1**) (100nM) for 60 minutes compared to baseline. (B) Sample trace for 50 ms interval. Reduction of initial fEPSP slopes were consistent with Figure 7. Stimulus artifacts (arrows) have been removed for clarity. Error bars are SE.

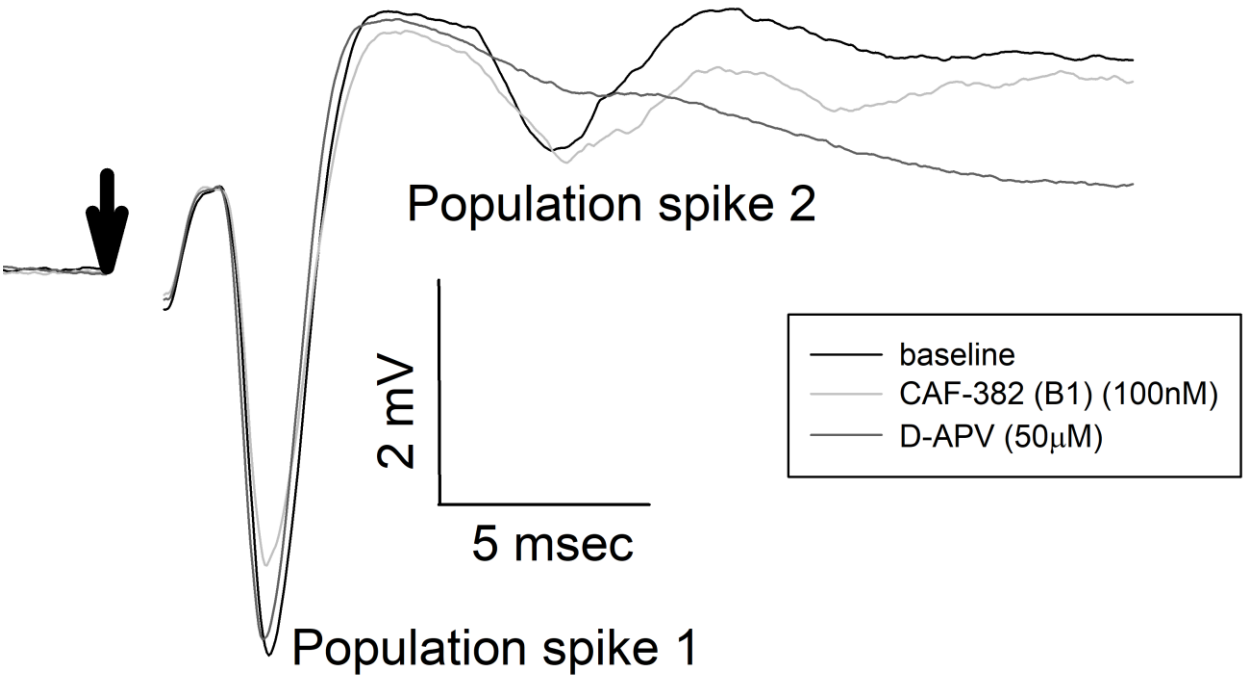

Figure 9. CAF-382 (**B1**) did not alter NMDAR-mediated component of fEPSPs. Maximal fEPSPs recorded in stratum pyramidale of CA1 with reduced extracellular Mg^{2+} demonstrate multiple population spikes; previous studies have demonstrated that secondary population spikes in these conditions are NMDAR-dependent[64]. CAF-382 (**B1**) (100 nM) did not alter population spike 1 (control -4.057±0.584mV, CAF-382 (**B1**) 3.929±0.736mV, n=10, p=0.742, RM-ANOVA) or NMDAR-mediated population spike 2 (control -2.093±0.568mV, CAF-382 (**B1**) -1.656±0.4442, n=10, p=0.867, RM-ANOVA). For comparison, the selective NMDAR antagonist D-APV (50 μM) completely blocked population spike 2, as previously reported [64]. Stimulation artifact has been removed (arrow) for clarity.

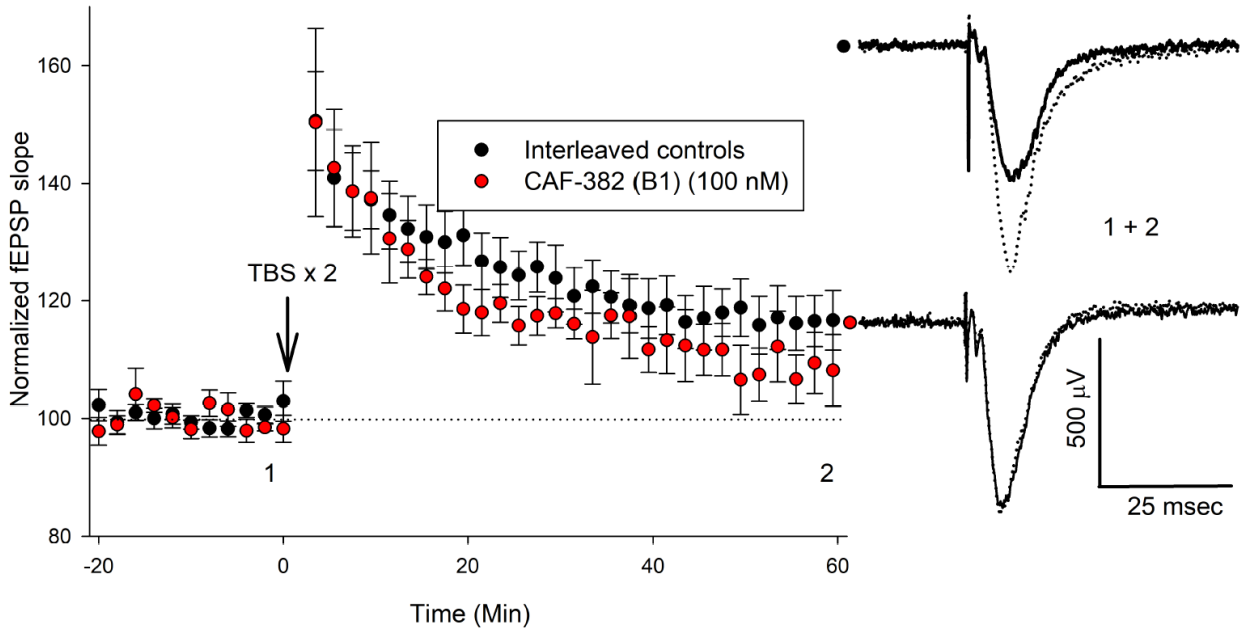

Figure 10. CAF-382 (**B1**) acutely reduces the expression of LTP in CA1 hippocampus. Hippocampal slices were initially incubated in CAF-382 (**B1**) for at least 30 minutes and then continuously perfused with CAF-382 (**B1**) (100 nM). fEPSP slope was normalized to initial baseline, expressed as 100% (dotted line); mean±SEM shown. Following stable baseline of fEPSP slope (> 20 minutes), LTP was induced by two theta-burst (TBS) trains. Compared to interleaved control slices, CAF-382 (**B1**) significantly reduced LTP as measured by fEPSP slope at 56-60 minutes post theta-burst (control: 115.6±2.2 n = 13 slices, 12 rats; CAF-382 (**B1**): 106.4±3.5, n = 5 slices, 4 rats; p = 0.029, 2-way ANOVA, Holm-Sidak post-hoc). Sample traces for control (black filled circle) and CAF-382 (**B1**) (red filled circle) before (1, solid trace) and after LTP (2, dotted trace) are shown to the right. Error bars are SE.

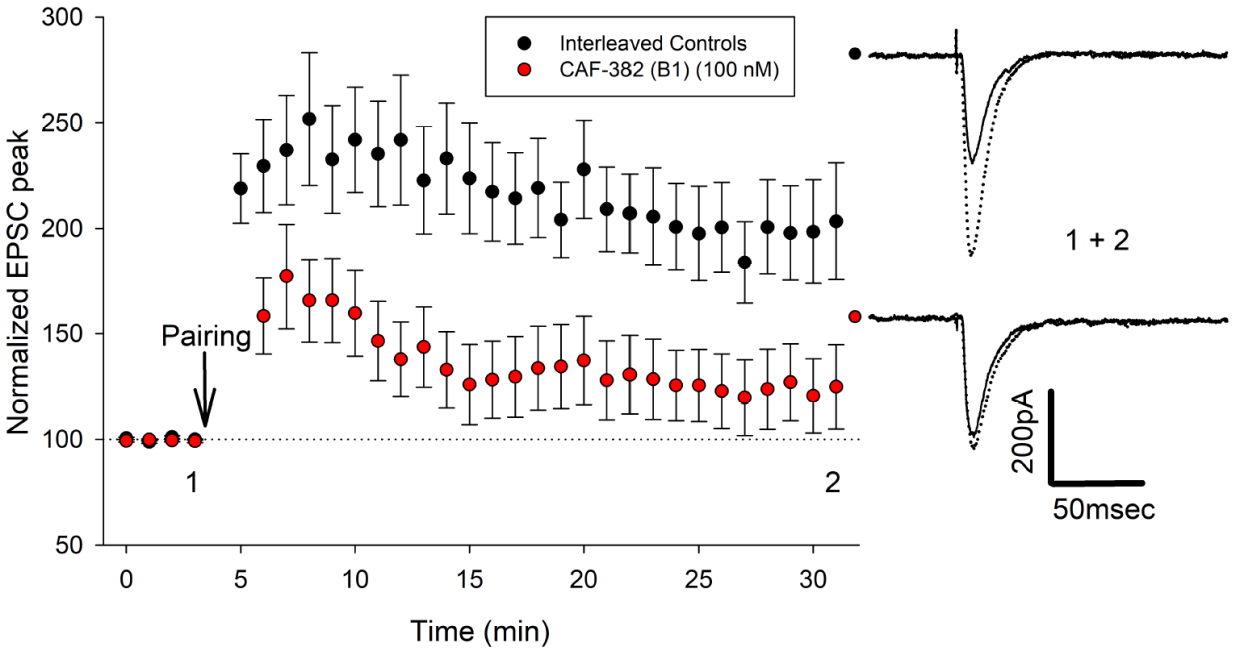

Figure 11. CAF-382 (**B1**) acutely reduces the expression of LTP mediated by AMPA-type glutamate receptors in CA1 hippocampus. Hippocampal slices were initially incubated in CAF-382 (**B1**) (100 nM) for at least 60 minutes prior to recording. Peak negative current of AMPA-type glutamate receptor mediated synaptic responses were normalized to initial baseline post break-in (time = 0), expressed as 100% (dotted line); mean±SEM shown. Following baseline, LTP was induced by a pairing protocol. Compared to interleaved control slices, CAF-382 (**B1**) significantly reduced LTP at 27-31 minutes post break-in (control: 197.5±8.4 n = 14 slices, 14 rats; CAF-382 (**B1**): 123.14±9.0, n = 12-13 slices, 13 rats; $p < 0.001$, 2-way ANOVA, Holm-Sidak post-hoc). Sample traces for control (black filled circle) and CAF-382 (**B1**, red filled circle) before (1, solid trace) and after LTP (2, dotted trace) are shown to the right. Error bars are SE.

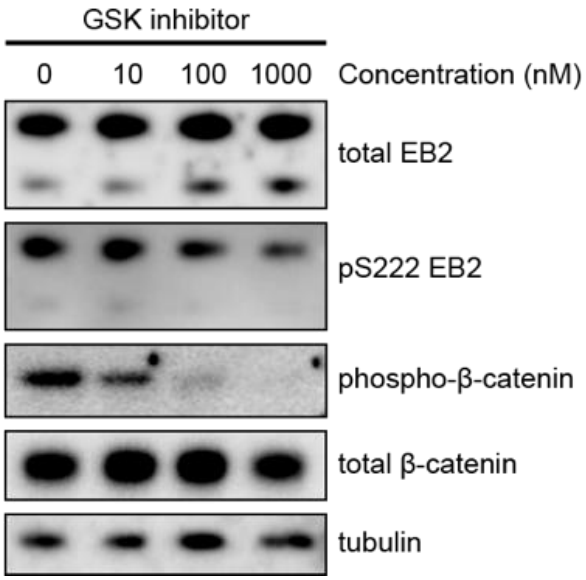

Figure S7. Phosphorylation of β-catenin, a substrate of GSK, is reduced upon treatment with a GSK inhibitor CHIR 99021 (Tocris) but EB2 phosphorylation is not changed. Western blot showing expression of total EB2, pS222 EB2, total β-catenin, phospho-β-catenin and tubulin in DIV14-15 rat primary neurones after an hour treatment with a GSK inhibitor.